



저작자표시-비영리-변경금지 2.0 대한민국

이용자는 아래의 조건을 따르는 경우에 한하여 자유롭게

- 이 저작물을 복제, 배포, 전송, 전시, 공연 및 방송할 수 있습니다.

다음과 같은 조건을 따라야 합니다:



저작자표시. 귀하는 원저작자를 표시하여야 합니다.



비영리. 귀하는 이 저작물을 영리 목적으로 이용할 수 없습니다.



변경금지. 귀하는 이 저작물을 개작, 변형 또는 가공할 수 없습니다.

- 귀하는, 이 저작물의 재이용이나 배포의 경우, 이 저작물에 적용된 이용허락조건을 명확하게 나타내어야 합니다.
- 저작권자로부터 별도의 허가를 받으면 이러한 조건들은 적용되지 않습니다.

저작권법에 따른 이용자의 권리는 위의 내용에 의하여 영향을 받지 않습니다.

이것은 [이용허락규약\(Legal Code\)](#)을 이해하기 쉽게 요약한 것입니다.

[Disclaimer](#)

이학박사 학위논문

**Study of 2-dimensional systems based
on BaSnO₃**

BaSnO₃ 기반의 2차원 시스템에 관한 연구

2021 년 8 월

서울대학교 대학원
물리천문학부
김 유 정

Study of 2-dimensional systems based on BaSnO_3

BaSnO_3 기반의 2차원 시스템에 관한 연구

지도 교수 차국린

이 논문을 이학박사 학위논문으로 제출함

2021년 7월

서울대학교 대학원

물리천문학부

김유정

김유정의 이학박사 학위논문을 인준함

2021년 7월

위원장 유재준

부위원장 차국린

위원 이택희

위원 김도현

위원 홍진표

Abstract

Study of 2-dimensional systems based on BaSnO₃

Youjung Kim

Department of Physics and Astronomy
The Graduate School
Seoul National University

Oxide semiconductors have been widely studied because of their optical transparency and great electrical properties. In particular, oxides with a perovskite structure showed additional novel characteristics such as ferromagnetism, ferroelectricity, multiferroicity, and superconductivity. However, the oxygen instability at high temperature and low mobility at room temperature of oxides have been problems for device applications. BaSnO₃ is a perovskite oxide with the highest electron mobility of 320 cm²/Vs among oxides at a carrier density of about 10²⁰ cm⁻³, and it has high oxygen stability that makes the p-n junction possible. BaSnO₃ has been and can be applied to various fields such as power electronics, high frequency device, solar cell, etc.

This dissertation focuses on the study of BaSnO₃-based two-dimensional systems to investigate the electrical characteristics of quantum wells made by the structures of BaSnO₃/(Ba,La)SnO₃/BaSnO₃ (δ -doped BaSnO₃) and LaInO₃/BaSnO₃. δ -doped BaSnO₃ has quantum well at the La-doped BaSnO₃ layer, which is made by conduction band bending at the BaSnO₃/(Ba,La)SnO₃ interface. LaInO₃/BaSnO₃ has quantum well on the BaSnO₃ side due to the large conduction band offset between the two materials and polarization of LaInO₃.

In the δ -doped BaSnO₃, two-dimensional carrier densities were measured at various

thicknesses and doping levels, and exhibited two unpredictable electrical properties; too low conductance in thin (Ba,La)SnO₃ sample and the conductance increase as the undoped BaSnO₃ capping layer thickens. Analysis using Poisson-Schrödinger simulation shows that these macroscopic properties are physically well explained by continuous band bending and changing surface boundary conditions. Temperature dependent resistance has also been investigated in δ -doped BaSnO₃ films and will be the basis for quantum phenomenon measurements.

LaInO₃/BaSnO₃ showed conductance enhancement at the interface even though both LaInO₃ and BaSnO₃ have insulating properties. The interface has been thought of as a two-dimensional electron gas, and I measured electrical properties of the interface with varying doping level of BaSnO₃ and LaInO₃ thicknesses using epitaxially well grown films confirmed by XRD and STEM. And the field effect transistor was fabricated using a two-dimensional electron gas as a channel layer and LaInO₃ as the high dielectric oxide, and it operated well. The temperature dependent resistance has also been investigated at the LaInO₃/BaSnO₃ interface, and still requires lower dislocation density than now to see the quantum phenomena.

Experimental results of the LaInO₃/BaSnO₃ interface were analyzed using Poisson-Schrödinger simulation to understand how quantum well with high two-dimensional carrier density is formed. 13 kinds of material parameters of LaInO₃ and BaSnO₃ (polarization, concentration and activation energy of donor, deep donor, acceptor, and deep acceptor, effective mass, dielectric constant, band gap, and conduction band offset between two materials) were analyzed to understand their effect on quantum well. High polarization of LaInO₃, appropriate concentrations and activation energies of carriers, not too small effective mass, not too high dielectric constant, and large conduction band offset make quantum well with high two-dimensional carrier density compared to conventional two-

dimensional electron gases. Based on these calculational analysis, I suggest methods for improvement of $\text{LaInO}_3/\text{BaSnO}_3$ two-dimensional electron gas and predict another BaSnO_3 -based two-dimensional electron gas interface.

These studies of δ -doped BaSnO_3 and two-dimensional electron gas at $\text{LaInO}_3/\text{BaSnO}_3$ have led to a physical understanding of the macroscopic electrical characteristics in the two-dimensional system, and the analysis results predict another advanced BaSnO_3 -based two-dimensional systems. Furthermore, it will develop into the observation of quantum phenomena by solving the current problem of dislocation density.

Keywords: BaSnO_3 , LaInO_3 , Perovskite oxide, δ -doping, Two-dimensional electron gas, Poisson-Schrödinger simulation.

Student Number: 2015-20321

List of Contents

Abstract	i
List of Contents	iv
List of Figures and Tables	vi
1. Introduction	1
1.1. Oxide semiconductors	1
1.2. Perovskite oxide BaSnO ₃	1
1.3. Electrical properties of BaSnO ₃	4
References	6
2. δ-doped BaSnO₃	7
2.1. Introduction	7
2.2. Experiment and calculation details	8
2.3. Band bending of BaSnO ₃ /(Ba,La)SnO ₃ interface	12
2.4. Fermi level pinning of (Ba,La)SnO ₃ surface	14
2.5. Temperature dependent electrical property	21
2.6. Conclusion	24
References	25
3. Two-dimensional electron gas at LaInO₃/BaSnO₃ interface	27
3.1. Introduction	27
3.2. Structural properties of LaInO ₃ /BaSnO ₃ interface	29
3.3. Electrical properties of LaInO ₃ /BaSnO ₃ interface.....	33
3.4. Field effect device based on LaInO ₃ /BaSnO ₃ interface	36
3.5. Temperature dependent electrical property	38
3.6. Conclusion	40
References	41

4. Analysis of LaInO₃/BaSnO₃ interface by Poisson-Schrödinger equation	43
4.1. Introduction	43
4.2. Poisson-Schrödinger simulations of conventional two-dimensional electron gases	46
4.2.1. GaAs two-dimensional electron gas	47
4.2.2. GaN two-dimensional electron gas	49
4.2.3. ZnO two-dimensional electron gas	51
4.2.4. Comparison of three conventional two-dimensional electron gases	53
4.3. Experimental results of LaInO ₃ /BaSnO ₃ interface	54
4.4. Poisson-Schrödinger simulations and analysis of LaInO ₃ /BaSnO ₃ interface ...	56
4.4.1. Polarization and deep donor density of LaInO ₃	59
4.4.2. Deep acceptor and shallow donor density of BaSnO ₃	62
4.4.3. Deep carrier activation energy	65
4.4.4. Effective mass, dielectric constant, and conduction band offset	69
4.5. Comparison of two-dimensional electron gases	75
4.6. Conclusion	81
References	82
5. Future direction of LaInO₃/BaSnO₃ and possibility of other BaSnO₃ based interface	87
5.1. Properties of LaInO ₃ /BaSnO ₃ interface	87
5.2. Reduction of dislocation density	89
5.3. Additional conductance enhancement of LaInO ₃ /BaSnO ₃ interface	91
5.4. Other two-dimensional electron gas based on BaSnO ₃	94
5.5. Conclusion	98
References	99
6. Summary	101
List of publications and presentations	103
Abstract in Korean	105

List of Figures

Chapter 1.

Figure 1.1 Resistance measurement of 4% La-doped BSO changing temperature and gases [4].

Figure 1.2 The conductance of 12nm BLSO as the La doping level increases from 0 to 1%.

Figure 1.3 The conduction band bending based on the Fermi level that shows quantum well and the quantized energies of red lines at the (a) δ -doped BSO system and (b) LIO/BSO 2DEG system.

Chapter 2.

Figure 2.1 Profiler measurement of a 1% BLSO film deposited by 5000 pulsed of laser produced 163.35 nm, namely the growth rate of 0.03267 nm/pulse.

Figure 2.2 Two contact methods to measure the electrical properties of δ -doped samples. (a) Contacts made by pressing Au-coated CuBe tips. (b) Contacts by depositing 4% BLSO pads using a stencil mask on the edges of the ion milled δ -doped samples.

Figure 2.3 (a) Structure of δ -doped BSO to measure the BLSO thickness dependent electrical properties. (b) Experimental results of 2D carrier densities with different BLSO thicknesses with blue and red dots in 0.5% and 1% La-doped BLSO layer. The lines are guides of the predicted 2D carrier density proportional to the channel thickness based on the experimental data from BLSO 20 nm sample.

Figure 2.4 AFM images of the 1% La-doped BSO surface on MgO substrate with 60 nm BHO and 150 nm BSO buffer layer in two different lateral scales.

Figure 2.5 Experimental and calculated results for δ -doped BSO films. (a) 2D carrier density of δ -doped BSO films with different BLSO thicknesses. The BLSO layer is doped with 0.5% La in blue and 1% in red. The lines are the results calculated with 1×10^{19} and $3 \times 10^{19} \text{ cm}^{-3}$ deep acceptor density. The experimental results in circles fit well with the calculations at about $3 \times 10^{19} \text{ cm}^{-3}$ deep acceptor density. (b) Calculated results of conduction band bending for 1% δ -doped samples with different thicknesses of 1% BLSO channel layer.

Figure 2.6 The 2D carrier density as the 1% BLSO channel thickness changes at a deep

acceptor density of (a) $3 \times 10^{19} \text{ cm}^{-3}$ and (b) $1 \times 10^{17} \text{ cm}^{-3}$. The 2D carrier density of N_D is derived from BLSO with a shallow donor density of $1.43 \times 10^{20} \text{ cm}^{-3}$ of 1% doping, and N_D-N_{DA} is from BLSO with shallow donor and deep acceptor. The 2D carrier density of the δ -doped BSO is from BLSO with shallow donor and deep acceptor in the δ -doping structure. N_D and N_D-N_{DA} are results without considering band bending and δ -doped BSO is the result considering band bending.

Figure 2.7 The effect of an undoped BSO capping layer over the BLSO layer. (a) Experimental conductance of the 1% 7.5 nm BLSO layer as a function of the thickness of the undoped BSO overlayer. (b) 2D carrier density of 0.5% and 1% BLSO layer with (circle) and without (triangles) 20 nm undoped BSO overlayer as a function of BLSO thickness. The 2D carrier density increases after depositing the undoped BSO overlayer.

Figure 2.8 (a) Structure to investigate the effect of an undoped BSO capping layer over the BLSO layer. (b) Predicted conduction band bending before and after deposition of the capping layer in solid and dashed lines. (c) Experimental results in blue dots and calculated results of 2D carrier density before and after the capping layer in triangle and line with the band bending of (b).

Figure 2.9 2D carrier density and band bending of δ -doped BSO films with 1% doped 7.5 nm BLSO layer with different boundary conditions. (a) Experimental and calculated carrier density using three kinds of boundary conditions as a function of the BSO capping layer thickness. (b) Band bending using “Ohmic” boundary condition showing similar trend to the experimental carrier density only in the thick BSO capping layer. Five cases of BSO capping layer thicknesses of 0.4, 1.5, 3.0, 4.5 and 10 nm described in experimental result in (a) are shown. (c) Band bending using “Schottky” boundary condition well fitted to the experimental carrier density. Five cases of BSO capping layer thicknesses of 0.0, 1.5, 3.0, 4.5 and 10 nm described in experimental result in (a) are shown.

Figure 2.10 The position of the conduction band minimum in comparison to the Fermi level used for the “Schottky” boundary condition in Fig 2.9 (c).

Figure 2.11 Calculated band bending of δ -doped BSO films by the “Schottky” boundary conditions same as in Fig 2.10 using $2.7 \times 10^{19} \text{ cm}^{-3}$ deep acceptor density. The shaded areas represent the differences between with and without the capping layer in the case of (a) 20 nm thick 0.5% BLSO and (b) 20 nm thick 1% BLSO.

Figure 2.12 Properties of δ -doped BSO films using 2% La doping with the structure of Fig 2.3(a). (a) 2D carrier density with different BLSO thickness. The experimental results fit

well with the calculation with about $2 \times 10^{19} \text{ cm}^{-3}$ deep acceptor density. (b)(c) Temperature dependent resistance of the δ -doped BSO, exhibiting transition from metal to semiconductor when the BLSO film becomes thinner.

Chapter 3.

Figure 3.1 XRD pattern of a sample with LIO/BSO interface grown on [001] MgO substrate. (a) θ - 2θ diffraction peaks corresponding to the (002) plane of substrate, buffer layers, BSO and pseudocubic LIO. (b) RSM result of the LIO/BSO interface layers.

Figure 3.2 Structural properties of the interface on MgO substrate seen in STEM images. (a) Overall image from the substrate to LIO layer, showing a large TD density in each film. (b) BSO/BHO interface (c) LIO/BSO interface which is coherently epitaxial.

Figure 3.3 AFM image of the surface of a 0.2 % La-doped BSO film, showing roughness less than a unit cell height. No unit cell height structure has been observed.

Figure 3.4 LIO/BLSO structure to measure electrical properties varying La doping rate of the channel layer.

Figure 3.5 Transport properties of LIO/BLSO interface on MgO and STO substrate [5]. (a) The sheet conductance of the before and after the formation of LIO/BLSO interface as a function of the La doping rate of the BLSO channel on MgO and STO substrates. (b) Carrier density and (c) mobility value of LIO/BLSO interface while varying the La doping rate on MgO and STO substrates.

Figure 3.6 LIO thickness dependence of the LIO/BLSO interface conductance.

Figure 3.7 Structure and I-V characteristic of FET device based on unintentionally doped LIO/BSO interface on MgO substrate. (a) Cross-sectional structure of the device. (b) The top view of the device by an optical microscope. (c) The output characteristics of the device varying the gate voltage from 0 V to 24 V. (d) The transfer characteristics of the device in the linear region with $V_{DS} = 1 \text{ V}$. The maximum mobility = $61.3 \text{ cm}^2/\text{Vs}$, $I_{on}/I_{off} = 1.0 \times 10^9$, and the subthreshold swing = 0.206 V/dec .

Figure 3.8 Calculated 3D carrier density of LIO/ 0.3% BLSO interface and δ -doped BSO with 2% doped 2 nm and 3 nm channel layer.

Figure 3.9 Temperature dependent resistance of the LIO/BLSO interface described with the result of δ -doped BSO.

Chapter 4.

Figure 4.1 P-S simulation of AlGaAs/GaAs 2DEG. (a) Structure and parameters for calculation. (b) Calculation result of conduction band minimum energy for the Fermi level of 0 eV. (c) An enlarged view of (b) near the interface of AlGaAs and GaAs with subband energy of the red line.

Figure 4.2 P-S simulation of AlGaN/GaN 2DEG. (a) Structure and parameters including the direction of the polarizations for calculation. (b) Calculation result of conduction band minimum energy for the Fermi level of 0 eV. (c) An enlarged view of (b) near the interface of AlGaN and GaN with subband energy of the red line.

Figure 4.3 P-S simulation of MgZnO/ZnO 2DEG. (a) Structure and parameters including the direction of the polarizations for calculation. (b) Calculation result of conduction band minimum energy for the Fermi level of 0 eV (c) An enlarged view of (b) near the interface of MgZnO and ZnO with subband energy of the red line.

Figure 4.4 An experiment to measure the 2D carrier density (n_{2D}) of LIO/BLSO interface as the LIO thickness increases. (a) LIO/BLSO schematic structure with buffer and contact layers. (b) n_{2D} of interface at each LIO thickness.

Figure 4.5 Results of P-S calculations and comparative experiments to define the unknown polarization value and deep donor density of LIO on the LIO/BLSO interface. (a) Interface polarization values on the LIO side that explains the experimental results well. (b) Carrier densities of quantum well calculated using the interface polarization in (a) were drawn by the green solid line that explains the experimental result of the blue dots. Increased and decreased carrier densities of red and purple solid lines from green solid line are calculated using the polarization values that are increased and decreased 10% from (a). Carrier densities using constant polarization that has same polarization value in the whole LIO film is shown in dashed lines, which cannot explain experimental data. (c) Carrier densities of quantum well with LIO deep donor densities of $5 \times 10^{19} \text{ cm}^{-3}$, $1.3 \times 10^{20} \text{ cm}^{-3}$, and $2 \times 10^{20} \text{ cm}^{-3}$ using the polarization of (a) according to the LIO thickness were drawn with solid lines and the blue dots show experimental results. (d) Changes in minimum conduction band bending at each deep donor density of LIO at LIO 10nm. Enlarged quantum well is shown in the inset.

Figure 4.6 Influence of the deep acceptor density and shallow donor density of BSO on the LIO/undoped BSO and the LIO/BLSO interface calculated with the P-S equation. (a) Carrier densities of quantum well with deep acceptor density of $1 \times 10^{17} \text{ cm}^{-3}$, $1 \times 10^{18} \text{ cm}^{-3}$

³, $1 \times 10^{19} \text{ cm}^{-3}$, $4 \times 10^{19} \text{ cm}^{-3}$, and $6 \times 10^{19} \text{ cm}^{-3}$ according to the LIO thickness. (b) Changes in minimum conduction band bending at each deep acceptor density of BSO at LIO 10 nm. (c) Carrier densities of quantum well with shallow donor density from 0 to $5.72 \times 10^{19} \text{ cm}^{-3}$ (0.4% BSLO) according to the LIO thickness. (d) Changes in minimum conduction band bending at each shallow donor density of BSO at LIO 10 nm.

Figure 4.7 Influence of the deep acceptor activation energy of BSO and deep donor activation energy of LIO on the LIO/undoped BSO interface calculated with the P-S equation. (a) Changes in minimum conduction band bending at different deep acceptor activation energy of BSO, 0.5 eV, 1.0 eV, and 1.55 eV at LIO 10 nm. (b) Polarization adjustment to applicate other deep acceptor activation energies of BSO. (c) Changes in minimum conduction band bending at different deep donor activation energy of LIO, 1.5 eV, 2.0 eV, and 2.5 eV at LIO 10 nm. (d) Polarization adjustment to applicate other deep donor activation energies of LIO.

Figure 4.8 Influence of the effective mass of BSO and LIO on the LIO/BLSO interface calculated with the P-S equation. (a) Carrier densities of quantum well with BSO effective masses of $0.2 m_e$, $0.42 m_e$, and $7 m_e$ according to the LIO thickness. (b) Changes in minimum conduction band bending at each effective mass of BSO at LIO 10 nm. (c) Carrier densities of quantum well with LIO effective masses of $0.2 m_e$, $0.46 m_e$, and $7 m_e$ according to the LIO thickness. (d) Changes in minimum conduction band bending at each effective mass of LIO at LIO 10 nm.

Figure 4.9 Influence of the dielectric constant of BSO and LIO on the LIO/BLSO interface calculated with the P-S equation. (a) Carrier densities of quantum well with BSO dielectric constants of 10, 20, 50, and 100 according to the LIO thickness. (b) Changes in minimum conduction band bending at each dielectric constant of BSO at LIO 10 nm. (c) Carrier densities of quantum well with LIO dielectric constants of 25, 38, and 50 according to the LIO thickness. (d) Changes in minimum conduction band bending at each dielectric constant of LIO at LIO 10 nm.

Figure 4.10 Influence of the conduction band offset between BSO and LIO on the LIO/BLSO interface calculated with the P-S equation. (a) Carrier densities of quantum well with conduction band offsets of 1.0 eV, 1.6 eV, and 2.4 eV according to the LIO thickness. (b) Changes in minimum conduction band bending at each conduction band offset at LIO 10 nm.

Chapter 5.

Figure 5.1 Polarization distributions at (a) AlGaAs/GaAs (b) AlGaN/GaN (c) MgZnO/ZnO (d) LIO/BSO interface.

Figure 5.2 Influence of reduced deep acceptor density of BSO on the LIO/undoped BSO interface calculated with the P-S equation at temperature 4 K. (a) Minimum conduction band bending of the interface with $1 \times 10^{18} \text{ cm}^{-3}$, $1 \times 10^{19} \text{ cm}^{-3}$, and $4 \times 10^{19} \text{ cm}^{-3}$ deep acceptor density. (b) Enlarged views of band near the interface and subband energies of the 2D quantum wells at each deep acceptor densities of BSO.

Figure 5.3 Experiments for the enhancement of LIO/BLSO conductance. (a) Structure of 2DEG interface that has additional X layer on LIO layer. (b) Conductance enhancement after deposition of about 100 nm material X on LIO.

Figure 5.4 Different electrical characteristics depending on the deposition order of the interface between LIO and undoped BSO (a)(b) Structure and conductance results of the interface when the BSO layer was deposited on the LIO. (c)(d) Structure and conductance results of the interface when the LIO layer was deposited on the BSO.

Figure 5.5 Different electrical characteristics depending on the deposition order of the interface between LIO and 0.2% La-doped BSO (a)(b) Structure and conductance results of the interface when the BLSO layer was deposited on the LIO. (c)(d) Structure and conductance results of the interface when the LIO layer was deposited on the BLSO.

Figure 5.6 Quantum well formation without polarization based on BSO. (a) Minimum conduction band bending at unknown material X and BSO interface when the conduction band offset between X and BSO is 1.5, 2.5, and 3.5 eV with the deep donor activation energy of 2.5 eV of X. X does not have any polarization and has same material parameters with BSO, except the band gap of 5 eV. (b) Minimum conduction band bending at unknown material X and BSO interface when the deep donor activation energy of X is 0.5, 1.5, and 2.5 eV with the conduction band offset 1.5 eV. (c) Carrier densities of quantum well at each combination of the X deep donor activation energy and the conduction band offset between X and BSO. (d) The X deep donor activation energy and the conduction band offset between X and BSO that make the quantum well n_{2D} of about $1 \times 10^{10} \text{ cm}^{-2}$, which means minimum condition to form the quantum well.

List of Tables

Chapter 1.

Table 1.1 FETs based on BSO

Chapter 4.

Table 4.1 Materials parameters used for GaAs, AlGaAs, GaN, AlGaN, ZnO and MgZnO

Table 4.2 13 kinds of materials parameters used for BSO and LIO

Table 4.3 Materials parameters and interface properties at GaAs, GaN, ZnO, LIO/BSO, and LAO/STO 2DEGs.

Table 4.4 Simulation results of GaAs, GaN, ZnO, LIO/BSO, and LAO/STO 2DEGs at temperature of 300K.

Table 4.5 Simulation results of GaAs, GaN, ZnO, LIO/BSO, and LAO/STO 2DEGs at temperature of 4K.

Chapter 1. Introduction

1.1. Oxide semiconductors

Oxide semiconductors have been widely studied because of their optical transparency over 80% and great electrical properties. In_2O_3 , SnO_2 , and ZnO have been studied as transparent conducting oxides with n-type dopants that exhibit high mobility with small effective masses made by the closed shell electronic configuration. In particular, oxides with a perovskite structure of ABO_3 showed additional novel characteristics. They can be easily doped compared to binary oxides and showed ferromagnetism, ferroelectricity, multiferroicity, and superconductivity in $\text{YBa}_2\text{Cu}_3\text{O}_7$, $\text{Pb}(\text{Zr},\text{Ti})\text{O}_3$, and SrTiO_3 (STO) [1-3]. However, oxygen instability at high temperature leads to poor reliability and difficulty of p-type doping, and low electron mobility at room temperature of oxides have been problems for device applications.

1.2. Perovskite oxide BaSnO_3

BaSnO_3 (BSO) is a perovskite oxide material that can break the limits of oxide semiconductors with three big strengths, including the advantages of other oxides and advantages coming from perovskite structure. First, BSO exhibits the highest room temperature mobility at degenerate region among perovskite oxides [4-6]. BSO has a mobility of $320 \text{ cm}^2/\text{Vs}$ at a carrier density of about 10^{20} cm^{-3} . The small effective mass of the Sn 5s orbital that makes up the conduction band is partially responsible for its high mobility [7-10]. In addition, the high mobility comes from the low scattering rate compared to other perovskite oxides [7,11]. Low scattering rate is facilitated by its single degenerate conduction band composed of s orbital of Sn while many other perovskites have conduction

bands with d orbitals with 3-fold degeneracy [11]. Second, BSO has high oxygen stability. In the previous report, the oxygen stability of BSO was measured using 4% La-doped BSO [4]. The temperature was raised to 530 degrees and maintained flowing Ar, oxygen and air gas, and the resistance was measured in Fig 1.1. There was only about 8% resistance change when it reached equilibrium state in an Ar gas atmosphere, and 1.7% resistance change in air. These resistance changes are caused by oxygen diffusion but it is very small compared to other oxides. ZnO shows one order of resistance change in air and four orders of change in a nitrogen atmosphere. The oxygen stability of BSO plays an important role in the development of oxide heterostructures and devices. And it shows the possibility of p-n junction that already has confirmed using La-doped n-type BSO and K-doped p-type BSO [12]. Third, BSO can be easily doped in n-type up to the level of several 10^{20} cm^{-3} due to the low formation energy and the high energy level of the La donor state, while the undoped BSO remains a good insulator because most defects in BSO seem to lie at the deep level [9,10,13,14]. This is shown in Fig 1.2 with the measured conductance of 12 nm (Ba,La)SnO₃ (BLSO) as the La doping level changes. BSO has all three advantages that oxides generally do not have at the same time, and BSO has been and can be applied to various fields such as power electronics, high frequency device, solar cell, etc.

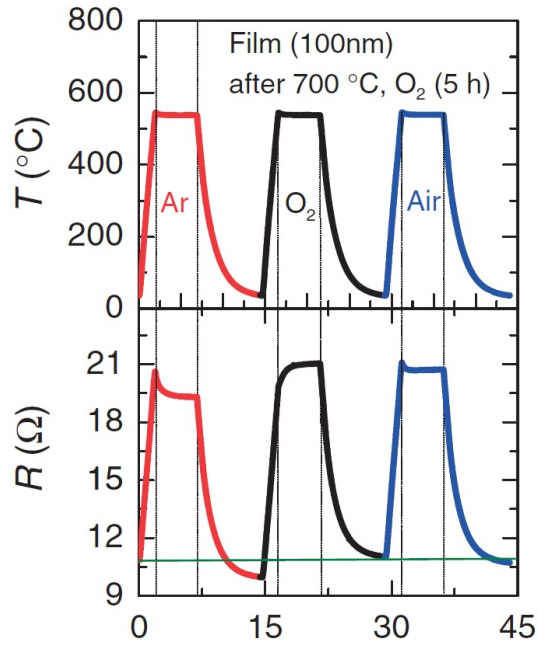


Figure 1.1 Resistance measurement of 4% La-doped BSO changing temperature and gases [4].

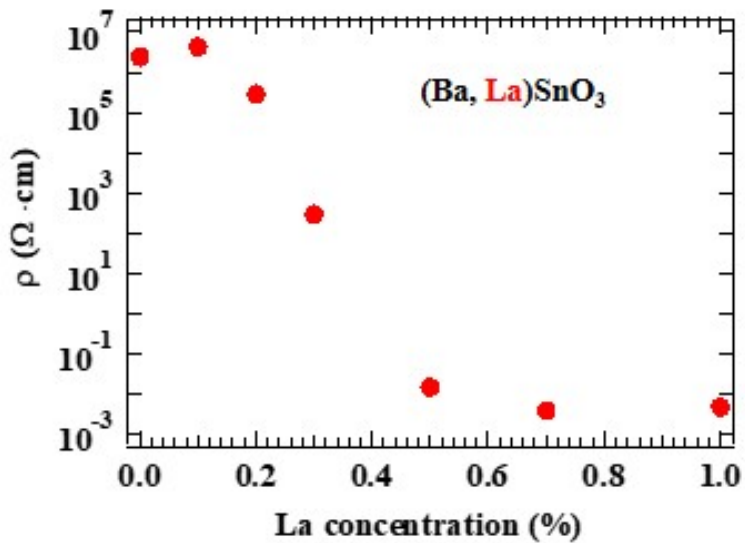


Figure 1.2 The conductance of 12nm BLSO as the La doping level increases from 0 to 1%.

1.3. Electrical properties of BaSnO₃

Based on great material properties of BSO, film growth and device fabrication were studied and developed using La dopant to make n-type doping. Well-set deposition conditions are basic steps for the epitaxial film [15], and for the reduction of dislocation density that makes electron trap, appropriate substrates and buffer layers were used under the BSO films [16,17]. Typically, STO and MgO were used as a substrate to grow BSO films among materials with similar lattice constant to BSO. STO has the same perovskite structure with lattice constant of 3.9 Å and MgO has a lower lattice mismatch with BSO than STO, although MgO does not have perovskite structure. Undoped BSO of appropriate thickness is known to be used as a buffer layer under the La-doped BSO layer. BSO buffer layers of 100 nm or less appeared not to sufficiently eliminate threading dislocations, and buffer layers above 200 nm appeared to have a bad effect on electrical properties by increasing surface roughness [16,17]. This was the same for STO and MgO substrates. An additional buffer layer of BaHfO₃ (BHO), which has a lattice constant between MgO and BSO, also helped to reduce dislocation density of the BSO film on the MgO substrate [18].

Field effect transistors (FET) were also fabricated using the BLSO channel layer, and results are shown in the Table 1.1. Using Al₂O₃, HfO₂ as dielectrics, it was confirmed that FETs worked well, and the maximum mobility and I_{on}/I_{off} showed similar values to other oxide-based FETs [16-18]. Furthermore, all-perovskite-FETs were tried using LaInO₃ (LIO) and BHO as a dielectric with the contact layers of metallic 4% BLSO [19-21]. They showed great properties of maximum mobility of 90 cm²/Vs at the FET with LIO dielectric and 0.07% BLSO channel and 10⁹ of I_{on}/I_{off} at the FET with LIO dielectric and undoped BSO channel that are highest values among BSO based FETs.

Dielectric material	$\mu_{FE}(\text{cm}^2\text{V}^{-1}\text{s}^{-1})$	$I_{\text{On}}/I_{\text{off}}$ ratio	References
Al_2O_3	17.8	10^5	[16]
HfO_2	43.9	3.0×10^7	[17]
HfO_2	24.9	6.0×10^6	[18]
LaInO_3	90	10^7	[19]
LaInO_3	48.9	10^9	[20]
BaHfO_3	52.7	10^7	[21]

Table 1.1 FETs based on BSO

Based on these material properties and electrical properties of BSO, there have been various kinds of application studies such as p-n junction, power electronics, high frequency device, and solar cell. I focused on two-dimensional (2D) properties of BSO for the start of measurement of quantum phenomena with the δ -doped BSO and LIO/BSO two-dimensional electron gas (2DEG) systems that have 2D quantum well and quantized energy eigenvalues shown in Fig 1.3.

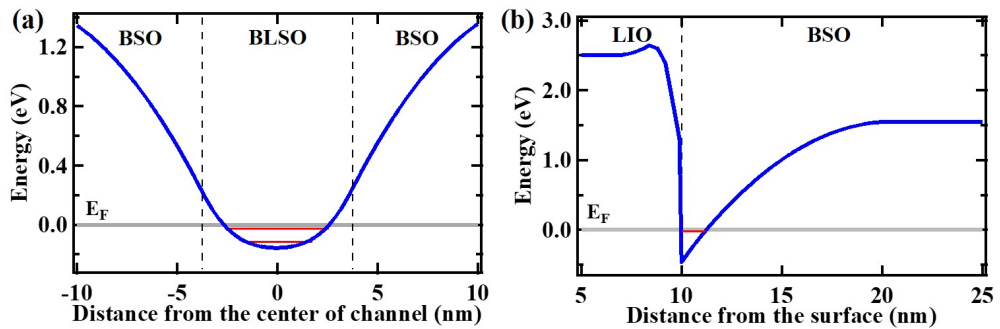


Figure 1.3 The conduction band bending based on the Fermi level that shows quantum well and the quantized energies of red lines at the (a) δ -doped BSO system and (b) LIO/BSO 2DEG system.

References

- [1] M. K. Wu, J. R. Ashburn, and C. J. Torng, *Phys. Rev. Lett.* **58**, 908 (1987).
- [2] R. Gupta, M. Tomar, A. Kumar, and V. Gupta, *Smart Mater. Struct.* **26**, 035002 (2017).
- [3] W.J. Burke and R.J. Pressley, *Solid State Commun.* **9**, 191 (1971).
- [4] H. J. Kim, U. Kim, H. M. Kim, T. H. Kim, H. S. Mun, B.-G. Jeon, K. T. Hong, W.-J. Lee, C. Ju, K. H. Kim, and K. Char, *Appl. Phys. Express* **5**, 061102 (2012).
- [5] S. Raghavan, T. Schumann, H. Kim, J. Y. Zhang, T. A. Cain, and S. Stemmer, *APL Mater.* **4**, 016106 (2016).
- [6] A. Prakash, P. Xu, X. Wu, G. Haugstad, X. Wang and B. Jalan, *J. Mater. Chem. C* **5**, 5730 (2017).
- [7] H. J. Kim, U. Kim, T. H. Kim, J. Kim, H. M. Kim, B.-G. Jeon, W.-J. Lee, H. S. Mun, K. T. Hong, J. Yu, K. Char, and K. H. Kim, *Phys. Rev. B* **86**, 165205 (2012).
- [8] H. Mizoguchi, H. W. Eng, and P. M. Woodward, *Inorg. Chem.* **43**, 1667 (2004).
- [9] H.-R. Liu, J.-H. Yang, H. J. Xiang, X. G. Gong, and S.-H. Wei, *Appl. Phys. Lett.* **102**, 112109 (2013).
- [10] S. Sallis, D. O. Scanlon, S. C. Chae, N. F. Quackenbush, D. A. Fischer, J. C. Woicik, J.-H. Guo, S. W. Cheong, and L. F. J. Piper, *Appl. Phys. Lett.* **103**, 042105 (2013).
- [11] K. Krishnaswamy, B. Himmetoglu, Y. Kang, A. Janotti, and C. G. Van de Walle, *Phys. Rev. B* **95**, 205202 (2017).
- [12] H. M. Kim, U. Kim, C. Park, H. Kwon, and K. Char, *APL Mater.* **4**, 056105 (2016).
- [13] Z. Lebens-Higgins, D. O. Scanlon, H. Paik, S. Sallis, Y. Nie, M. Uchida, N. F. Quackenbush, M. J. Wahila, G. E. Sterbinsky, D. A. Arena, J. C. Woicik, D. G. Schlom, and L. F. J. Piper, *PRL* **116**, 027602 (2016).
- [14] D. O. Scanlon, *Phys. Rev. B* **87**, 161201(R) (2013).
- [15] U. Kim, Ph. D. thesis, Seoul National University (2015).
- [16] C. Park, U. Kim, C. J. Ju, J. S. Park, Y. M. Kim, and K. Char, *Appl. Phys. Lett.* **105**, 203503 (2014).
- [17] J. Shin, Y. M. Kim, Y. Kim, C. Park, and K. Char, *Appl. Phys. Lett.* **109**, 262102 (2016).
- [18] Y. M. Kim, C. Park, U. Kim, C. Ju, and K. Char, *Appl. Phys. Express* **9** 011201 (2016).
- [19] U. Kim, C. Park, T. Ha, Y. M. Kim, N. Kim, C. Ju, J. Park, J. Yu, J. H. Kim, and K. Char, *APL Materials* **3**, 036101 (2015).
- [20] Y. Kim, Y. M. Kim, J. Shin, and K. Char, *APL Materials* **6**, 096104 (2018).
- [21] Y. M. Kim, C. Park, T. Ha, U. Kim, N. Kim, J. Shin, Y. Kim, J. Yu, J. H. Kim, and K. Char, *APL Mater.* **5**, 016104 (2017).

Chapter 2. δ -doped BaSnO₃

In this chapter, I will discuss the δ -doped BSO system for the study of a simple 2D system based on BSO, focusing on its band bending and surface boundary conditions. The two-dimensional carrier density (n_{2D}) of δ -doped BSO system was measured with various thicknesses and doping levels. I also studied the effect of BSO capping layer thickness on n_{2D} . It shows that the δ -doped BSO system can be very well described by band bending with the aid of the Poisson-Schrödinger simulation. At the same time, the capping layer thickness dependence of n_{2D} reveals how the boundary condition on the surface of La-doped BSO evolves as a function of its capping layer thickness. I also investigated the temperature dependent resistance of δ -doped BSO films as a 2D system and found a metal-semiconductor transition as a function of the δ -doped thickness.

2.1. Introduction

δ -doped semiconductors with only a few nm thick dopant layer have been effectively utilized in devices such as diodes, transistors, and lasers [1,2]. GaAs and Si have been extensively studied and much remains to be explored [1,3]. This system has a quasi-two-dimensional potential well that creates quantized energy levels [1,4] and even the quantum Hall effect was seen in δ -doped GaAs [5,6].

In perovskite oxide systems, STO has been previously studied extensively for 2D carriers. For example, the LaAlO₃(LAO)/STO interface system were used to study enhanced thermoelectric efficiency [7] and interface metallic conductivity [8,9]. δ -doped STO were studied for quantum ground state formation at low temperature [10-12]. To date, the quantum Hall effects have been observed only in δ -doped STO system, not yet in LAO/STO systems. In addition, δ -doped STO system showed novel properties in measurement of the quantum Hall effect skipping specific Landau level filling factors. This was thought because of strong electron correlation effects of 3d orbitals consisting STO

conduction band while many kinds of conventional semiconductors have carriers in s and p orbital [11].

My focus is on the δ -doped BSO system that forms a quantum well structure for 2D-like transport properties. In particular, the band bending between undoped BSO and BLSO and the boundary conditions for BSO and BLSO surfaces were investigated, which are applicable for many potential devices using BSO heterostructures. Understanding and controlling the band bending and the interfacial boundary conditions is crucial for the devices involving heterostructures. Analyzing electrical properties of the δ -doped system will help us understand them. Their characterization can be applied to 2DEG analysis because the dopant formed into sheets is the most suitable profile to understand 2DEG system. Currently the main focus of BSO is the 2DEG formed at the LIO/BLSO interface [13,14], which is believed to be a quantum well of width smaller than 2 nm on the BLSO side [15]. Such 2DEG state can be simulated with the δ -doped BSO system. Theoretical calculation using Poisson-Schrödinger (P-S) equation based on the basic principles of band bending will be helpful in interpreting the complex 2DEG system since they show similarities in the experiments.

2.2. Experiment and calculation details

All depositions for δ -doped samples with a BSO/BLSO/BSO structure were performed by the pulsed laser deposition technique. Targets were ablated to deposit films with an energy fluence of approximately 1.5 J/cm^2 using a 248 nm wavelength KrF excimer laser. All targets were manufactured by TOSHIMA Manufacturing Co. in Japan. The depositions were conducted at $750 \text{ }^\circ\text{C}$ in 0.1 Torr oxygen pressure and the thickness of the films was deduced from the number of laser pulses and the growth rate per pulse measured for a thick

film using a profiler as shown in Fig 2.1. MgO was used as the substrate for its excellent insulating properties [14] and for the lower deep acceptor density in the epitaxial BSO films grown on MgO than on STO [15,16]. Underneath the δ -doped layer a 60 nm BHO and 150 nm BSO buffer layer were used with the intent to reduce the threading dislocations on MgO substrates, which improves electrical and structural properties of BLSO on top [14,16,17]. The contacts were made by pressing Au-coated CuBe tips on the δ -doped samples, as shown in Fig 2.2(a). In some cases, depositing 4% BLSO pads using a stencil mask on the edges of the ion milled δ -doped samples, as shown in Fig 2.2(b), also produced good electrical contacts. Hall measurements were performed in a Van der Pauw geometry. Electrical properties were recorded with Keithely 4200SCS parameter analyzer and the measurement of temperature dependent properties were carried out using Physical Property Measurement System. Theoretical calculations were performed with a self-consistent 1D P-S band calculator designed by Snider [18]. It finds the eigenfunctions, energy eigenvalues and the resulting potential that satisfies 1D Poisson equation and Schrödinger equation self consistently. In the simulation of δ -doped BSO, I used three experimentally obtained main material parameters of BSO; electron effective mass, dielectric constant, and energy gap. And as the source of carrier, shallow donor (La doping) and deep acceptor (electron trap) were considered. A more detailed description of its use with appropriate materials parameters is given in Ref. 15.

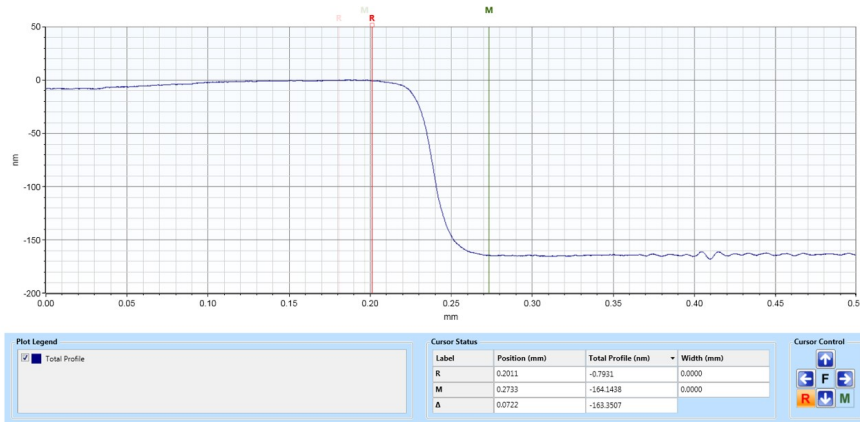


Figure 2.1 Profiler measurement of a 1% BLSO film deposited by 5000 pulsed of laser produced 163.35 nm, namely the growth rate of 0.03267 nm/pulse.

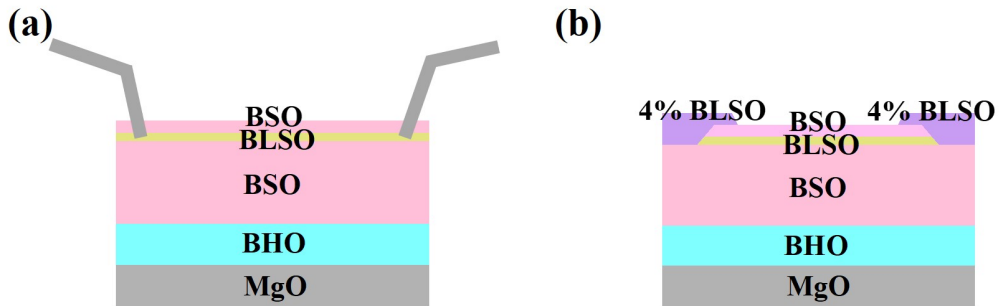


Figure 2.2 Two contact methods to measure the electrical properties of δ -doped samples. (a) Contacts made by pressing Au-coated CuBe tips. (b) Contacts by depositing 4% BLSO pads using a stencil mask on the edges of the ion milled δ -doped samples.

After deposition of 1~20 nm thick BLSO channel layer on the buffer layer, an undoped 20 nm BSO capping layer covered the BLSO channel layer in a structure shown in Fig 2.3(a). First, I investigated electrical properties while changing the doping ratio and thickness of BLSO layers of δ -doped system in order to understand the band bending in BSO systems. The experimental carrier densities are the red and the blue circles in Fig 2.3(b) as a function of the BLSO channel layer thickness. The measured n_{2D} values are not proportional to the channel layer thickness as predicted by the lines in Fig 2.3(b) that show

proportionally decreasing n_{2D} based on 20 nm BLSO sample. And the experimental results differ from the predicted values more as the BLSO thickness gets thinner. Less than 10 nm in 0.5% BLSO and 5 nm in 1% BLSO layer exhibit almost insulating properties even though the roughness of the sample surface is only about 1 nm, as shown in Fig 2.4. The carrier densities by the P-S calculation for the same structure are represented by the red and the blue lines in Fig 2.5(a) with the experimental results. In calculations, I introduced deep level acceptor states in the BSO, which represent cation vacancies including the threading dislocations caused by the lattice mismatch. The deep acceptor density of about $3 \times 10^{19} \text{ cm}^{-3}$ in the middle of the gap fits the experimental results at both doping ratios, as can be seen in Fig 2.5(a), consistent with our previous results [15,16].

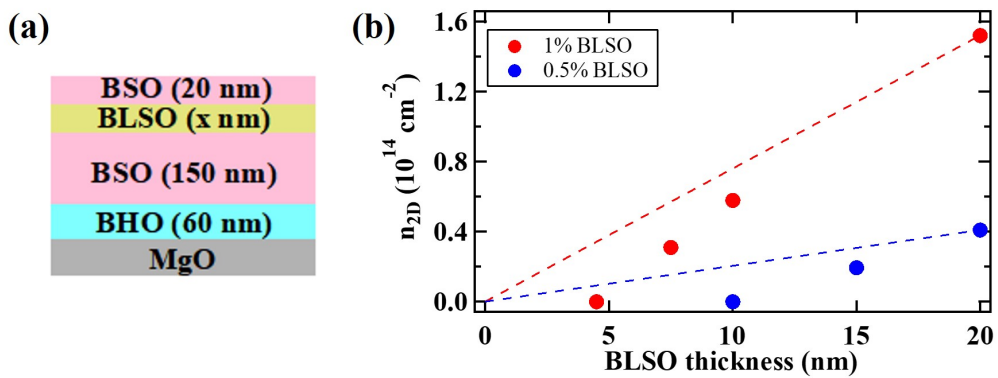


Figure 2.3 (a) Structure of δ -doped BSO to measure the BLSO thickness dependent electrical properties. (b) Experimental results of 2D carrier densities with different BLSO thicknesses with blue and red dots in 0.5% and 1% La-doped BLSO layer. The lines are guides of the predicted 2D carrier density proportional to the channel thickness based on the experimental data from BLSO 20 nm sample.

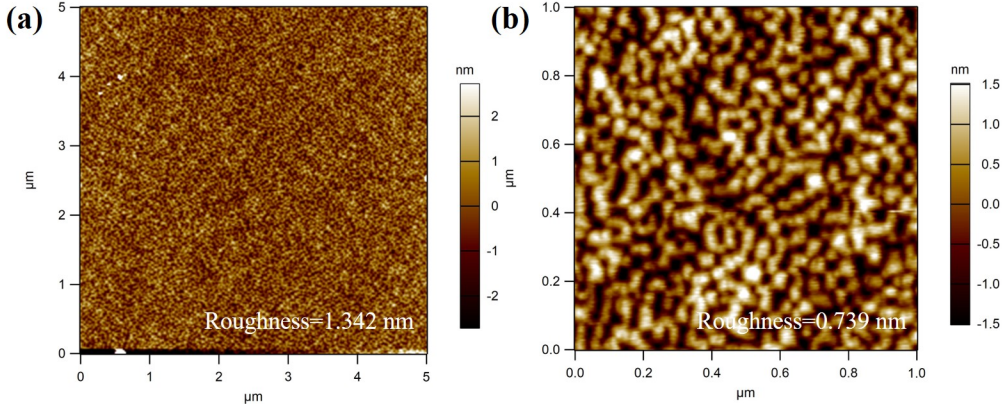


Figure 2.4 AFM images of the 1% La-doped BSO surface on MgO substrate with 60 nm BHO and 150 nm BSO buffer layer in two different lateral scales.

2.3. Band bending of BaSnO₃/(Ba,La)SnO₃ interface

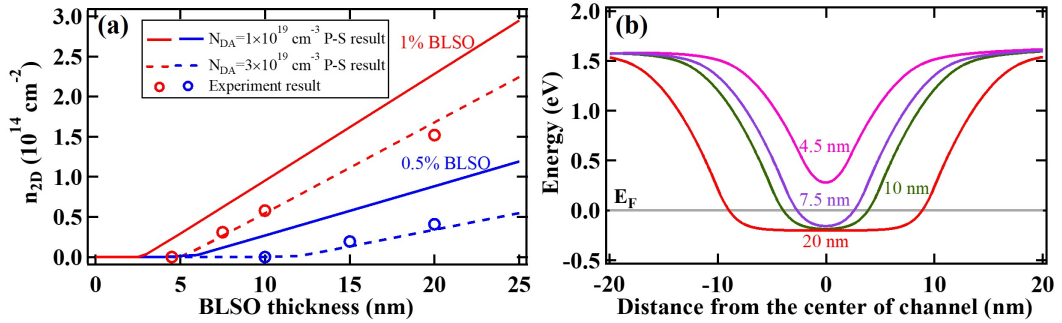


Figure 2.5 Experimental and calculated results for δ -doped BSO films. (a) 2D carrier density of δ -doped BSO films with different BLSO thicknesses. The BLSO layer is doped with 0.5% La in blue and 1% in red. The lines are the results calculated with 1×10^{19} and $3 \times 10^{19} \text{ cm}^{-3}$ deep acceptor density. The experimental results in circles fit well with the calculations at about $3 \times 10^{19} \text{ cm}^{-3}$ deep acceptor density. (b) Calculated results of conduction band bending for 1% δ -doped samples with different thicknesses of 1% BLSO channel layer.

Fig 2.5(b) illustrates the band bending of the δ -doped samples with 1% La doping of various BLSO channel layer thickness. Here, the “Ohmic” boundary condition is used at the end of the both undoped BSO layers. The “Ohmic” boundary condition sets charge neutrality condition that the Fermi level must be in the middle of the bandgap, as one can easily think of for an ideal undoped BSO layer. The conduction band of the 1% δ -doped

BSO layer is influenced by the undoped BSO layers on both sides of it because the Fermi level of the undoped BSO is in the center of the bandgap, and the Fermi level is above the conduction band minimum in the 1% BLSO channel layer. Therefore, continuous band bending moves the conduction band of BLSO channel layer near its surfaces. This is consistent with what have been observed in δ -doped Si system [19]. In 4.5 nm thick 1% δ -doped BSO sample, which did not show conductance experimentally, the conduction band minimum is above the Fermi level. As the thickness of the BLSO increases, the conduction band minimum starts to go down, eventually reaching -0.2 eV relative to the Fermi level, namely the value for the bulk 1% doped BLSO.

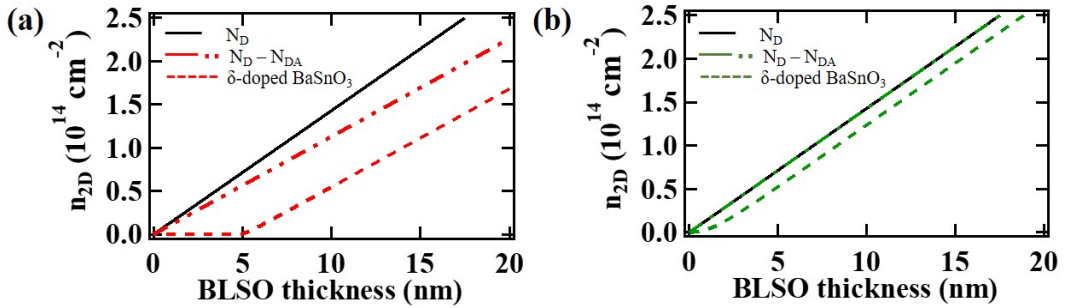


Figure 2.6 The 2D carrier density as the 1% BLSO channel thickness changes at a deep acceptor density of (a) $3 \times 10^{19} \text{ cm}^{-3}$ and (b) $1 \times 10^{17} \text{ cm}^{-3}$. The 2D carrier density of N_D is derived from BLSO with a shallow donor density of $1.43 \times 10^{20} \text{ cm}^{-3}$ of 1% doping, and $N_D - N_{DA}$ is from BLSO with shallow donor and deep acceptor. The 2D carrier density of the δ -doped BSO is from BLSO with shallow donor and deep acceptor in the δ -doping structure. N_D and $N_D - N_{DA}$ are results without considering band bending and δ -doped BSO is the result considering band bending.

The low Fermi levels, created by continuous band bending, are derived from the decrease in activation rate of shallow donor rather than more activated deep acceptors. They are clearly distinguished by checking the effect of the deep acceptor on band bending. Fig 2.6 shows n_{2D} value calculated from the BLSO channel that has donor density N_D ($1.43 \times 10^{20} \text{ cm}^{-3}$), both N_D and N_{DA} that make carrier density equal to the difference between donor

density and deep acceptor density ($1.43 \times 10^{20} \text{ cm}^{-3}$ - $3 \times 10^{19} \text{ cm}^{-3}$ in (a), $1.43 \times 10^{20} \text{ cm}^{-3}$ - $1 \times 10^{17} \text{ cm}^{-3}$ in (b)), and BLSO channel in δ -doped BSO structure with donor and deep acceptor, at each thickness of BLSO. In first two cases, band bending was not considered and BLSO channel in δ -doped BSO structure only considered continuous band bending. Fig 2.6 shows additional reduction of n_{2D} when the band bending is considered with the δ -doped structure compared to the values of N_D - N_{DA} that means 100% activated deep acceptors. The $1 \times 10^{17} \text{ cm}^{-3}$ of deep acceptor density is negligibly small value compared to the shallow donor density or $3 \times 10^{19} \text{ cm}^{-3}$ of deep acceptor density making N_D and N_D - N_{DA} almost same in Fig 2.6(b), but it also shows reduction of n_{2D} at δ -doped BSO structure. If the low Fermi level is due to increased activated deep acceptors, there should be no such reduction. However, n_{2D} decreased with the same trend at negligibly small value of deep acceptor density. Therefore, Fermi level lowering is from the lowered shallow donor density at the interface of BSO and BLSO.

2.4. Fermi level pinning of (Ba,La)SnO₃ surface

Another important characteristic of δ -doped samples is the effect of undoped BSO capping layer and the boundary conditions of the surface. I noticed that the BSO capping layer above the channel layer increases the conductance, as clearly shown in Fig 2.7(a). If one assumes that the conduction band on the surface of BLSO channel stays same as its bulk conduction band, as depicted in solid line of Fig 2.8(b), the carrier density of the channel layer should have a higher value without the BSO capping layer than with the BSO capping layer since there is no band bending due to the capping layer. But the opposite behavior was observed; BSO capping layer makes conductance enhancement. In Fig 2.7(b), I find n_{2D} of the δ -doped samples with and without a BSO capping layer of 0.5% and 1%

BLSO of various thicknesses. The results for the BSO capped sample of the structure in the Fig 2.3(a) inset are described as circles and the results without BSO capping layer are shown in triangles. The effect of the BSO capping layer is larger for 1% doped BLSO than for 0.5% BLSO; n_{2D} increased by about $2 \times 10^{13} \text{ cm}^{-2}$ in 1% samples and by about $0.5 \times 10^{13} \text{ cm}^{-2}$ in 0.5% samples. The different degree of increase in n_{2D} depending on the doping ratio will be explained in detail later with Fig 2.11.

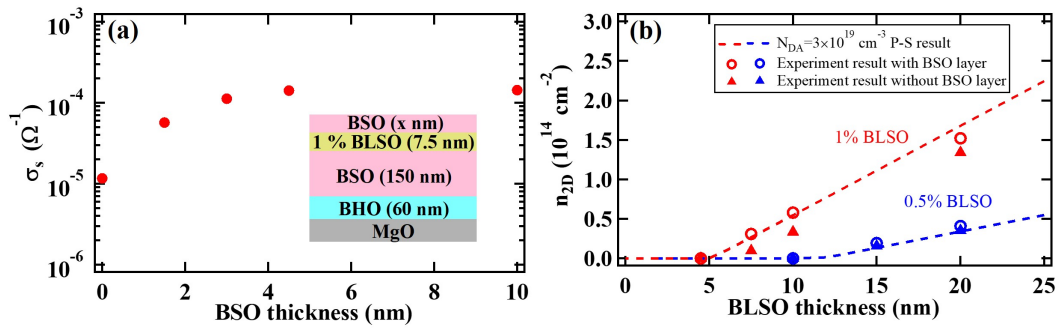


Figure 2.7 The effect of an undoped BSO capping layer over the BLSO layer. (a) Experimental conductance of the 1% 7.5 nm BLSO layer as a function of the thickness of the undoped BSO overlayer. (b) 2D carrier density of 0.5% and 1% BLSO layer with (circle) and without (triangles) 20 nm undoped BSO overlayer as a function of BLSO thickness. The 2D carrier density increases after depositing the undoped BSO overlayer.

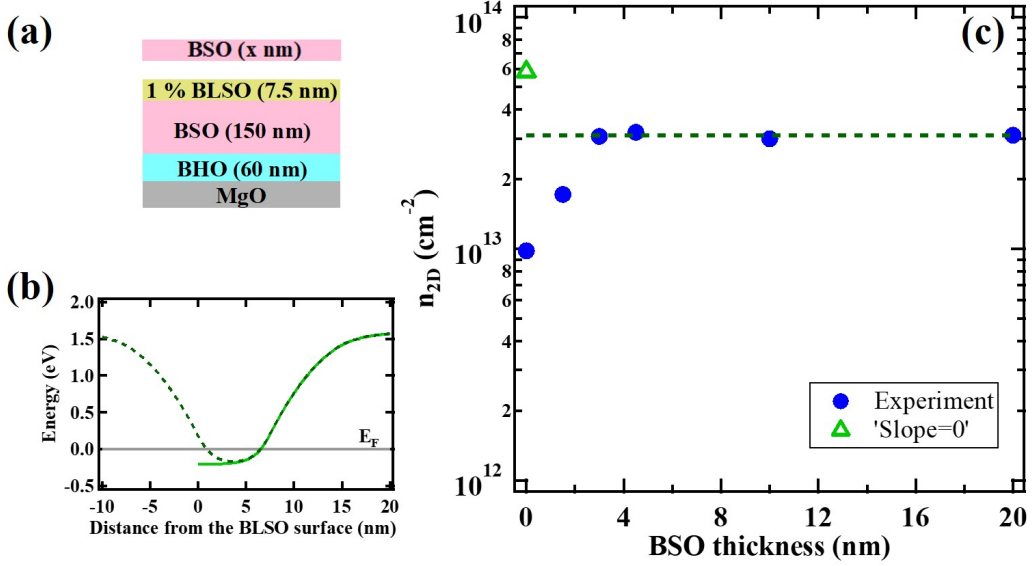


Figure 2.8 (a) Structure to investigate the effect of an undoped BSO capping layer over the BLSO layer. (b) Predicted conduction band bending before and after deposition of the capping layer in solid and dashed lines. (c) Experimental results in blue dots and calculated results of 2D carrier density before and after the capping layer in triangle and line with the band bending of (b).

We can first exclude the possibility that there is a dead layer on the surface of BLSO and the deposition of the BSO capping layer removes the dead layer on the surface. When judging from Fig 2.7(b) by shifting the x-axis scale, if there is a dead layer, it should be 2~3 nm thick for 1% BLSO and much thinner for 0.5% BLSO. If a dead layer idea is going to make sense, I expect it to be thicker for 0.5% BLSO, or at least same in both cases. Additionally, possibility of redistribution of dopants during the deposition of BSO layer seems remote as well since the mobility increased with the BSO capping layer and it is known that the mobility increases as the three-dimensional (3D) carrier density increases in films because presently scattering by charged defects such as dislocations is dominant [20]. Therefore, I move on to explain the experimental results with various surface boundary conditions.

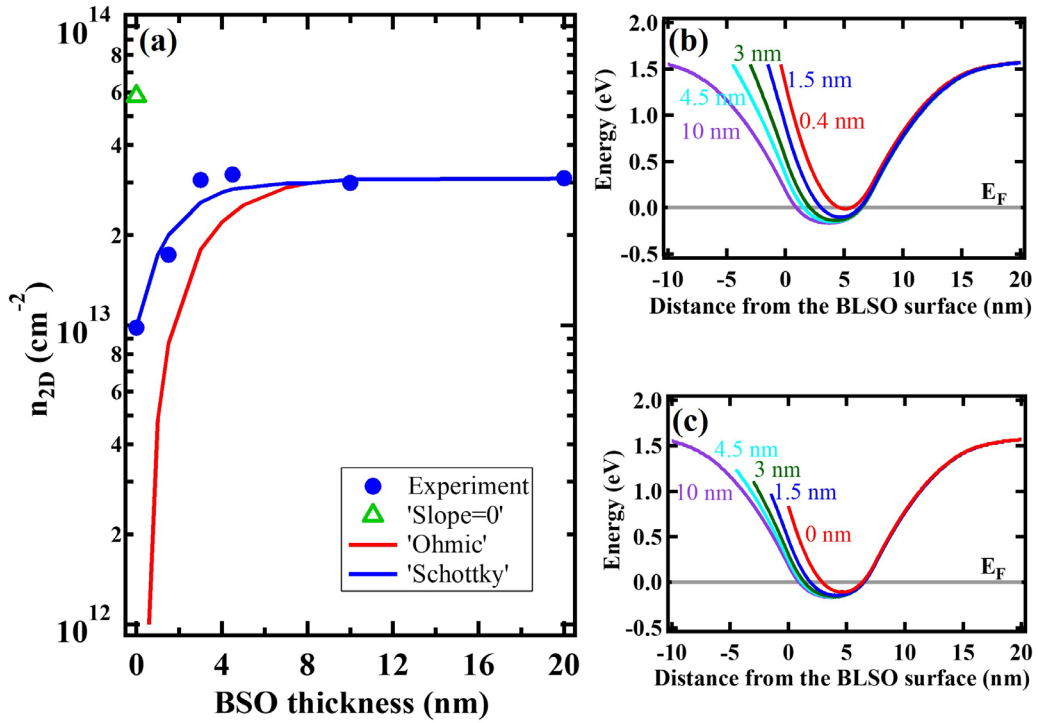


Figure 2.9 2D carrier density and band bending of δ -doped BSO films with 1% doped 7.5 nm BLSO layer with different boundary conditions. (a) Experimental and calculated carrier density using three kinds of boundary conditions as a function of the BSO capping layer thickness. (b) Band bending using “Ohmic” boundary condition showing similar trend to the experimental carrier density only in the thick BSO capping layer. Five cases of BSO capping layer thicknesses of 0.4, 1.5, 3.0, 4.5 and 10 nm described in experimental result in (a) are shown. (c) Band bending using “Schottky” boundary condition well fitted to the experimental carrier density. Five cases of BSO capping layer thicknesses of 0.0, 1.5, 3.0, 4.5 and 10 nm described in experimental result in (a) are shown.

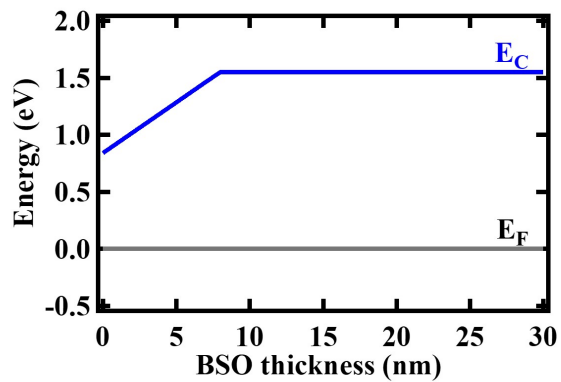


Figure 2.10 The position of the conduction band minimum in comparison to the Fermi level used for the “Schottky” boundary condition in Fig 2.9 (c).

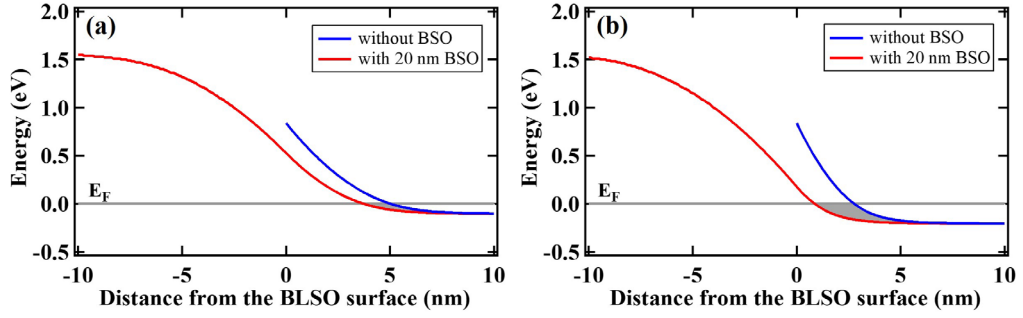


Figure 2.11 Calculated band bending of δ -doped BSO films by the “Schottky” boundary conditions same as in Fig 2.10 using $2.7 \times 10^{19} \text{ cm}^{-3}$ deep acceptor density. The shaded areas represent the differences between with and without the capping layer in the case of (a) 20 nm thick 0.5% BLSO and (b) 20 nm thick 1% BLSO.

In order to predict how different boundary conditions will affect n_{2D} , I employ the P-S simulation. In Fig 2.8, $2.7 \times 10^{19} \text{ cm}^{-3}$ deep acceptor density in BSO was used because slightly smaller deep acceptor density fits better for this case of 7.5 nm 1% BLSO. Fig 2.8(c) shows n_{2D} of the experimental data in blue dots and those of the predicted values as mentioned earlier in green triangle. Naively, BLSO without BSO capping layer can be thought of as having its surface Fermi level equal to its bulk value with the conduction band minimum at -0.2 eV for the 1% La doped BSO relative to the Fermi level at 0 eV. In this case, the carrier density should be $5.83 \times 10^{13} \text{ cm}^{-2}$ indicated by the green triangle in Fig 2.8(c), which also represents the “Slope=0” boundary condition in Fig 2.8(b). As a BSO capping layer is added, I expect it to decrease towards the dashed line at $3.1 \times 10^{13} \text{ cm}^{-2}$ in Fig 2.8(c) with the change in band bending of Fig 2.8(b). However, the experimental results show opposite trend to such expected carrier density change. Therefore, we consider other boundary conditions to explain the experimental results.

The “Ohmic” boundary condition, which puts the Fermi level at the midgap regardless of 1% doping, shown in Fig 2.9(b) can make similar trend of experimental carrier density change seen in red line of Fig 2.9(a). But it underestimates the n_{2D} , especially for thin BSO

capping layer cases. It only explains the result of the thick BSO capping layer. Moreover, the carrier density by simulation with the “Ohmic” boundary condition approaches to the thick limit more slowly than the experimental results which saturate at 3~5 nm BSO.

As a result, an alternative middle approach is necessary. I introduced the “Schottky” boundary condition on the δ -doped BSO surface. The “Schottky” boundary condition refers to the pinned Fermi level at the surface. Appropriate “Schottky” boundary conditions (the difference between the conduction band minimum and the Fermi level on the surface) for fitting with experimental results were established, which continuously vary from 0.84 eV to 1.55 eV as the BSO capping layer becomes thicker in Fig 2.10. 1.55 eV Schottky boundary condition is identical with the “Ohmic” condition, being exactly the half the bandgap of BSO. The corresponding band diagrams are in Fig 2.9(c). Compared to the “Ohmic” boundary condition, the potential wells are deeper due to the higher Fermi level on the surface with thin BSO capping layer. In Fig 2.9(a), n_{2D} of the “Schottky” boundary condition is plotted as a blue line, which fits the experimental results much better than the results with the “Ohmic” boundary conditions including n_{2D} without a BSO capping layer, $9.8 \times 10^{12} \text{ cm}^{-2}$. The saturation thickness of BSO capping layer is lower than that by the “Ohmic” boundary condition and fits better with the experimental data. The conduction band minimum for 1% doped BLSO in bulk is lower than the Fermi level, but the analysis of its δ -doped system suggests that the conduction band minimum is higher than the Fermi level on the surface of 1% doped BLSO due to the Fermi level pinning on its surface.

This δ -doped BSO system has Fermi level pinning without a capping layer, and the pinning continuously disappears as the undoped capping layer thickness increases. Well-known semiconductors, GaAs and STO have already been studied for this in their δ -doped systems. δ -doped GaAs was reported to have the Fermi level pinning in the semiconductor surface of the doped GaAs layer [2,21,22]. However, δ -doped STO is reported to have no

change in its valence band of δ -doped layer, based on Fermi level in comparison to the doped bulk in the X-ray photoelectron spectroscopy (XPS) results [23]. If there had been band bending like our BSO system in Fig 2.5(b) with thin doped channel layer, one would expect a shift in the valence band energy.

In other transparent conducting oxides such as ZnO, CdO, In₂O₃ and SnO₂, surface states and native defects, for example oxygen vacancies, are known to make downward band bending on the surface, rendering the surface more conductive [24-28]. For example, unintentionally and Sb doped SnO₂ are reported to have a Fermi level pinning on the surface in XPS studies [28], similar with BSO system without the capping layer but the band bending direction is opposite to the case of BLSO here. However, a similar phenomenon of upward band bending on the surface was reported in the case of La-doped STO [29]. Recently Fermi level pinning on the surface of BLSO which bends the conduction band upward was deduced using UV angle-resolved photoemission spectroscopy (ARPES) on BLSO surface [30], when compared with the bulk property measured by X-ray [31]. This not only agrees with my experiments in its bending direction but the upward shift of the conduction band by 1.0 eV on the surface also agrees with my number (the difference in Fig 2.8(b) and 2.9(c) on BLSO surface). Such shift of the Fermi level towards the midgap has been seen in many semiconducting surfaces including Si, GaAs, and GaN [32-34]. However, since BSO has significant and persistent photoconductivity [30, 35] and UV can move the Fermi level closer to the conduction band minimum even in undoped BSO, more careful investigation is needed for the accurate analysis, especially without the photoconductivity effect caused by UV.

Now, I will see how the different doping levels in the channel will affect the amount of n_{2D} increase with the undoped capping layer. The increase in n_{2D} on 0.5% BLSO layer was much less than on 1% BLSO after deposition of the BSO capping layer. For example, 15

nm 0.5% BLSO has $0.37 \times 10^{13} \text{ cm}^{-2}$ increment (from $1.57 \times 10^{13} \text{ cm}^{-2}$ to $1.94 \times 10^{13} \text{ cm}^{-2}$) and there was $0.55 \times 10^{13} \text{ cm}^{-2}$ increment for 20 nm 0.5% BLSO (from $3.54 \times 10^{13} \text{ cm}^{-2}$ to $4.09 \times 10^{13} \text{ cm}^{-2}$) which are much smaller than the enhancement of about 2×10^{13} in 1% BLSO samples. The band bending results with and without the capping layer of 0.5% BLSO and 1% BLSO can explain this in Fig 2.11, using the same ‘‘Schottky’’ boundary condition of Fig 2.10. Fig 2.11(a) is the band bending with and without the 20 nm BSO capping layer of 0.5% BLSO and Fig 2.11(b) is the band bending with and without the 20 nm BSO capping layer of 1% BLSO. The 20 nm capping layer causes a larger band bending change in 1% BLSO in Fig 2.11(b) than in 0.5% BLSO in Fig 2.11(a). And from the shaded regions which represents the incremental n_{2D} after deposition of 20 nm undoped BSO capping layer, I can easily see higher doping makes higher increment due to the wider and deeper conduction band. However, this is based on an assumption that the pinned Fermi levels are the same for 0.5% and 1% doping rates. It is reported that the lower doped BLSO film has smaller upward bending of the conduction band, which will move the pinned Fermi level closer to the conduction band minimum [30]. In such case, the shaded area in Fig 2.11(a) will further shrink.

2.5. Temperature dependent electrical property

Equipped with some knowledge on the δ -doped BSO system, I examined the temperature dependent resistance characteristics of the δ -doped BSO system using 2% doped BSO as function of the channel layer thickness. I chose 2% doping because this can be useful for understanding the LIO/BLSO 2DEG system; the simulation results of such 2DEG [15] predicts the 3-dimensional carrier density inside the quantum well will be close to the value of 2% BLSO that will be explained in chapter 3. While the 0.5% and 1% δ -doped BSO in

Fig 2.5 were fitted with the deep acceptor density $3 \times 10^{19} \text{ cm}^{-3}$, in the case of the 2% BLSO samples fits were better with slightly lower deep acceptor density of $2 \times 10^{19} \text{ cm}^{-3}$ in Fig 2.12(a), indicating fluctuation of the deep acceptor states depending on the La doping level and the growth conditions. Fig 2.12(b) illustrates the resistance as a function of temperature of from 2K to room temperature, for different thicknesses of BLSO. BLSO samples thicker than 3 nm show metallic temperature dependence of decreasing resistance at the temperature lowers while thinner BLSO samples with high resistance and low carrier density show semiconductor-like temperature dependence. The data for the three thicknesses around the metal-semiconductor transition were magnified in Fig 2.12(c). These results have been shown to have similar properties to the δ -doped STO system [36], the GaAs system [5] and the V_O -doped BSO system [37], which all displayed transition from a weak localization to a strong localization as the resistance of the sample increases. However, the mobility values in our experiment are currently not high enough. In order to study 2D quantum phenomena with a δ -doped BSO system, it is necessary to develop the growth of BSO films with appropriate substrates. After solving this problem, δ -doped BSO can show different quantum phenomena like δ -doped STO that the d orbital consists conduction band, mentioned in introduction, because BSO has much larger atomic number than conventional semiconductors that have shown 2D phenomena, though BSO has conduction band of s and p orbital, same with conventional semiconductors.

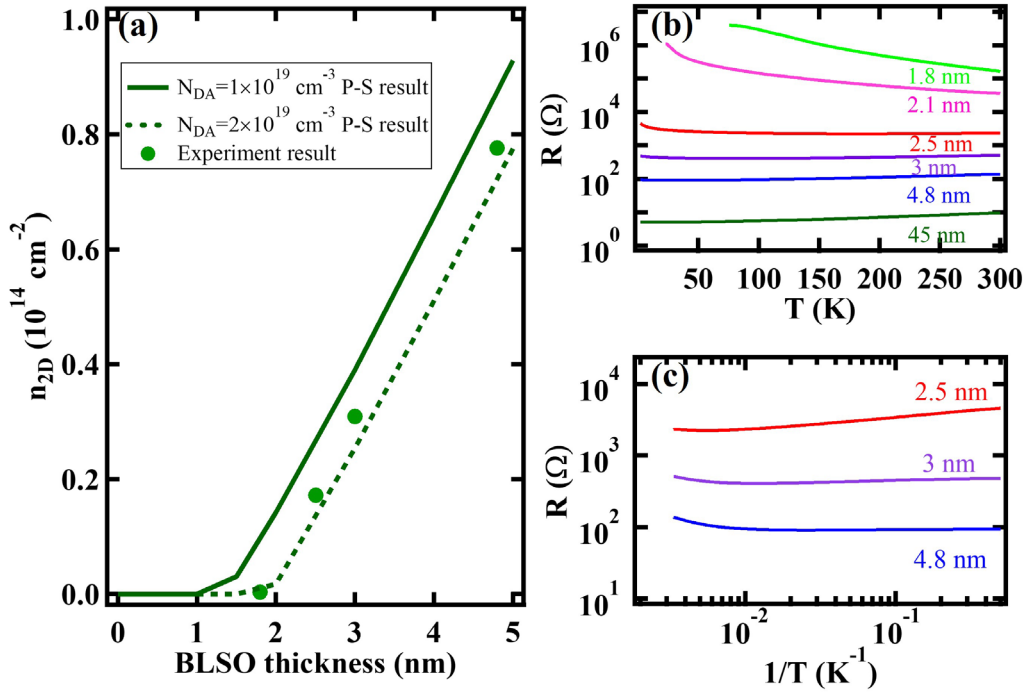


Figure 2.12 Properties of δ -doped BSO films using 2% La doping with the structure of Fig 2.3(a). (a) 2D carrier density with different BLSO thickness. The experimental results fit well with the calculation with about $2 \times 10^{19} \text{ cm}^{-3}$ deep acceptor density. (b)(c) Temperature dependent resistance of the δ -doped BSO, exhibiting transition from metal to semiconductor when the BLSO film becomes thinner.

2.6. Conclusion

In summary, δ -doped BSO system has been investigated for application to the device and quantum phenomena as in other semiconducting systems. I specifically focused on the electrical properties of δ -doped BSO resulting from the band bending and the surface boundary conditions applicable to the analysis of other heterostructures. The n_{2D} of the δ -doped sample were well explained by the band bending by P-S simulation. I reported on the Fermi level pinning on the surface of the 1% BLSO towards the midgap. I have also presented the metal-semiconductor transition as a function of thickness of the δ -doped BLSO. Since the δ -doped BSO system has a quasi-quantum well by band bending, similar to the δ -doped GaAs and STO systems in which quantum phenomena were observed, these studies will be helpful in understanding heterostructures including the 2DEG state at LIO/BLSO interface.

References

- [1] J. J. Harris, *J. Mater. Sci.* **4**, 93 (1993).
- [2] E.F. Schubert, *J. Vac. Sci. Technol. A* **8**, 2980 (1990).
- [3] H. J. Gossmann and E. F. Schubert, *Crit. Rev. Solid State Mater. Sci.* **18**, 1 (1993).
- [4] J. J. Harris, R. Murray and C. T. Foxon, *Semicond. Sci. Technol.* **8**, 31 (1993).
- [5] R. Dötzer, K. J. Friedland, R. Hey, H. Kostial, H. Miehling, and W. Schoepe, *Semicond. Sci. Technol.* **9**, 1332 (1994).
- [6] T. Ferrus, B. Goutiers, J. Galibert, L. Ressler, and J. P. Peyrade, *Superlatt. Microstruct.* **29**, 99 (2001).
- [7] H. Ohta, S. Kim, Y. Mune, T. Mizoguchi, K. Nomura, S. Ohta, T. Nomura, Y. Nakanishi, Y. Ikuhara, M. Hirano, H. Hosono, and K. Koumoto, *Nature Mater.* **6**, 129 (2007).
- [8] A. Ohtomo and H. Y. Hwang, *Nature* **427**, 423 (2004).
- [9] N. Reyren, S. Thiel, A. D. Caviglia, L. F. Kourkoutis, G. Hammerl, C. Richter, C. W. Schneider, T. Kopp, A.-S. Rüetschi, D. Jaccard, M. Gabay, D. A. Muller, J.-M. Triscone, and J. Mannhart, *Science* **317**, 1196 (2007).
- [10] Y. Kozuka, M. Kim, C. Bell, B. G. Kim, Y. Hikita and H. Y. Hwang, *Nature* **462**, 487 (2009).
- [11] Y. Matsubara, K.S. Takahashi, M.S. Bahramy, Y. Kozuka, D. Maryenko, J. Falson, A. Tsukazaki, Y. Tokura and M. Kawasaki, *Nat. Commun.* **7**, 11631 (2016).
- [12] B. Jalan and S. Stemmer, *Phys. Rev. B* **82**, 081103 (2010).
- [13] U. Kim, C. Park, Y. M. Kim, J. Shin, and K. Char, *APL Mater.* **4**, 071102 (2016).
- [14] Y. Kim, Y. M. Kim, J. Shin, and K. Char, *APL Materials* **6**, 096104 (2018).
- [15] Y. M. Kim, T. Markurt, Y. Kim, M. Zupancic, J. Shin, M. Albrecht, and K. Char, *Sci. Rep.* **9**, 16202 (2019).
- [16] J. Shin, Y. M. Kim, Y. Kim, C. Park, and K. Char, *Appl. Phys. Lett.* **109**, 262102 (2016).
- [17] C. Park, U. Kim, C. J. Ju, J. S. Park, Y. M. Kim, and K. Char, *Appl. Phys. Lett.* **105**, 203503 (2014).
- [18] I.-H. Tan, G. Snider, and E. Hu, *J. Appl. Phys.* **68**, 4071 (1990).
- [19] J. A. Miwa, P. Hofmann, M. Y. Simmons, and J. W. Wells, *PRL* **110**, 136801 (2013).

- [20] H. J. Kim, U. Kim, H. M. Kim, T. H. Kim, H. S. Mun, B.-G. Jeon, K. T. Hong, W.-J. Lee, C. Ju, K. H. Kim, and K. Char, *Appl. Phys. Express* **5**, 061102 (2012).
- [21] T. M. Hsu, W. C. Lee, and J. R. Wu, *Phys. Rev. B* **51**, 17215 (1995).
- [22] T. M. Hsu, Y. C. Tien, N. H. Lu, S. P. Tsai, D. G. Liu, and C. P. Lee, *J. Appl. Phys.* **72**, 1065 (1992).
- [23] A. M. Kaiser, A. X. Gray, G. Conti, B. Jalan, A. P. Kajdos, A. Gloskovskii, S. Ueda, Y. Yamashita, K. Kobayashi, W. Drube, S. Stemmer, and C. S. Fadley, *Appl. Phys. Lett.* **100**, 261603 (2012).
- [24] P. D. C. King and T. D. Veal, *J. Phys.: Condens. Matter* **23**, 334214 (2011).
- [25] O. Schmidt, P. Kiesel, C. G. Van de Walle, N. M. Johnson, J. Nause, and G. H. Döhler, *Jpn. J. Appl. Phys., Part 1* **44**, 7271 (2005).
- [26] P. D. C. King, T. D. Veal, P. H. Jefferson, J. Zúñiga-Pérez, V. Muñoz-Sanjosé, and C. F. McConville, *Phys. Rev. B* **79**, 035203 (2009).
- [27] P. D. C. King, T. D. Veal, D. J. Payne, A. Bourlange, R. G. Egdell, and C. F. McConville, *PRL* **101**, 116808 (2008).
- [28] T. Nagata, O. Bierwagen, M. E. White, M. Y. Tsai, Y. Yamashita, H. Yoshikawa, N. Ohashi, K. Kobayashi, T. Chikyow, and J. S. Speck, *Appl. Phys. Lett.* **98**, 232107 (2011).
- [29] A. Ohtomo, and H. Y. Hwang, *Appl. Phys. Lett.* **84**, 1716 (2004).
- [30] E. B. Lochocki, H. Paik, M. Uchida, D. G. Schlom, and K. M. Shen, *Appl. Phys. Lett.* **112**, 181603 (2018).
- [31] Z. Lebens-Higgins, D. O. Scanlon, H. Paik, S. Sallis, Y. Nie, M. Uchida, N. F. Quackenbush, M. J. Wahila, G. E. Sterbinsky, D. A. Arena, J. C. Woicik, D. G. Schlom, and L. F. J. Piper, *PRL* **116**, 027602 (2016).
- [32] M. Arita, K. Torigoe, T. Yamauchi, T. Nagaoka, T. Aiso, Y. Yamashita and T. Motooka, *Appl. Phys. Lett.* **104**, 132103 (2014).
- [33] M. D. Pashley, K. W. Haberern, R. M. Feenstra, and P. D. Kirchner, *Phys. Rev. B* **48**, 4612 (1993).
- [34] M. Grodzicki, K. Moszak, D. Hommel and G. R. Bell, *Appl. Surf. Sci.* **533**, 147416 (2020).
- [35] J. Park, U. Kim, and K. Char, *Appl. Phys. Lett.* **108**, 092106 (2016).
- [36] Y. Kozuka, M. Kim, H. Ohta, Y. Hikita, C. Bell, and H. Y. Hwang, *Appl. Phys. Lett.* **97**, 222115 (2010).
- [37] K. Ganguly, A. Prakash, B. Jalan, and C. Leighton, *APL Mater.* **5**, 056102 (2017)

Chapter 3. Two-dimensional electron gas at $\text{LaInO}_3/\text{BaSnO}_3$ interface

In this chapter, I will discuss another 2D system based on BSO at the interface between LIO and BSO. I will focus on a new property of LIO/BLSO polar interface using MgO substrates. First, the growth of well-formed LIO/BLSO interface structures on non-perovskite MgO substrates was confirmed by reciprocal space mapping image and transmission electron microscopy. And I measured electrical properties as a function of the La doping rate of the BLSO layer and found that the LIO/BLSO polar interface shows conductance enhancement after the deposition of the polar LIO layer on the BLSO layer, in agreement with our earlier results on STO substrates. However, different electrical properties of the interfaces were found on MgO from those on STO substrates; I observed conductance enhancement even at the interface with undoped BSO on the MgO substrates. I attribute such different behavior to the difference in the Fermi levels of BSO on MgO and STO substrates, either due to the larger donor density or the smaller acceptor density in BSO on MgO. Using such nominally undoped interface, I fabricated the field effect transistors and present their performances with $I_{\text{on}}/I_{\text{off}} \sim 10^9$. I also investigated the temperature dependent resistance of the interface and compared it with δ -doped BSO system.

3.1. Introduction

Perovskite heterostructures have been attracting attention due to their interesting interfacial properties such as superconductivity and ferromagnetism [1-4]. In particular, 2DEG at the interface of perovskite heterostructures shows high charge carrier density [5], which can enable high electron mobility transistors to be used in high power and high frequency devices. Similar with the 2DEG interfaces of a wurtzite structure in AlGaIn/GaN and MgZnO/ZnO with the mobility of 160,000 [6] and 180,000 cm^2/Vs [7], respectively, in which polarization plays a major role, LAO/STO interface of a perovskite structure exhibits mobility over 10,000 cm^2/Vs [8]. One of the reasons for such high mobility values

is that there are no intentional dopants which cause ionized impurity scattering. Although the exact mechanism of these 2DEGs has not yet been fully elucidated [9-12], 2DEG in a perovskite structure can be used in various places, especially in combination with a material with a novel characteristic of the same perovskite structure.

The BSO is another perovskite material that shows high mobility value of $320 \text{ cm}^2/\text{Vs}$ at 3D carrier density of $8.0 \times 10^{19} \text{ cm}^{-3}$ in addition to high oxygen stability [13, 14]. In LIO/BLSO perovskite interface, a 2DEG-like behavior was observed; conductance enhancement by more than 10^4 was observed when LIO is deposited on a BLSO film, suggesting that a 2DEG-like layer has been created at the interface between BLSO and LIO [15]. Subsequent experimental results have shown that the role of La diffusion or oxygen vacancy at the interface can be ruled out and the polarization of LIO at the interface plays an important role. The simulation results, which will also be explained in chapter 4, using 1D P-S program developed by Gregory Snider, show that a potential well of 1~2 nm width is created at this interface [16, 17], when taking into account the materials properties such as the effective mass, the dielectric constant, and the band alignment [14, 18-22]. The 1~2 nm width is consistent with the recent thermoelectric power measurement of 3D and 2D BSO materials[23].

To ensure that such 2DEG-like behavior is indeed a 2D behavior, we should observe quantized Landau levels with the Shubnikov-de Haas oscillation [24] or quantum Hall effect [25] when the sufficiently large magnetic field is applied at a sufficiently low temperature. These phenomena can be seen in the technically possible range of temperature and the magnetic field when the films possess sufficiently large mobility. Although such phenomena were observed for Si and GaAs 2DEG [26-29], it is yet difficult at the interface of LIO/BLSO because of its current mobility value around $100 \text{ cm}^2/\text{Vs}$, limited by defects such as the threading dislocations [5].

The MgO substrates possess a large bandgap and good oxygen stability [30]. Its lattice constant is 4.212 Å [31], and the lattice mismatch with BSO is smaller than that of the STO substrate which has the lattice constant of 3.9 Å [32]. Recently it has been reported that the BSO films on MgO substrates have good electrical properties [33]. Although the MgO substrates are of a non-perovskite structure, the characteristics of the BSO films, for example their mobilities, on the MgO substrates were as good as those on the STO substrate. I investigated the 2DEG-like LIO/BSO interface using MgO substrates and found different results from such interface on STO substrates. I will explain such different 2DEG behavior qualitatively with the structural difference and the resulting Fermi level shift. Subsequently, field effect was studied by fabricating all-perovskite field effect transistors and a very high on/off ratio of 10^9 was observed, which can be attributed to highly insulating nature of MgO substrates.

3.2. Structural properties of LaInO₃/BaSnO₃ interface

In all experiments, the samples were made by pulsed laser deposition technique and the targets were ablated with an energy fluence of about 1.3 J/cm² using a KrF excimer laser with a wavelength of 248 nm. The deposition was carried out at 750 °C with 0.1 Torr oxygen pressure in a typical base pressure of 1.0×10^{-6} Torr.

We first confirmed that the interface between the films is well formed on MgO substrates having a larger lattice constant than the films and a different crystalline structure. For this, a sample was deposited on a MgO substrate in the order of 60 nm BHO buffer layer, 162 nm BSO buffer and channel layer, and 100 nm LIO. A BHO buffer with a larger bandgap and a lattice constant of 4.189 Å [34], which is closer to MgO than to BSO, was used first before the usual BSO buffer to enhance the buffer effect [33]. Fig 3.1(a), the θ - 2θ x-ray

diffraction pattern, shows (002) peaks of entire layers of the sample. The leftmost peak is the MgO substrate, and in turn, peaks of BHO, LIO and BSO are shown. Considering that there are no peaks of the secondary phase and other crystalline planes, all films are epitaxially grown well along the orientation of the MgO substrate. However, the full width half maximum (FWHM) values of the rocking curves of the BSO and LIO films are 0.63° and 0.74° , respectively, while the FWHM values on the STO substrate are 0.09° for BSO and 0.52° for LIO [21]. It is believed that the larger FWHM values on MgO are due to the non-perovskite structure of MgO.

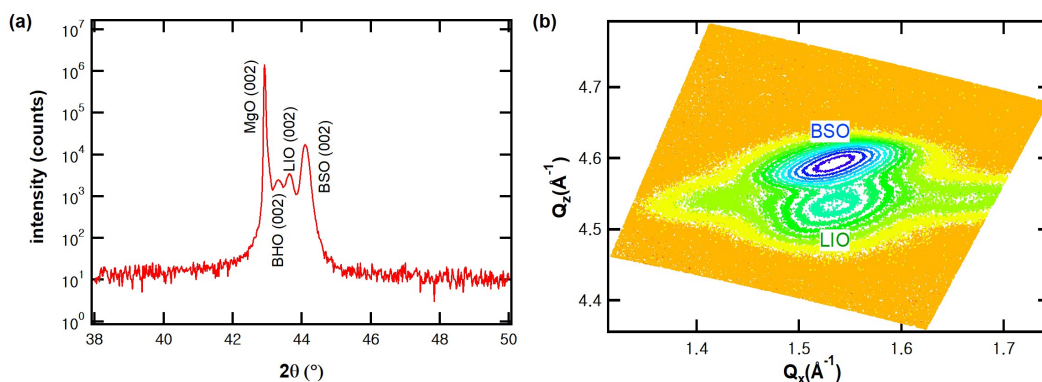


Figure 3.1 XRD pattern of a sample with LIO/BSO interface grown on [001] MgO substrate. (a) θ - 2θ diffraction peaks corresponding to the (002) plane of substrate, buffer layers, BSO and pseudocubic LIO. (b) RSM result of the LIO/BSO interface layers.

Fig 3.1(b) shows the reciprocal space mapping (RSM) scan around the peak of the (103) plane of the perovskite structure. These show how the interfaces grown on the non-perovskite MgO substrate and the perovskite STO substrate differ. There are two peaks in the RSM on the MgO substrate in Fig 3.1(b). The upper peak with the highest intensity belongs to BSO and the lower peak is due to LIO. When compared with similar RSM data on STO from the previous report [21], it is clear that the BSO and LIO layers deposited on STO substrates show less mosaicity than those on MgO substrates. The side lobes in the

LIO peaks are probably due to the orthorhombic domains in LIO. The in-plane lattice constant of BSO is $a = 4.126 \text{ \AA}$, and the out-of-plane lattice constant is $c = 4.104 \text{ \AA}$ on the MgO substrates. LIO has values of $a = 4.128 \text{ \AA}$ and $c = 4.157 \text{ \AA}$. In comparison, the lattice constants of BSO on STO substrates are $a = 4.107 \text{ \AA}$ and $c = 4.127 \text{ \AA}$ and the lattice constants of LIO are $a = 4.111 \text{ \AA}$ and $c = 4.150 \text{ \AA}$. The bulk lattice constants of BSO and LIO are 4.116 \AA and 4.118 \AA (pseudocubic), respectively [13, 22]. Films are slightly under tensile strain on MgO substrates and compressive strain on STO substrates. No peak corresponding to the lattice constant of BHO was observed because it is out of the range we scanned.

Scanning transmission electron microscopy (STEM) was performed to see the interface structure on the MgO substrates in high resolution. The sample used for TEM has the layers of 60 nm BHO buffer layer, 230 nm BSO buffer and channel layer, and 370 nm LIO on top of them. In Fig 3.2 (a) the entire layers on an MgO substrate can be seen with a large density of threading dislocations (TDs) in each layer. Fig 3.2 (b) shows the interface between BHO and BSO. I observed misfit dislocations at the interface between the MgO substrate and the BHO film as well as between BHO and BSO and they turn into a large density of TDs. Although the density of TDs decreases as the buffer layers become thicker, the roughness of the surface increases simultaneously. The TD density at the 2DEG-like channel is roughly $2.7 \times 10^{11}/\text{cm}^2$, which is slightly larger than that in the LIO/BSO interface on the STO substrate [35]. Fig 3.2(c) is the image of LIO/BSO interface in high resolution. I can confirm that it is coherently epitaxial without any misfit dislocations, making it difficult to distinguish between LIO and BSO.

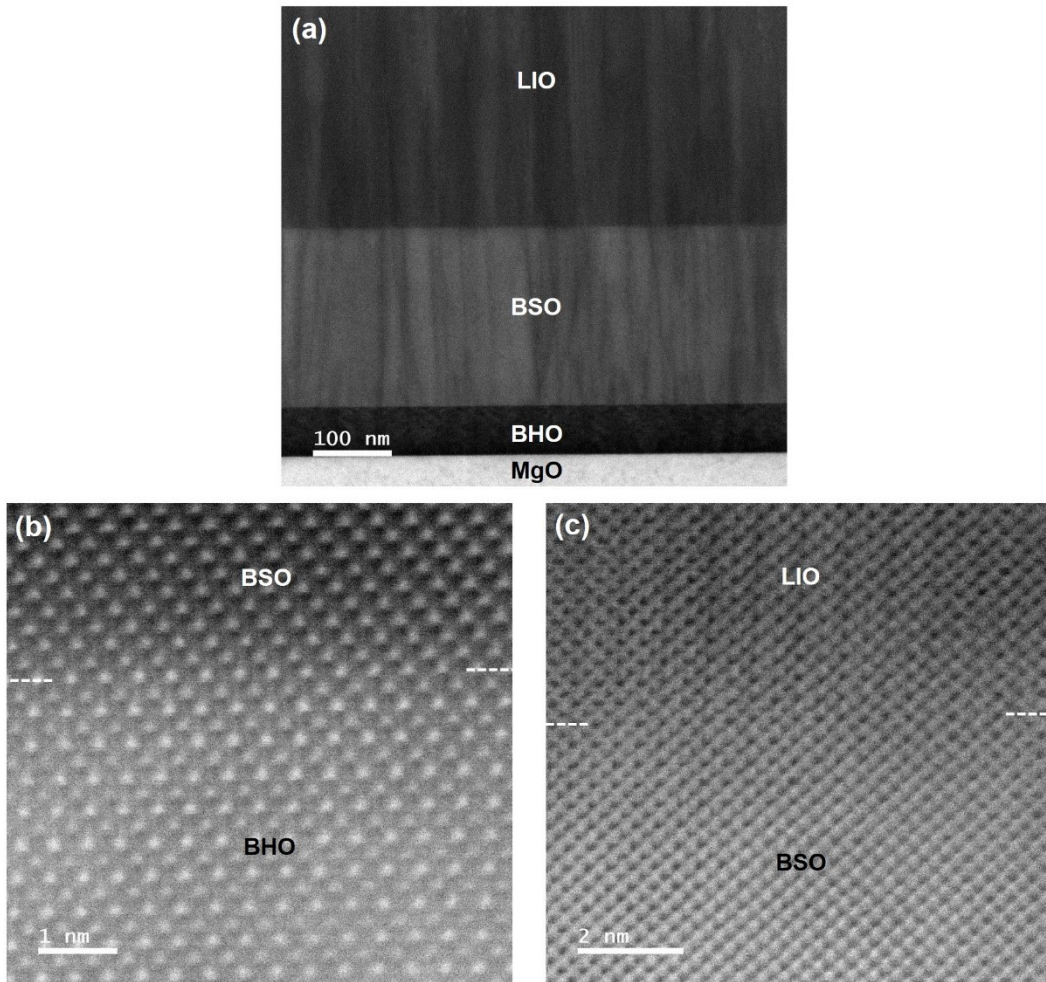


Figure 3.2 Structural properties of the interface on MgO substrate seen in STEM images. (a) Overall image from the substrate to LIO layer, showing a large TD density in each film. (b) BSO/BHO interface (c) LIO/BSO interface which is coherently epitaxial.

In AFM study of the BLSO surface, as shown in Fig 3.3, I have never observed a terrace structure with unit cell height steps in spite of its roughness less than a unit cell height. I think there is no specific termination layer in our process and the surface layer is mixed with BaO and SnO₂ layers. This is not surprising since BLSO ceramic target were used for our PLD process.

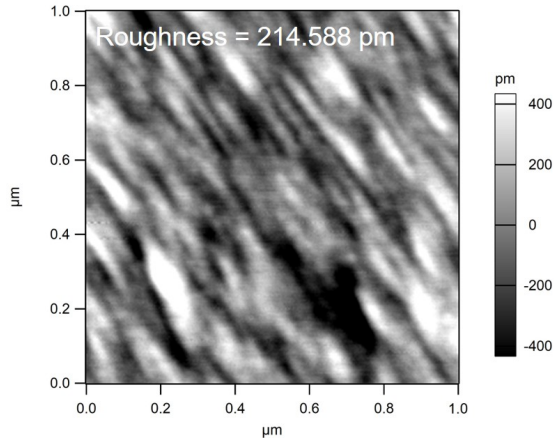


Figure 3.3 AFM image of the surface of a 0.2 % La-doped BSO film, showing roughness less than a unit cell height. No unit cell height structure has been observed.

3.3. Electrical properties of $\text{LaInO}_3/\text{BaSnO}_3$ interface

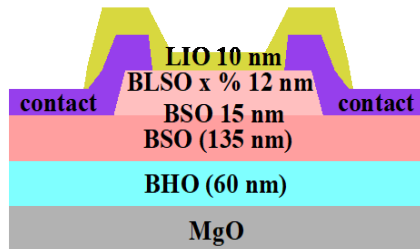


Figure 3.4 LIO/BLSO structure to measure electrical properties varying La doping rate of the channel layer.

Next, in order to see electrical characteristics of the interface on the MgO substrate, I made the same patterns of interface structure as in our previous report [5] with the structure of Fig 3.4. The BHO and BSO buffer was grown on the overall area of the 5 mm x 5 mm substrate and the 2 mm x 2 mm square patterned BLSO channel was deposited while changing the doping rate. Subsequently, the contact layer was deposited in the four corners of the channel, using 4 % BLSO. On top of this, 10 nm thick LIO layer covering the channel

with a 3.2 mm × 3.2 mm square shape was deposited. I measured the electrical properties such as conductance, carrier density, and mobility using the Van der Pauw method and Hall measurement while varying the La doping rate of the channel layer.

Fig 3.5(a) shows the conductance before and after the 2DEG-like interface was formed as a function of the doping rate of the channel. The lightly colored lines are the experimental results for the interface on STO substrates from our previous report [5]. On MgO substrates, the overall interface characteristics are similar to those on STO substrates. The LIO/BLSO interface shows a rapid increase in conductance when the interface is formed. Such conductance increase has been observed with 100 % probability in dozens of samples I have made. The increase of conductance is greatest in the 0.2 % BLSO channel. However, there is a clear difference from the interface on STO substrates. On STO substrates, the conductance hardly showed any increase after the LIO layer deposition when the channel layer is undoped, whereas the conductance of the nominally undoped interface on MgO substrates exhibits significant increase. Also, as shown in Fig 3.5(a), (b) and (c), the interface on MgO substrates at the same doping rate has higher conductance, carrier density, and mobility than on STO substrates. It looks as if, in the case MgO substrates, the data on STO substrates are shifted to the lower doping level. I believe the lower conductance level of BLSO on MgO substrates before LIO deposition is probably due to more insulating nature of the MgO substrates than STO substrates.

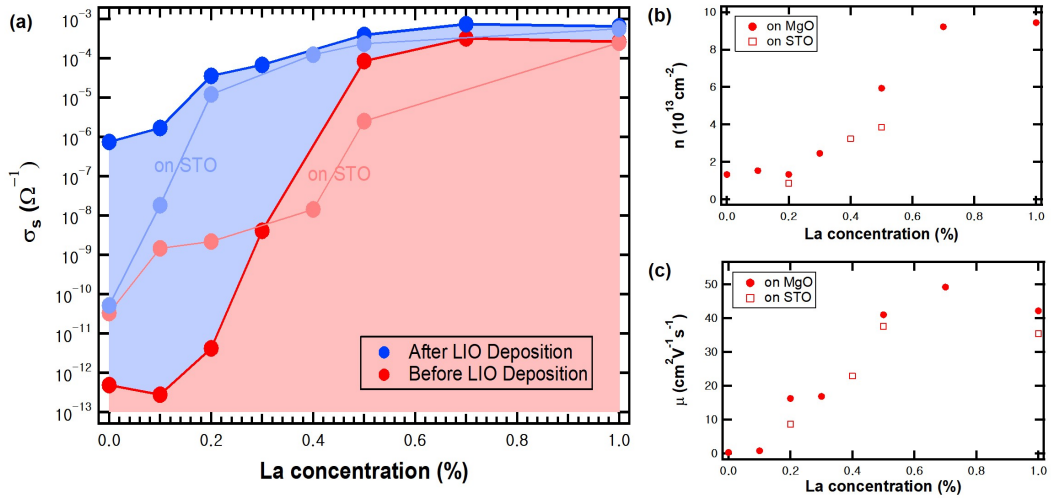


Figure 3.5 Transport properties of LIO/BLSO interface on MgO and STO substrate [5]. (a) The sheet conductance of the before and after the formation of LIO/BLSO interface as a function of the La doping rate of the BLSO channel on MgO and STO substrates. (b) Carrier density and (c) mobility value of LIO/BLSO interface while varying the La doping rate on MgO and STO substrates.

In our previous report, we showed the conductance enhancement at the LIO/BLSO interface is neither due to oxygen vacancy formation nor the La diffusion. Instead, 2DEG can be formed by band bending due to the interfacial polarization of LIO [5] and the large conduction band offset between BSO and LIO [21]. Since the interface conductance data on MgO substrates in Fig 3.5(a) look like the data on STO substrates except for the doping rate shift, I believe that the BSO on MgO either has larger donor density (oxygen vacancies) or smaller acceptor density (less cation vacancy in TD cores). This causes the effective doping on MgO to be slightly larger than that on STO with the same nominal La doping rate. The possibility of slightly more oxygen vacancies or slightly less cation vacancies in TD cores is consistent with slightly different structural characteristics of BSO on MgO, as shown in Fig 3.1(b). For example, the oxygen content $\text{BaSnO}_{3-0.001}$ instead of BaSnO_3 will be equivalent to extra 0.2 % La doping and such reduced oxygen stoichiometry can be generated by the tensile strain from the MgO substrate. Alternatively, slightly less cation vacancies in the TD cores on MgO will be equally equivalent.

The LIO thickness dependence of the conductance is shown in Fig 3.6. The 2DEG behavior, albeit small, arises as soon as the first unit cell of LIO is deposited, rapidly increasing the conductance by several orders of magnitude as more LIO is added. The conductance usually reaches the maximum value around 4 unit cell thickness of LIO and then starts to decrease very slowly, usually by about an order of magnitude when the LIO becomes as thick as 250 nm to be used as a gate oxide.

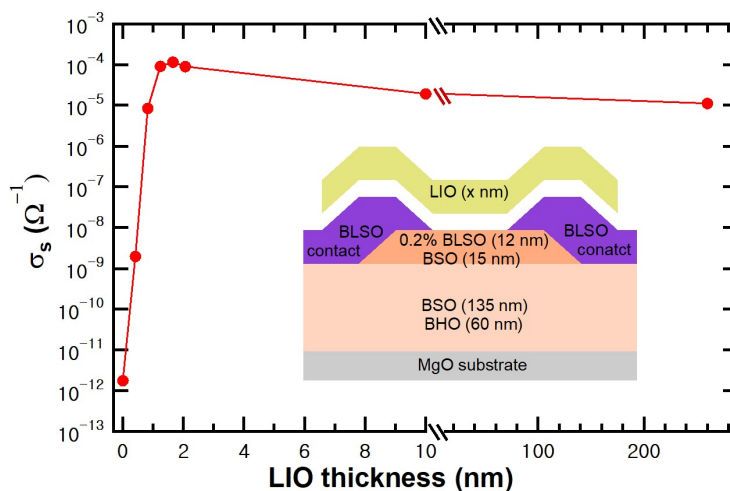


Figure 3.6 LIO thickness dependence of the LIO/BLSO interface conductance.

3.4. Field effect device based on $\text{LaInO}_3/\text{BaSnO}_3$ interface

I fabricated FETs using LIO/BSO (undoped) interface on MgO substrates. Fig 3.7(a) shows the cross-sectional schematics of the FET and Fig 3.7(b) shows top view of the FET by an optical microscope. First, a buffer layer of 60 nm thick BHO was deposited on the entire surface of an MgO substrate. Then, 162 nm BSO was grown with a line pattern of 110 μm width, and a contact layer was deposited with a 4 % BLSO at both ends of the BSO line with 125 μm channel length. A gate dielectric of 294 nm LIO was grown afterwards, and finally a line gate electrode with a width of 160 μm was deposited. Fig 3.7(c) shows

the output characteristic. I_{ds} vs. V_{ds} were measured while varying the gate voltage from 0 V to 24 V. It shows that the pinch-off occurs at large V_{ds} . Fig 3.7(d) shows the transfer characteristic when the gate voltage sweep is performed in the linear region with $V_{ds} = 1$ V. The device shows clear switching with little leakage through the gate oxide. The field effect mobility value was calculated from the output characteristics with its maximum mobility $61.3 \text{ cm}^2/\text{Vs}$. The I_{on}/I_{off} is 1.0×10^9 , higher than that on an STO substrate, probably due to the more insulating MgO substrates. The subthreshold swing is $0.206 \text{ V}/\text{dec}$ at $V_{gs} = -5 \text{ V}$, lower than that on an STO substrate in spite of the slightly larger threading dislocation density. The trapped charge density seems smaller on MgO in spite of the slightly larger TD density on MgO, consistent with the data in Fig 3.5(a).

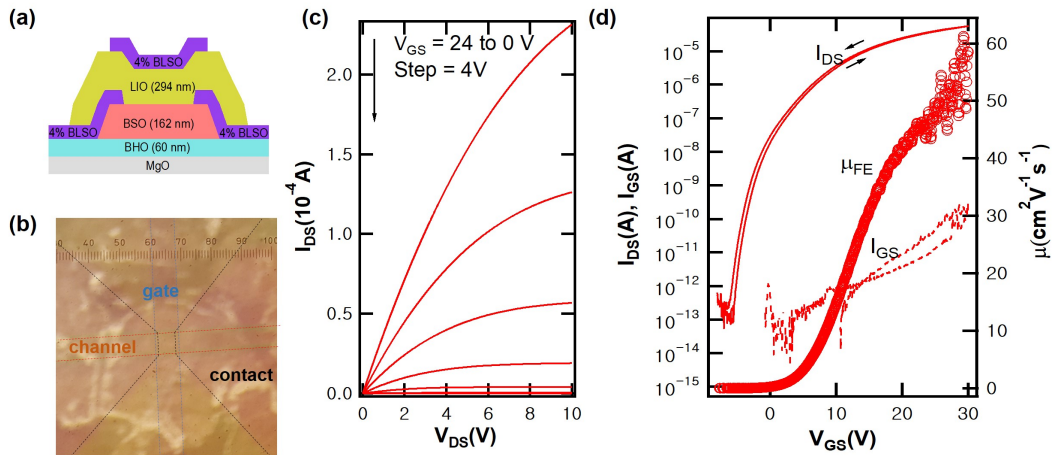


Figure 3.7 Structure and I-V characteristic of FET device based on unintentionally doped LIO/BSO interface on MgO substrate. (a) Cross-sectional structure of the device. (b) The top view of the device by an optical microscope. (c) The output characteristics of the device varying the gate voltage from 0 V to 24 V. (d) The transfer characteristics of the device in the linear region with $V_{DS} = 1$ V. The maximum mobility = $61.3 \text{ cm}^2/\text{Vs}$, $I_{on}/I_{off} = 1.0 \times 10^9$, and the subthreshold swing = $0.206 \text{ V}/\text{dec}$.

3.5. Temperature dependent electrical property

The temperature dependence of electrical property of LIO/BLSO interface was also measured with the same conditions of the measure of δ -doped BSO sample from 2K to room temperature. As I mentioned before, to see the quantum phenomena of 2DEG, high mobility value is needed at low temperature and high magnetic field. I tried to see the trend of electrical properties at the low temperature as the beginning of the study of quantum phenomena. Two kinds of LIO/BLSO sample were prepared. For the first sample, the LIO was grown on the molecular beam epitaxy (MBE)-grown BSO in Schlom group of Cornell University that is predicted to have lower defects than the PLD-grown BSO, and the other is the interface that is made in the same condition of previous samples using PLD. LIO/BLSO interface with MBE-grown BSO had much lower resistance than that of the interface with PLD-grown BSO. Although PLD-grown one has 0.3% La-doped channel, MBE-grown one has even lower resistance. It can be thought MBE-grown one has much smaller acceptor density like the interface on the MgO compared to the on the STO.

Temperature dependent property of LIO/BLSO interface was compared to the properties of δ -doped BSO sample with 2% La-doped channel because they have similar resistance and 3D carrier density distribution shown in Fig 3.8. δ -doped BSO with 2 nm of 2% La-doped channel has most similar 3D carrier distribution from the P-S calculation, though it has a little broader distribution than LIO/BLSO interface. More doped and thinner BLSO in δ -doped system will make much similar 3D carrier density distribution with LIO/BLSO interface, but under 1 nm channel is hard to control its thickness and the surface roughness will be a problem. Therefore, 2~3 nm of 2% La-doped BSO channel with δ -doped structure were used for comparison. When compared to the temperature dependent electrical characteristics of a δ -doped sample that has similar resistance to the LIO/BLSO interface,

LIO/BLSO interface shows a little higher resistance at low temperature, and rough trend is similar. The mobility value should be higher than $10,000 \text{ cm}^2/\text{Vs}$ at low temperature to see the quantum phenomena, but the interface does not show it. Even MBE-grown BSO with a relatively small acceptor density still seems to have a lot of dislocations, and to solve the problem, a substrate that matches lattice with BSO is required. If the problem is improved to have high mobility, this study in δ -doped BSO and LIO/BLSO interface will be helpful to understand 2D characteristics of BSO.

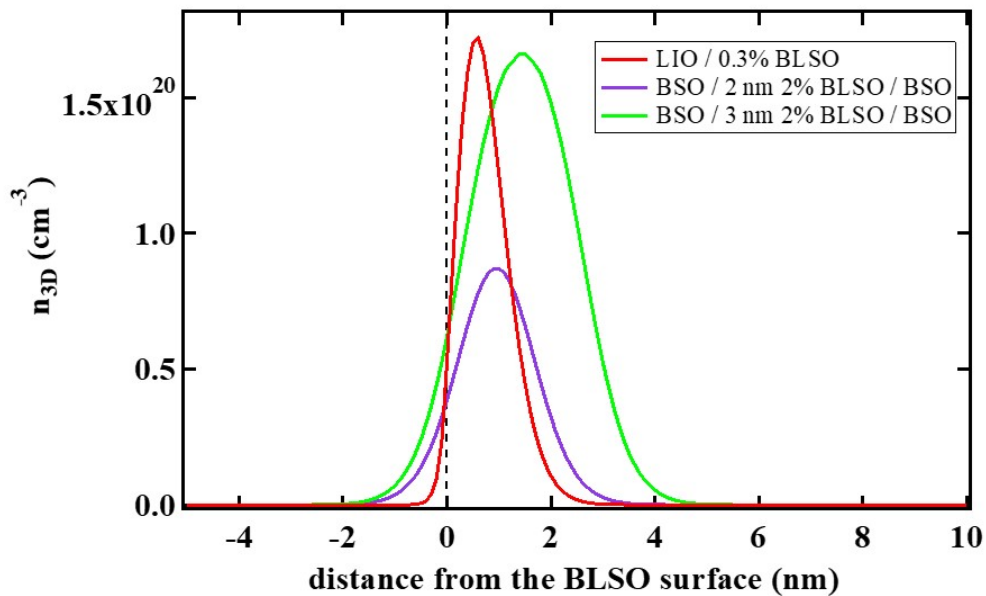


Figure 3.8 Calculated 3D carrier density of LIO/ 0.3% BLSO interface and δ -doped BSO with 2% doped 2 nm and 3 nm channel layer.

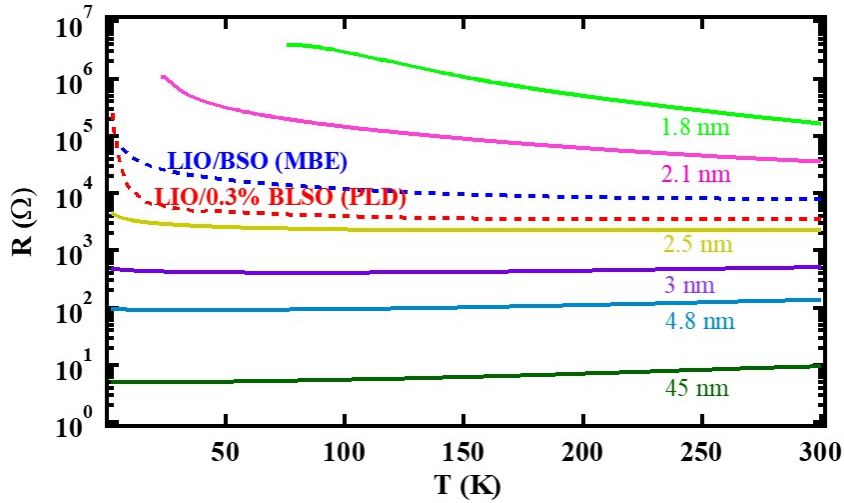


Figure 3.9 Temperature dependent resistance of the LIO/BLSO interface described with the result of δ -doped BSO.

3.6. Conclusion

In summary, I have shown that LIO/BLSO interfaces formed on non-perovskite MgO substrates show a 2DEG-like behavior in their electrical properties. Unlike on STO substrates, the interface with nominally undoped BSO showed a conductance increase, and we believe that it is due to the slightly higher Fermi level of BSO on MgO substrates, either from the larger donor density or from the smaller acceptor density. I also fabricated FETs using LIO/BSO (undoped). The on/off ratio and subthreshold swing value is better than other FETs based on BSO mainly due to its very low off state current level [21, 33, 35-38]. However, the mobility is lower than the FET with LIO/BLSO interface on STO substrates though our FET has no ionized impurity scattering from dopants on the channel [21], probably due to less crystalline quality on non-perovskite MgO substrates. I have also presented the temperature dependent property of LIO/BLSO interface. Further improvement on the crystalline quality of each layer and reduction of threading dislocations will lead to more understanding of the fundamental properties of the interface and practical devices using such interface.

References

- [1] J. A. Bert, B. Kalisky, C. Bell, M. Kim, Y. Hikita, H. Y. Hwang, and K. A. Moler, *Nat. Phys.* **7**, 767 (2011).
- [2] M. Huijben, G. Rijnders, D. H. A. Blank, S. Bals, S. van Aert, J. Verbeeck, G. van Tendeloo, A. Brinkman, and H. Hilgenkamp, *Nat. Mater.* **5**, 556 (2006).
- [3] N. Reyren, S. Thiel, D. Caviglia, L. F. Kourkoutis, G. Hammerl, C. Richter, C. W. Schneider, T. Kopp, A.-S. Ruetschi, D. Jaccard, M. Gabay, D. A. Muller, J.-M. Triscone, and J. Mannhart, *Science* **317**, 1196 (2007).
- [4] L. Li, C. Richter, J. Mannhart, and R. C. Ashoori, *Nat. Phys.* **7**, 762–766 (2011).
- [5] U. Kim, C. Park, Y. M. Kim, J. Shin, and K. Char, *APL Mater.* **4**, 071102 (2016).
- [6] M. J. Manfra, K. W. Baldwin, A. M. Sergent, K. W. West, R. J. Molnar, and J. Caissie, *Appl. Phys. Lett.* **85**, 5394 (2004).
- [7] A. Tsukazaki, S. Akasaka, K. Nakahara, Y. Ohno, H. Ohno, D. Maryenko, A. Ohtomo and M. Kawasaki, *Nature Mater.* **9**, 889 (2010).
- [8] A. Ohtomo and H. Y. Hwang, *Nature* **427**, 423 (2004).
- [9] J. P. Ibbetson, P. T. Fini, K. D. Ness, S. P. DenBaars, J. S. Speck, and U. K. Mishra, *Appl. Phys. Lett.* **77**, 250 (2000).
- [10] H. W. Jang, C. M. Jeon, K. H. Kim, J. K. Kim, S.-B Bae, J.-H. Lee, J. W. Choi, and J.-L. Lee, *Appl. Phys. Lett.* **81**, 1249 (2002).
- [11] N. Nakagawa, H. Y. Hwang, and D. A. Muller, *Nat. Mater.* **5**, 204 (2006).
- [12] W. Siemons, G. Koster, H. Yamamoto, W. A. Harrison, G. Lucovsky, T. H. Geballe, D. H. A. Blank, and M. R. Beasley, *Phys. Rev. Lett.* **98**, 196802 (2007).
- [13] H. J. Kim, U. Kim, H. M. Kim, T. H. Kim, H. S. Mun, B.-G. Jeon, K. T. Hong, W.-J. Lee, C. Ju, K. H. Kim, and K. Char, *Appl. Phys. Express* **5**, 061102 (2012).
- [14] H. J. Kim, U. Kim, T. H. Kim, J. Kim, H. M. Kim, B.-G. Jeon, W.-J. Lee, H. S. Mun, K. T. Hong, J. Yu, K. Char, and K. H. Kim, *Phys. Rev. B* **86**, 165205 (2012).
- [15] K. Krishnaswamy, L. Bjaalie, B. Himmetoglu, A. Janotti, L. Gordon, and C. G. Van de Walle, *Appl. Phys. Lett.* **108**, 083501 (2016).
- [16] J. Shin, Y. M. Kim, C. Park and K. Char, *Phys. Rev. A* **13**, 064066 (2020).
- [17] Y. M. Kim and K. Char, unpublished.
- [18] U. Kim, C. Park, T. Ha, R. Kim, H. S. Mun, H. M. Kim, H. J. Kim, T. H. Kim, N. Kim, J. Yu, K. H. Kim, J. H. Kim, and K. Char, *APL Mater.* **2**, 056107 (2014).

- [19] B. Hadjarab, A. Bouguelia, A. Benchettara, and M. Trari, *J. Alloy. Compd.*, **461**, 360 (2008).
- [20] P. Singh, B. J. Brandenburg, C. P. Sebastian, P. Singh, S. Singh, D. Kumar, and O. Parkash, *Jpn. J. Appl. Phys.* **47**, 3540 (2008).
- [21] U. Kim, C. Park, T. Ha, Y. M. Kim, N. Kim, C. Ju, J. Park, J. Yu, J. H. Kim, and K. Char, *APL Mater.* **3**, 036101 (2015).
- [22] H. M. Park, H. J. Lee, S. H. Park, and H. I. Yoo, *Acta Cryst. C* **59**, i131-i132 (2003).
- [23] A. V. Sanchela, T. Onozato, B. Feng, Y. Ikuhara, and H. Ohta, *Phys. Rev. Mater.* **1**, 034603 (2017).
- [24] L. L. Chang, H. Sakaki, C. A. Chang, and L. Esaki, *Phys. Rev. Lett.* **38**, 1489 (1977).
- [25] H. Cao, J. Tian, I. Miotkowski, T. Shen, J. Hu, S. Qiao, and Y. P. Chen, *Phys. Rev. Lett.* **108**, 216803 (2012).
- [26] G. Stöger, G. Brunthaler, G. Bauert, K. Ismail, B. S. Meyerson, J. Lutz, and F. Kuchar, *Semicond. Sci. Technol.* **9**, 765 (1994).
- [27] S. F. Nelson, K. Ismail, J. J. Nocera, F. F. Fang, E. E. Mendez, J. O. Chu, and B. S. Meyerson, *Appl. Phys. Lett.* **61**, 64 (1992).
- [28] F. B. Mancoff, L. J. Zielinski, and C. M. Marcus, *Phys. Rev. B* **53**, R7599(R) (1996).
- [29] J. A. Simmons, H. P. Wei, L. W. Engel, D. C. Tsui, and M. Shayegan, *Phys. Rev. Lett.* **63**, 1731 (1989).
- [30] D. M. Roessler and W. C. Walker, *Phys. Rev.* **159**, 733 (1967).
- [31] J. Nowotny, *Science of Ceramic interface II* (Elsevier Science Publisher B. V., Amsterdam, The Netherlands, 1994) p. 349.
- [32] S. Piskunov, E. Heifets, R. I. Eglitis, G. Borstel, *Comp. Mater. Sci.*, **29**, 165 (2004).
- [33] Juyeon Shin, Young Mo Kim, Youjung Kim, Chulkwon Park, and Kookrin Char, *Appl. Phys. Lett.* **109**, 262102 (2016).
- [34] G. Lupina, O. Seifarth, P. Dudek, G. Kozlowski, J. Dabrowski, H.-J. Thieme, G. Lippert, T. Schroeder, and H.-J. Müssig, *Phys. Status Solidi B* **248**, 323 (2011).
- [35] U. Kim, Ph. D. thesis, Seoul National University (2015).
- [36] C. Park, U. Kim, C. J. Ju, J. S. Park, Y. M. Kim, and K. Char, *Appl. Phys. Lett.* **105**, 203503 (2014).
- [37] Y. M. Kim, C. Park, T. Ha, U. Kim, N. Kim, J. Shin, Y. Kim, J. Yu, J. H. Kim, and K. Char, *APL Mater.* **5**, 016104 (2017).
- [38] Y. M. Kim, C. Park, U. Kim, C. Ju, and K. Char, *Appl. Phys. Express* **9**, 011201 (2016).

Chapter 4. Analysis of $\text{LaInO}_3/\text{BaSnO}_3$ interface by Poisson-Schrödinger equation

In this chapter, I will discuss the quantitative analysis of the LIO/BLSO interface shown in chapter 3. 2DEG systems have high carrier density and mobility in the quantum well and their mechanisms have been understood by simulations with 1D P-S equation. In this chapter, I will analyze an oxide 2DEG system composed of LIO and BSO using P-S simulation, which exhibits even higher carrier density than conventional 2DEGs. The “interface polarization” model that the polarization exists only near the interface has explained the electrical property of LIO/BLSO 2DEG. Through this model, I investigated how quantum well with high carrier density is formed discussing the role of 13 kinds of LIO and BSO material parameters; polarization, concentration and activation energy of donor, deep donor, acceptor, and deep acceptor, effective mass, dielectric constant, band gap, and conduction band offset between two materials. The calculation results show that the material parameters of LIO and BSO have adequate values for forming narrow and deep quantum well.

4.1. Introduction

Two-dimensional electron gas (2DEG) systems have been studied in several materials due to their applicability to devices such as high electron mobility transistor (HEMT) [1] and novel physical properties such as quantum phenomena [2]. There are well-known 2DEG heterostructures such as AlGaAs/GaAs, AlGaN/GaN, and MgZnO/ZnO with high two-dimensional carrier density (n_{2D}) and high mobility in the triangular quantum wells of the interface [3,4,5]. In recent years, perovskite oxide heterostructures have exhibited even higher n_{2D} while conventional 2DEGs have less than $1 \times 10^{13} \text{ cm}^{-2}$ at the AlGaN/GaN [3,6] and MgZnO/ZnO [4,7] interfaces, and $1 \times 10^{11} \text{ cm}^{-2}$ at the AlGaAs/GaAs interface [5,8]. For example, LaAlO_3 (LAO)/ SrTiO_3 (STO) oxide interface with perovskite structure showed n_{2D} of $1 \times 10^{13} \sim 1 \times 10^{14} \text{ cm}^{-2}$ [9,10] and the n_{2D} of LaInO_3 (LIO)/ BaSnO_3 (BSO)

2DEG was about $1 \times 10^{13} \sim 3 \times 10^{13} \text{ cm}^{-2}$ [11,12], even though there was a large dislocation density in the BSO channel due to lattice mismatch with substrates. High n_{2D} is an important factor in creating high drain current and transconductance in HEMT and such high concentration of carriers at the perovskite oxide interfaces can be completely modulated when combined with high dielectric material of the same perovskite structure [13].

There are still no exact theories explaining how these 2DEGs are formed. However, band bending created by conduction band offset at AlGaAs/GaAs (“modulation doping”) [14] and the discontinuity of spontaneous and/or piezoelectric polarization at AlGaN/GaN and MgZnO/ZnO (“polarization doping”) [3,4] generally explain the formation of 2D quantum wells and the thickness dependent electrical properties [15-19]. A “polar catastrophe” model with a specific termination layer has been proposed as a plausible hypothesis for the LAO/STO interface [20] although there are many contradicting opinions such as cation diffusion and oxygen vacancies [21]. In the LIO/(Ba,La)SnO₃ (BLSO) interface, these claims were ruled out by a series of experiments [11] with the help of high oxygen stability [22]. The “interface polarization” model that the polarization exists only near the interface, gradually decreasing over 4 unit cell of LIO from interface, was proposed to describe the formation of quantum well and the LIO thickness dependent electrical property, namely n_{2D} , that has different characteristic from the conventional 2DEGs [23]. It is reliable model in that it has something in common with conventional 2DEGs in terms of inversion symmetry. At the structures of the materials that consist conventional 2DEGs, it is known that the absence of inversion symmetry creates constant spontaneous and piezoelectric polarizations over long length scale with the help of lattice strain [24]. Similarly, it is believed that the inversion symmetry breaking that appears only near the LIO/BLSO interface creates “interface polarization” due to structural mismatch between the orthorhombic and cubic [25].

The 2DEG systems have been extensively analyzed through calculations using the 1D Poisson-Schrödinger (P-S) equation to prove these theoretical models work physically correct to make a quantum well and investigate how the parameters affect to the quantum well and n_{2D} . The P-S equation is a widely used tool to predict the band bending of systems such as nanowires, diodes, transistors and 2DEGs [26-29] calculating the potential energy from changes in charge distribution. The calculation results of the three conventional 2DEGs considering conduction band offset and polarization discontinuity as the cause of 2DEG at the interface agree well with the experimental results showing quantum well with n_{2D} of $1 \times 10^{11} \text{ cm}^{-2}$ in GaAs interface [30] and about $1 \times 10^{13} \text{ cm}^{-2}$ n_{2D} in GaN [31] and ZnO [32] interface. It also provided insight into how material parameters work. In modulation doped AlGaAs/GaAs 2DEG system, the effects of boundary conditions and the deep donors on quantum well were investigated [33,34]. The polarization doped AlGaN/GaN 2DEG was correlated with the Al fraction, the background donor concentration, and surface boundary conditions, while the surface boundary conditions were found to be the most crucial parameter [31]. The n_{2D} of MgZnO/ZnO 2DEG was found dependent on the Mg composition, the barrier layer thickness, and surface state density [32,35,36].

There are also several papers on simulation of perovskite oxide interfaces. The LAO/STO interface was investigated to explain the n_{2D} of quantum well [37,38]. LIO/BLSO 2DEG was calculated by P-S simulation [39] and interpreted to fit the experimental results [23]. However, more analysis of these perovskite oxide interfaces are needed, especially for how material parameters are involved in quantum well. In this chapter, I interpret the LIO/BLSO interface which is a little different with conventional 2DEGs. Using P-S simulation, I analyze if the properties of perovskite oxide heterostructure 2DEG can be well explained and investigate the role of material parameters of LIO and BSO, comparing conventional 2DEGs. First, I define 2 unknown material

parameters; polarization and deep donor density of LIO. Second, I investigate the effects of other LIO, BSO material parameters; concentration and activation energy of shallow and deep carriers, effective mass, dielectric constant, and conduction band offset between two materials. This analysis reveals what are the differences between conventional 2DEGs and LIO/BLSO 2DEG and I will look into the future direction of development of 2DEG.

4.2. Poisson-Schrödinger simulations of conventional two-dimensional electron gases

Prior to the LIO/BLSO analysis, I simulated three kinds of conventional 2DEGs to ensure that the experimental results could be reproduced with the calculation method (P-S band calculator designed by snider [29]) to be used in the LIO/BLSO interface using their formation mechanisms. $\text{Al}_{0.32}\text{Ga}_{0.68}\text{As}/\text{GaAs}$, $\text{Al}_{0.32}\text{Ga}_{0.68}\text{N}/\text{GaN}$, and $\text{Mg}_{0.32}\text{Zn}_{0.68}\text{O}/\text{ZnO}$ were simulated with the materials parameters that are important factors in calculation using P-S equation. Effective mass, dielectric constant, band gap, conduction band offset and polarization of GaAs [40,41], $\text{Al}_{0.32}\text{Ga}_{0.68}\text{As}$ [40,41], GaN [3,41,42], $\text{Al}_{0.32}\text{Ga}_{0.68}\text{N}$ [3,42-45], ZnO [41,46-48] and $\text{Mg}_{0.32}\text{Zn}_{0.68}\text{O}$ [46-50] are already known through experiments or calculations at 300 K temperature indicated in the Table 4.1. The concentrations and activation energy of donor and acceptor are also obtained through experiments or calculations [51-59]. However, since the parameters related to the donor and acceptors are known as ranges of values and are not critical parameters for calculation results, I entered any values in the ranges.

For the boundary condition the “Schottky” boundary condition was put on the surface because the surface of alloyed materials have a Fermi level pinning determined by the surface deep states [52,60,61] and the “slope=0” boundary condition that the band slope

goes to zero was placed on the bottom boundary of the non-alloyed substrate. Even if there is a Fermi level pinning at the bottom of the substrate, it is not considered here for simplicity, and it is not a problem for quantum well as the thick substrate thickness cancels out the effect of the bottom boundary. Using 9 kinds of materials parameters excluding shallow carriers that I did not consider here and boundary conditions, I calculated the band bending at the GaAs, GaN, and ZnO interfaces with 30 nm alloyed film over the 500 nm of non-alloyed substrate with 32% of alloyed percentages. Although I used material parameters at a temperature of 300 K, but calculations were done at 4K to clearly see the energy eigenstates.

	GaAs	Al _{0.32} Ga _{0.68} As	GaN	Al _{0.32} Ga _{0.68} N	ZnO	Mg _{0.32} Zn _{0.68} O
m_e^*/m_0	0.067	0.096	0.27	0.37	0.30	0.49
κ	13.1	11.1	10.4	9.54	8.10	8.68
E_g (eV)	1.42	1.82	3.44	4.19	3.35	4.10
ΔE_c (eV)	-	0.35	-	1.1	-	0.59
P_{SP} ($\mu C \cdot cm^{-2}$)	0	0	2.90	4.56	5.40	7.43
P_{PE} ($\mu C \cdot cm^{-2}$)	0	$<1 \times 10^{-3}$	0	1.17	0	1.10

Table 4.1 Materials parameters used for GaAs, AlGaAs, GaN, AlGaN, ZnO and MgZnO

4.2.1. GaAs two-dimensional electron gas

First, the GaAs interface, which is the simplest 2DEG, was simulated with the structure shown in Fig 4.1(a). The boundary conditions, concentrations of acceptor and donor with activation energies, and polarization values and directions are also described in Fig 4.1(a). The Si dopant in AlGaAs was considered a deep donor of 0.05 eV activation energy. The unknown values of AlGaAs, concentration and activation energy of deep acceptor, were set to the same values as GaAs. AlGaAs and GaAs have a zinc blende structure, which is one of the hexagonal structures. This structure has an inversion symmetry breaking that can

make spontaneous polarization at the bulk of AlGaAs and GaAs, and the strain gradient at the interface can make piezoelectric polarization in AlGaAs. However, the spontaneous polarization of AlGaAs and GaAs is known to be zero, and the piezoelectric polarization of AlGaAs is known to be negligible enough as shown in Table 4.1. Therefore, the Formation of GaAs 2DEG has been explained by a “modulation doping” model in which the 2DEG interface is created by conduction band offset [14].

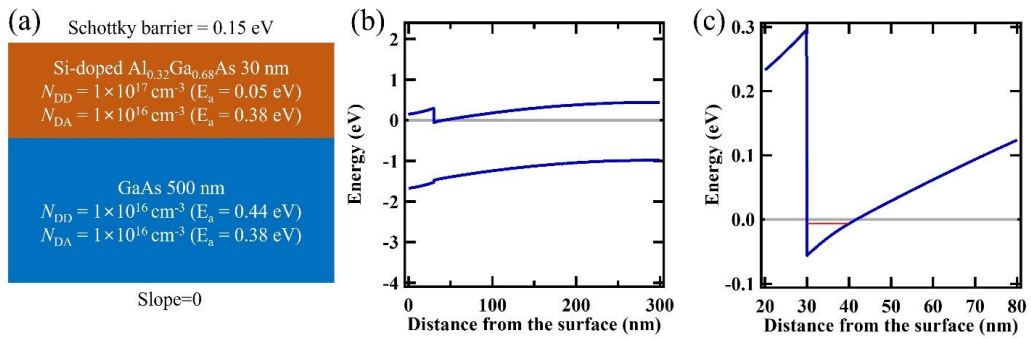


Fig 4.1 P-S simulation of AlGaAs/GaAs 2DEG. (a) Structure and parameters for calculation. (b) Calculation result of conduction band minimum energy for the Fermi level of 0 eV. (c) An enlarged view of (b) near the interface of AlGaAs and GaAs with subband energy of the red line.

The minimum conduction band bending result of the simulation is plotted with blue lines in Fig 4.1(b) relative to the Fermi level located at 0 eV, and Fig 4.1(c) is the enlarged conduction band minimum of the interface with bounded energy eigenvalues indicated by a red line. Quantum well was well formed at the interface, and the result was consistent with the experimental results mentioned above. In Fig 4.1(b) and (c), it has quantum well of 11.6 nm width where the conduction band minimum locates below the Fermi level. And the interface has an n_{2D} of $1.68 \times 10^{11} \text{ cm}^{-2}$ in the quantum well, which is similar to about $1 \times 10^{11} \text{ cm}^{-2}$ of the GaAs interface, known in experiments [5,8]. And the bound state energy described in Fig 4.1(c) is -0.0060 eV for AlGaAs/GaAs. It can be seen that the simulation

is physically right satisfying the “Schottky” boundary condition of 0.15 eV at the surface in Fig 4.1(b) and “slope=0” boundary condition that change the conduction band slope to zero as the x-axis increases. As the “modulation doping” model says, the conduction band offset at the interface makes quantum well below the Fermi level decreasing of conduction band energy at the interface.

4.2.2. GaN two-dimensional electron gas

Second, I simulated GaN interface. The boundary conditions, acceptor density and donor density with the activation energies, polarization values and directions are described in Fig 4.2(a) along with the structure used for simulation. There is no intentional dopant and unknown values of AlGaIn, concentrations and activation energies of deep carriers, were set to the same values as GaN. GaN and AlGaIn have wurtzite structure classified as a hexagonal structure, and the inversion symmetry is broken creating spontaneous polarization shown in Table 4.1 and piezoelectric polarization that is made by the strain gradient in AlGaIn. Conduction band offset and polarization discontinuity at the interface are known to be the main causes of GaN 2DEG formation, which is referred to as “polarization doping” [3].

The band bending result of the simulation is plotted in Fig 4.2(b), and Fig 4.2(c) is magnified one near the conduction band minimum with the bounded energy eigenvalues of the red line. A deep quantum well exists at the interface, and this result is also consistent with the previously mentioned experimental results. In Fig 4.2(b) and (c), it has quantum well of 5.2 nm width with $1.51 \times 10^{13} \text{ cm}^{-2}$ of 2DEG n_{2D} which is similar to about $1 \times 10^{13} \text{ cm}^{-2}$ of the GaN interface, can be seen from the experiments [3,6]. The bound state energies described in Fig 4.2(c) is -0.1323 eV. It also satisfies the “Schottky” boundary condition of

1.1 eV at the surface in Fig 4.2(b) and “slope=0” boundary condition as it goes to the bottom of the structure. As the “polarization doping” model explains, the conduction band offset at the interface makes a quantum well below the Fermi level decreasing the conduction band, and the polarization of AlGa_N makes a deeper quantum well with the downward slope in AlGa_N. In contrast, the polarization value of GaN makes conduction band near the interface higher and disturbs the formation of deep quantum well, but the larger total polarization of AlGa_N than GaN ultimately amplifies the role of conduction band offset at the interface.

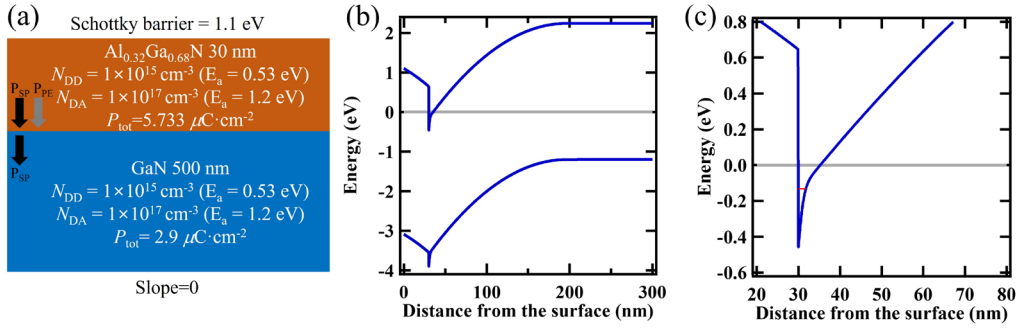


Fig 4.2 P-S simulation of AlGa_N/GaN 2DEG. (a) Structure and parameters including the direction of the polarizations for calculation. (b) Calculation result of conduction band minimum energy for the Fermi level of 0 eV. (c) An enlarged view of (b) near the interface of AlGa_N and GaN with subband energy of the red line.

Conduction band slope is mainly determined by polarization, dielectric constant, and carriers, and is also related to boundary conditions, conduction band offset, and 2DEG carrier density. In AlGa_N, the slope of the conduction band can be obtained by the charge neutrality condition that contains all of these parameters [62]. This slope becomes saturated with increasing thickness of AlGa_N, explaining the 2DEG that become saturated experimentally with increasing AlGa_N thickness [17,18]. The slope of GaN must also consider all parameters, but it can be simply understood as deep carrier activation and

polarization. They affect each other, changing the band bending. For example, in Fig 4.1(c), GaN has a changing band slope of a quadratic function with a large slope near the interface and a decreasing slope as x-axis increases. This is thought to be made by changing the activation rate of deep carriers. The polarization discontinuity near the interface decreases the conduction band making quantum well below the Fermi level and prevents the activation of deep donor in GaN filling electrons of deep donor level, whereas the deep acceptors are all activated because the energy level is located far below the Fermi level. This makes a high density of deep acceptors and a high band slope near interface of GaN. And as the x-axis increases in GaN, the conduction band rises upward under the influence of activated deep acceptors, and the deep donors start to activate because its energy level start to be located above the Fermi level, which changes the slope to zero. While this is happening, the polarization of GaN is invisible because it cancels out with deep carriers. Once the slope of the band disappears, charge neutrality remains with the slope zero band until the end of the sample.

4.2.3. ZnO two-dimensional electron gas

Third, ZnO interface was simulated. The parameters for the calculation and the structure of the interface are described in Fig 4.3(a). There is no intentional dopant and the unknown values of MgZnO, concentrations and activation energies of deep carriers, were set to the same values as that of ZnO. MgZnO and ZnO also have the same wurtzite structure as GaN, with the broken inversion symmetry. Large spontaneous polarizations are formed at each material shown in Table 4.1 with the similar piezoelectric polarization value of MgZnO to that of AlGaN. However, the direction of piezoelectric polarization of MgZnO faces the surface in the opposite direction to the that of AlGaN. Here, alloyed MgZnO was placed

on top for the comparison with GaAs and GaN 2DEG interface, but MgZnO should be placed on the bottom for the large carrier density of 2DEG. In that case, the direction of the piezoelectric polarization in ZnO coincides with the direction of spontaneous polarization of ZnO and amplifies the effect of the polarization discontinuity at the interface. Same as GaN interface, conduction band offset and polarization discontinuity at the interface are known to be the main causes of ZnO 2DEG formation, which is referred to as “polarization doping” [4].

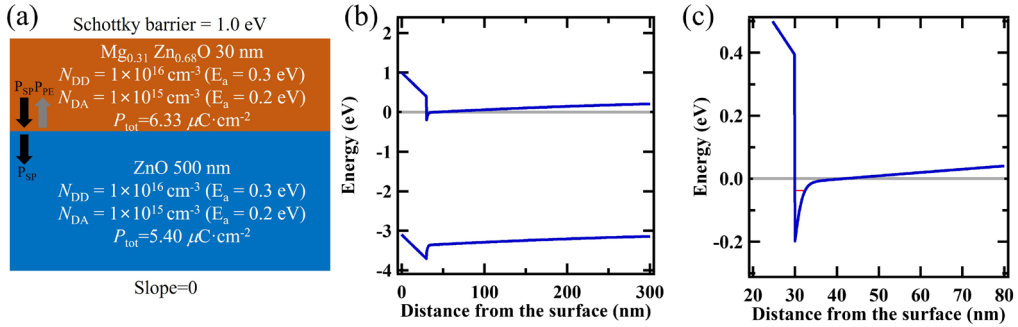


Fig 4.3 P-S simulation of MgZnO/ZnO 2DEG. (a) Structure and parameters including the direction of the polarizations for calculation. (b) Calculation result of conduction band minimum energy for the Fermi level of 0 eV (c) An enlarged view of (b) near the interface of MgZnO and ZnO with subband energy of the red line.

The band bending results obtained through simulation is plotted in Fig 4.3(b), and Fig 4.3 (c) is enlarged conduction band minimum of the interface with energy eigenvalues. In Fig 4.3(b) and (c), it has quantum well with a width of 11.4 nm, and the interface has an n_{2D} of $4.80 \times 10^{12} \text{ cm}^{-2}$ which is slightly smaller than the experiment results [4,7] of about $1 \times 10^{13} \text{ cm}^{-2}$ because of the swapped positions of MgZnO and ZnO. And the bound state energies described in Fig 4.3(c) is -0.0377 eV. It also satisfies boundary conditions well, though it seems to have band slope at the ZnO bottom because the bottom side of the graph

was cut off in the figure. Same as GaN interface, it is shown that the conduction band offset and the polarization discontinuity in the band bending together make quantum well.

4.2.4. Comparison of three conventional two-dimensional electron gases

These calculations reveal that the main parameters that make big differences between the three 2DEGs are conduction band offset or polarization or effective mass because these values show big difference. In AlGaIn/GaN, we can see deepest quantum well among Fig 4.1(b), 4.2(b), and 4.3(b) described in same scale, and the largest bounded energy level can be seen among Fig 4.1(c), 4.2(c), and 4.3(c). It is thought that this result is made by the largest conduction band offset and the largest polarization discontinuity in GaN interface that play crucial roles in creating a largest electric field making biggest conduction band change at the interface with 1.1 eV when it is only 0.35 eV at GaAs and 0.59 eV at ZnO interface and large downward band slope at AlGaIn. The polarization discontinuity between the two materials at the GaN interface is also biggest with $2.833 \mu\text{C}\cdot\text{cm}^{-2}$ while they are about $0 \mu\text{C}\cdot\text{cm}^{-2}$ at GaAs interface, and $0.93 \mu\text{C}\cdot\text{cm}^{-2}$ at ZnO interface. In contrast, in addition to the effect of small conduction band offset and polarization discontinuity, the small n_{2D} of the GaAs interface can be made by a much smaller effective mass of GaAs than GaN and ZnO. The density of state of a 2D quantum well is proportional to the absolute value of the bound state energy ($E_F - E$), and it is also proportional to the effective mass. It can be the reason that n_{2D} of GaAs interface is more than 10 times smaller than the ZnO interface n_{2D} , although the bound state energy level of the GaAs interface is only about 1/6 of that of ZnO interface.

The calculated values of n_{2D} can vary with change in the donor and acceptor carrier density, carrier activation energy, and boundary conditions that have big differences at each

material that make three 2DEGs, and the accuracy of the reference values are relatively low. However, they do not change quantum well very much because the most important parameters forming quantum well are conduction band offset and polarization value in 2DEGs. For example, when the deep acceptor activation energies of AlGaN and GaN in AlGaN/GaN are changed from 1.2 eV to 0.5 eV, n_{2D} changes from $1.51 \times 10^{13} \text{ cm}^{-2}$ to $1.49 \times 10^{13} \text{ cm}^{-2}$, and when the Schottky barrier on the AlGaN surface in AlGaN/GaN changes from 1.1 eV to 0.1 eV, the n_{2D} changes from $1.51 \times 10^{13} \text{ cm}^{-2}$ to $1.68 \times 10^{13} \text{ cm}^{-2}$ which are not significant differences. In the same sense, I do not need to worry the accuracy of these parameters because the existence of quantum well is correct, and the order of carrier density is reliable

4.3 Experimental results of LaInO₃/BaSnO₃ interface

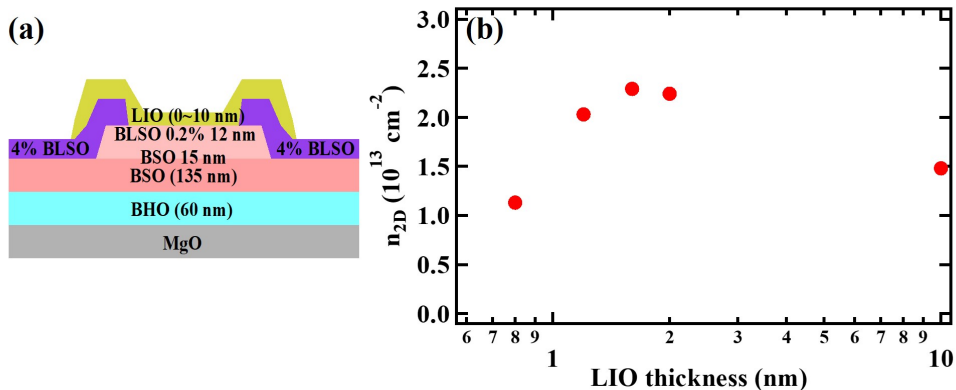


Figure 4.4 An experiment to measure the 2D carrier density (n_{2D}) of LIO/BLSO interface as the LIO thickness increases. (a) LIO/BLSO schematic structure with buffer and contact layers. (b) n_{2D} of interface at each LIO thickness.

I confirmed that P-S simulation works well for conventional 2DEGs. I will analyze the perovskite oxide LIO/BLSO interface based on the same calculation method. Before the calculation analysis, the electrical characteristics of the LIO/BLSO interface were

experimentally obtained with the structure of Fig 4.4(a) changing LIO thickness. All layers were deposited by the pulsed laser deposition technique. Targets were ablated for deposition with an energy fluence of approximately 1.5 J/cm^2 using a 248 nm wavelength KrF excimer laser at $750 \text{ }^\circ\text{C}$ in 0.1 Torr oxygen pressure. All targets were manufactured by Toshima Manufacturing Co. in Japan. Keithely 4200SCS parameter analyzer was used to record the electrical properties. MgO was chosen as the substrate for better property of the BLSO channel layer which have lower density of deep acceptor that traps electron [63] and for insulating property of substrate itself, made by a large band gap [12] compared to widely used STO substrate with relatively small band gap that can have conduction easily by oxygen vacancy though MgO has a different structure from BSO. The LIO/BLSO interface on the MgO substrate was deposited with the BaHfO₃ (BHO) and BSO buffer layers to reduce the dislocation density alleviating the lattice mismatch problem with the substrate [12]. For the channel layer, a 0.2% La-doped BSO layer with insulating property was used. Changing the thickness of the LIO layer on the 0.2% La-doped BSO channel layer, the Hall measurement of the interface between the LIO and BLSO was performed in Van der Pauw geometry through a contact layer of metallic 4% La-doped BSO in the 4 corners of the samples.

The LIO/BLSO interface shows conducting electrical property with maximum conductance of about $1 \times 10^{-4} \Omega$, although BLSO and LIO each have a conductance of less than $1 \times 10^{-11} \Omega^{-1}$. The n_{2D} of the interface at each LIO thickness are indicated by red points in Fig 4.4(b). The same trend as in previous report of the LIO/BLSO interface according to the LIO thickness is seen, which was well explained by the “interface polarization” model [12,23]. The n_{2D} increase as the LIO thickness increases from 1 unit cell to 4 unit cell, and after the peak value at 4 unit cell, they decrease and saturate. It is only represented below LIO thickness of 10 nm in Fig 4.4(b) due to the difficulty of Hall measurement in sample

of thick LIO, but the conductance saturated at thick LIO consistent with our previous results [12]. The sheet conductance decreased by only about 2.5 times, while LIO thickness was changed by 250 nm (from $1.5 \times 10^{-5} \Omega^{-1}$ at 10 nm LIO to $6.1 \times 10^{-6} \Omega^{-1}$ at 260 nm LIO), that is much less than the decrease of 7.5 times of conductance while LIO thickness changes 8.4 nm from 4 unit cell ($1.2 \times 10^{-4} \Omega^{-1}$) to 10 nm ($1.5 \times 10^{-5} \Omega^{-1}$). The LIO/BLSO interface has maximum conductance at LIO 4 unit cells, LIO 1.6 nm, which is about $1 \times 10^{-4} \Omega^{-1}$, where n_{2D} is $2.29 \times 10^{13} \text{ cm}^{-2}$ and the mobility is $31.2 \text{ cm}^2 \text{ V}^{-1} \text{ s}^{-1}$. The highest n_{2D} is larger than that of most conventional 2DEGs, although LIO/BLSO interface was grown on MgO substrate which has a different structure from BLSO channel and large lattice mismatch with the lattice constant of 4.212 Å of MgO [64] when it is 4.116 Å at BSO [22] and 4.117 Å at pseudocubic LIO [65]. This large lattice mismatch makes the electron mobility lower than in other 2DEG interfaces since the large density of dislocations limit the mobility.

4.4. Poisson-Schrödinger simulations and analysis of LaInO₃/BaSnO₃ interface

In previous report, theoretical calculation of LIO/BLSO interface using “interface polarization” model explained the trend of LIO thickness dependent electrical characteristic that has peak value of n_{2D} and mobility at 4 unit cell of LIO [23]. This characteristic cannot be explained using “constant polarization” known to exist in materials consisting conventional 2DEGs that shows monotonical change of n_{2D} and mobility with changing the thickness of the larger bandgap materials (AlGaAs, AlGaN, and MgZnO) [15-19] with much larger range of thickness length scale. Transmission electron microscopy (TEM) results of LIO/BLSO interface supports a “interface polarization” model [23] showing change in octahedral tilting over a range of about 4 unit cells of LIO near the

interface. And it is studied that the orthorhombic/cubic strain near LIO/BSO interface is related to the polarization that only exists near the interface [25]. At the SrRuO₃(SRO)/STO interface of the similar orthorhombic/cubic structure, symmetry breaking that makes polarization was also measured near the interface which is made by strain [66].

	BSO	LIO
P (μCcm^{-2})	0	0
N_D (cm^{-3})	1.43×10^{19} (for 0.1% La doping)	-
N_A (cm^{-3})	-	-
N_{DD} (cm^{-3})	-	$0 \sim 2 \times 10^{20}$
N_{DA} (cm^{-3})	4×10^{19}	-
E_D (eV)	-0.63	-
E_A (eV)	-	-
E_{DD} (eV)	-	2.5
E_{DA} (eV)	1.55	-
m_e[*]/m₀	0.42	0.46
κ	20	38
E_g (eV)	3.1	5.0
ΔE_C (eV)	-	1.6

Table 4.2 13 kinds of materials parameters used for BSO and LIO

Based on these grounds, I applied “interface polarization” model, and theoretical simulations were done at a temperature of 300 K using a P-S band calculator designed by snider [29]. A detailed description of calculation is given in supplementary of Ref. 23. The several material parameters and boundary conditions are key factors in calculation using the P-S equation. All the important material parameters used in the calculation are shown in the Table 4.2, in turn, they are polarization (P), donor and acceptor density (N_D, N_A), deep donor and deep acceptor density (N_{DD}, N_{DA}), donor and acceptor activation energy (E_D, E_A), deep donor and deep acceptor activation energy (E_{DD}, E_{DA}), effective mass

(m_e^*/m_0), dielectric constant (κ), band gap (E_g), and conduction band offset (ΔE_C), which are obtained from experiments [23, 65,67-71].

Among them, polarization near the interface and deep donor density of LIO are unknown parameters that I will define from the experimental results. And the activation energies of deep donor and deep acceptor are not accurate. Presently they were just put at the center of the band gap for simplicity. In the same sense, deep acceptors of LIO and deep donors of BSO are not considered as they are not activated when the deep state levels are at the center of band gap because the Fermi level is lower than the deep acceptor level of LIO and higher than the deep donor level of BSO when band bending is induced by the conduction band offset and polarization at the interface. If we use activation energy of deep carriers lower than values in Table 4.2, all kinds of deep states at LIO and BSO have to be considered. However, this case was not taken into account as it only requires adjustment of density of deep states while the big picture remains the same. In most of cases, the “Ohmic” boundary conditions were used at the LIO surface and BSO bottom except the deep carrier levels are changed in Fig 4.7 and 4.13. The “Ohmic” boundary condition sets charge neutrality condition that the Fermi level locates in the middle of the bandgap which exactly show deep carrier levels of LIO and BSO at the center of band gap. Many of calculations were done at the interface between 0.2% La-doped BLSO and LIO, but some were used undoped BSO channel due to hard calculation with too large carrier density in Fig 4.6, 4.7, 4.11, and 4.13 which have low BSO deep acceptor density or large LIO deep donor density.

4.4.1. Polarization and deep donor density of LaInO_3

Now, I will focus on what makes conducting 2D quantum well at the LIO/BLSO interface with high n_{2D} and how the material parameters of LIO and BSO change quantum well, based on experimental results. First, I set two completely unknown parameters, polarization and deep donor density of the LIO, while checking whether experimentally obtained n_{2D} occurs at the interface. For a rough guess on polarization and deep donor density, I first tried the similar values as adopted for the already interpreted LIO/BLSO interface grown on the STO substrate [23] and found polarization value that explains experimental results of Fig 4.4 adjusting the value. The interface polarization is described in Fig 4.5(a), that decreases from $60 \mu\text{C}\cdot\text{cm}^{-2}$ to $25 \mu\text{C}\cdot\text{cm}^{-2}$, $10 \mu\text{C}\cdot\text{cm}^{-2}$ and $0 \mu\text{C}\cdot\text{cm}^{-2}$ as it moves from the interface to the LIO surface, shown in minus values of x-axis. The calculation result of n_{2D} according to the change in LIO thickness on 0.2% BLSO with this polarization value is indicated by green line in Fig 4.5(b) and it fits well to the experimental results. The use of different substrate and slightly different deposition conditions seem to produce different polarization value with previous report. The deep donor density of LIO is $1.3 \times 10^{20} \text{ cm}^{-3}$ here. This interface polarization distribution well explains unique thickness dependent n_{2D} distribution in LIO/BLSO that has maximum point at 4 unit cell of LIO. Inversion symmetric orthorhombic LIO cannot explain the creation of the polarization of LIO. However, it can be thought that the strain and octahedral tilting near the interface can make broken inversion symmetry and polarization only near the interface of LIO as mentioned before. And I tried polarizations of 10% increase and decrease value. Red and purple lines in Fig 4.5(b) shows increased and decreased n_{2D} . From the n_{2D} results at each polarization, it is easy to understand that high polarization makes higher electric field, deeper quantum well, and higher n_{2D} at the interface. The dashed lines are the results

of using constant polarization. When the LIO has polarization of $60 \mu\text{C}\cdot\text{cm}^{-2}$, $30 \mu\text{C}\cdot\text{cm}^{-2}$ and $15 \mu\text{C}\cdot\text{cm}^{-2}$ at the whole film, it shows the same trend as the thickness dependence of GaN and ZnO 2DEG [17-19], which cannot explain the LIO/BLSO interface at all.

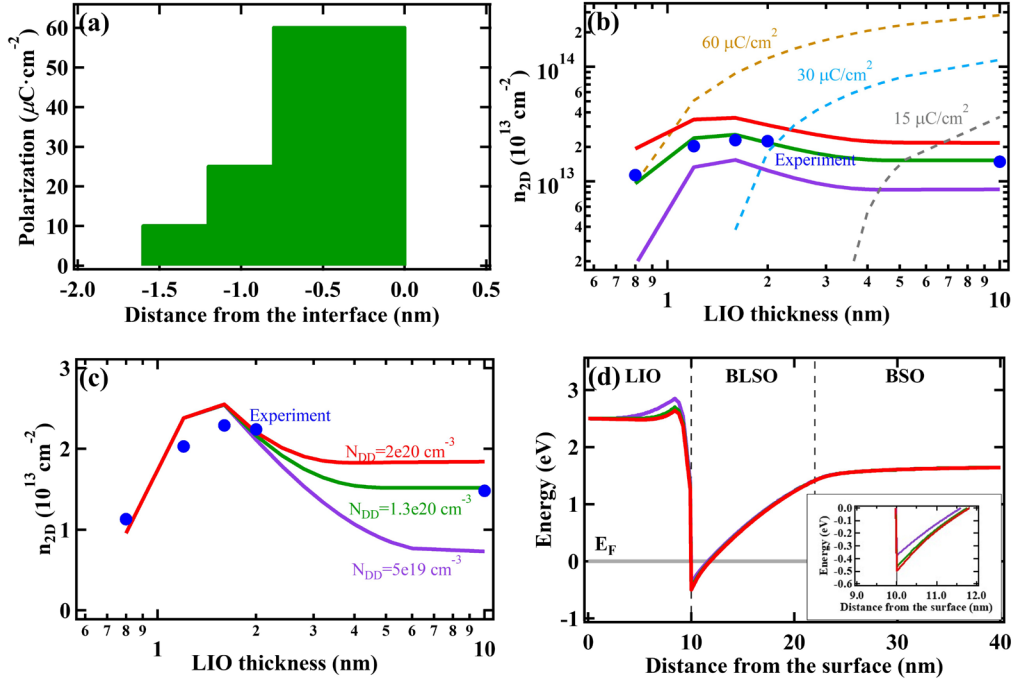


Fig 4.5 Results of P-S calculations and comparative experiments to define the unknown polarization value and deep donor density of LIO on the LIO/BLSO interface. (a) Interface polarization values on the LIO side that explains the experimental results well. (b) Carrier densities of quantum well calculated using the interface polarization in (a) were drawn by the green solid line that explains the experimental result of the blue dots. Increased and decreased carrier densities of red and purple solid lines from green solid line are calculated using the polarization values that are increased and decreased 10% from (a). Carrier densities using constant polarization that has same polarization value in the whole LIO film is shown in dashed lines, which cannot explain experimental data. (c) Carrier densities of quantum well with LIO deep donor densities of $5 \times 10^{19} \text{ cm}^{-3}$, $1.3 \times 10^{20} \text{ cm}^{-3}$, and $2 \times 10^{20} \text{ cm}^{-3}$ using the polarization of (a) according to the LIO thickness were drawn with solid lines and the blue dots show experimental results. (d) Changes in minimum conduction band bending at each deep donor density of LIO at LIO 10nm. Enlarged quantum well is shown in the inset.

Using an interface polarization value of 60/60/25/10 $\mu\text{C}\cdot\text{cm}^{-2}$ that explains experimental results, I set up another completely unknown parameter, deep donor density of the LIO. Fig

4.5(c) presents the n_{2D} of the interface according to the LIO thickness change in 3 kinds of deep donor density of LIO, $5 \times 10^{19} \text{ cm}^{-3}$, $1.3 \times 10^{20} \text{ cm}^{-3}$ and $2 \times 10^{20} \text{ cm}^{-3}$ of purple, green, and red lines, comparing the experimental results of blue dots. The experimental result of n_{2D} at LIO 10 nm fits well to the calculation result of $1.3 \times 10^{20} \text{ cm}^{-3}$ of LIO deep donor density while experiments on STO substrate has $2 \times 10^{20} \text{ cm}^{-3}$ of LIO deep donor density. This is consistent with deep acceptor density of BSO which have $6 \times 10^{19} \text{ cm}^{-3}$ on STO substrate and $4 \times 10^{19} \text{ cm}^{-3}$ on MgO substrate [63]. It would have been nice to have more data between 2 nm and 10 nm, but we knew the trend of that part in the previous papers [12, 23], so I proceeded as it is. The difference in LIO deep donor density only affects interface with thick LIO, after polarization ends at the LIO. This is because of the role of the LIO deep donor and it can be seen in conduction band bending [23]. The conduction band minimums are presented in Fig 4.5(d) at each LIO deep donor concentrations with LIO 10 nm. The interface polarization of LIO directs from LIO to BSO in the range of 4 unit cell of LIO (8.4 nm to 10 nm of x-axis in Fig 4.5(d)) making the energy of LIO side (8.4 nm of x-axis) higher and BSO side (10nm of x-axis) lower. And it helps activation of deep donors near the LIO side of polarization. Deep donors are ionized into positive ions after activation and positive ions screen increased energy made by polarization at the LIO side. In thin LIO, the energy of the LIO surface is mainly determined by the electric field of the interface with little effect of the deep donors, and after the end of polarization, the role of deep donor increases.

The difference of band bending at each deep acceptor concentration accurately show the role of LIO deep donor in Fig 4.5(d). As shown in the inset of Fig 4.5(d), low deep donor density makes less screening resulting in a high conduction band energy, shallow depth of the quantum well, and low n_{2D} , especially at thick LIO. In contrast, higher deep donor density makes more screening, resulting in lower conduction band, deeper quantum well

and higher n_{2D} , same with previously described in Ref. 23. The band slope can be easily understood again through a simple approximation of the Poisson equation in (1) where the $\varphi(x)$ is potential energy per unit charge, $\rho(x)$ is charge made by carriers, and ε is dielectric constant.

$$\nabla^2 \varphi(x) = -\frac{\rho(x)}{\varepsilon} \quad (1)$$

On the LIO side, there is only deep donor as a carrier. And I got the solution of potential energy as equation (2) with the constants of C_0 and C_1 and electron charge of e .

$$V(x) = e\varphi(x) = \frac{eN_{DD}}{\varepsilon}x^2 + C_0x + C_1 \quad (2)$$

Conduction band slope is determined by deep donor density with large value at large deep donor density. In Fig 4.5(d), when I compare the band slope before flattening of band; the slope from 6 nm to 8.4 nm at $5 \times 10^{19} \text{ cm}^{-3}$ of deep donor density and from 7.5 nm to 8.4 nm at $2 \times 10^{20} \text{ cm}^{-3}$ of deep donor density, the slope is large at large deep donor density. The range I consider depends on deep donor density because after flattening of the slope, the deep donor cannot be activated because the Fermi level has been lowered.

4.4.2. Deep acceptor and shallow donor density of BaSnO₃

I guessed two unknown parameters and at the same time confirmed that an “interface polarization” model is plausible explaining the electrical property of the interface as a function of LIO thickness. From now on, I am going to fix the polarization value of 60/60/20/10 $\mu\text{C}\cdot\text{cm}^{-2}$ in each unit cell of LIO at the interface and $1.3 \times 10^{20} \text{ cm}^{-3}$ of the LIO deep donor density. I will look at how already known other parameter values change quantum well at the LIO/BLSO interface. Let’s consider the donor and acceptor carrier density first. In LIO, carrier is only deep donor I have already investigated, and BSO has deep acceptor and donor (shallow only since no deep donors will be activated). Therefore,

the change of n_{2D} and band bending at different deep acceptor and donor density of BSO were investigated. The deep acceptor density of BSO is known to be about $4 \times 10^{19} \text{ cm}^{-3}$ on MgO substrate [23,63]. The n_{2D} as a function of LIO thickness with undoped BSO channel and the conduction band bending at 10 nm LIO with deep acceptor density of $4 \times 10^{19} \text{ cm}^{-3}$ of BSO are described in Fig 4.6(a), (b) by purple lines. And for the investigation of the role of deep acceptor density, the n_{2D} and the band bending are also shown at deep acceptor density of $1 \times 10^{17} \text{ cm}^{-3}$, $1 \times 10^{18} \text{ cm}^{-3}$, $1 \times 10^{19} \text{ cm}^{-3}$ and $6 \times 10^{19} \text{ cm}^{-3}$ by green, red, blue, and sky blue lines in same condition.

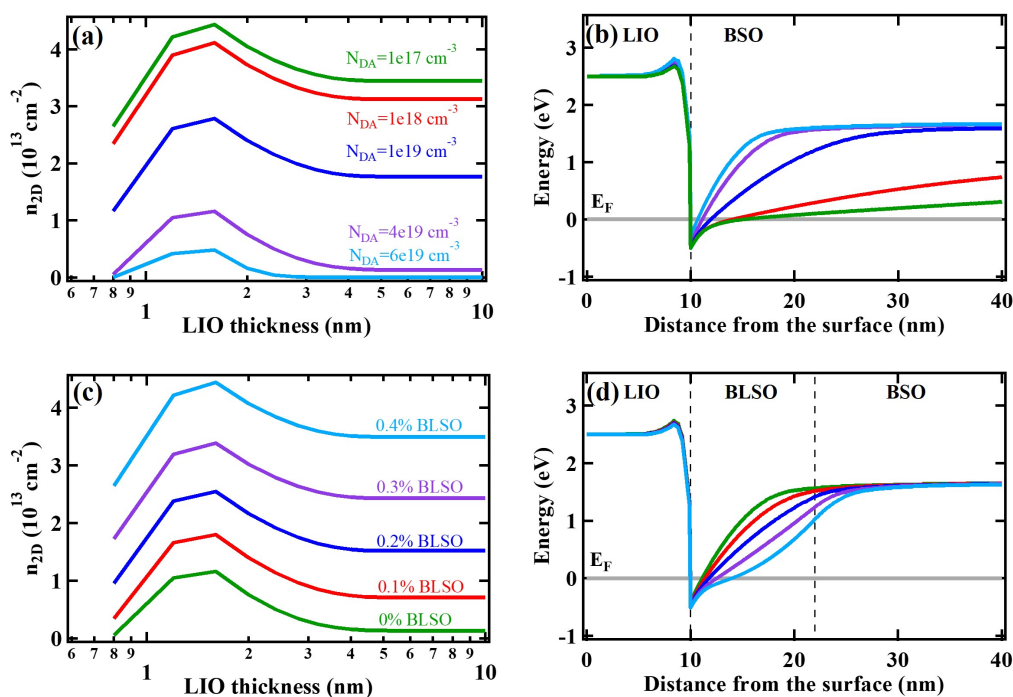


Fig 4.6 Influence of the deep acceptor density and shallow donor density of BSO on the LIO/undoped BSO and the LIO/BLSO interface calculated with the P-S equation. (a) Carrier densities of quantum well with deep acceptor density of $1 \times 10^{17} \text{ cm}^{-3}$, $1 \times 10^{18} \text{ cm}^{-3}$, $1 \times 10^{19} \text{ cm}^{-3}$, $4 \times 10^{19} \text{ cm}^{-3}$, and $6 \times 10^{19} \text{ cm}^{-3}$ according to the LIO thickness. (b) Changes in minimum conduction band bending at each deep acceptor density of BSO at LIO 10 nm. (c) Carrier densities of quantum well with shallow donor density from 0 to $5.72 \times 10^{19} \text{ cm}^{-3}$ (0.4% BLSO) according to the LIO thickness. (d) Changes in minimum conduction band bending at each shallow donor density of BSO at LIO 10 nm.

It is obvious that the n_{2D} of quantum well is high at low deep acceptor density, as the less activated acceptor increases the electron carrier density. The deep acceptor of BSO acts similar to deep donor of LIO according to equation (3).

$$V(x) = e\varphi(x) = -\frac{eN_{DA}}{\epsilon}x^2 + C_0x + C_1 \quad (3)$$

Deep acceptor is the only carrier of the BSO when the quantum well is made using undoped BSO channel. The quadratic coefficient is proportional to the deep acceptor density with a dielectric constant ϵ of the BSO in the channel layer, but the sign is opposite to the case of the LIO deep donor density. The absolute value of band slope should be larger at high deep acceptor density and it is shown in Fig 4.5(b) with the shallower and narrower quantum well. The deep acceptor of BSO works similarly to deep donor of LIO. If we reduce deep acceptor density with the use of lattice matched substrate, we will get much higher 2DEG carrier density.

The donor density of BSO can be controlled by the La dopant ratio of channel layer, and the doping dependent electrical properties of the LIO/BLSO interface have already been reported [12]. The formation of interface was calculated with 5 kinds of donor density from the undoped channel to the 0.4% La doped channel and they are illustrated in Fig 4.6(c) and (d). As can be easily thought of, high donor density of BSO channel makes high n_{2D} of interface in Fig 4.6(c), resulting in a deep and wide quantum well in Fig 4.6(d) calculated with 10 nm LIO layer. In the undoped BSO, the width of the quantum well is only 1.2 nm whereas in the 0.4% doped channel, it is 4.0 nm with 0.11 eV deeper well in Fig 4.6(d). And in the Poisson equation, the donor has an opposite effect to the slope of the energy band with positive quadratic coefficient compared to the effect of deep acceptor with opposite sign. This is why the slope near the interface is convex only in the band of 0.4% BLSO 2DEG in Fig 4.6(d), at which the shallow donor density starts to be greater than

deep acceptor density and concave towards substrate side. In low doped channels, shallow donor effect is canceled by deep acceptors and only concave slope is shown.

4.4.3. Deep carrier activation energy

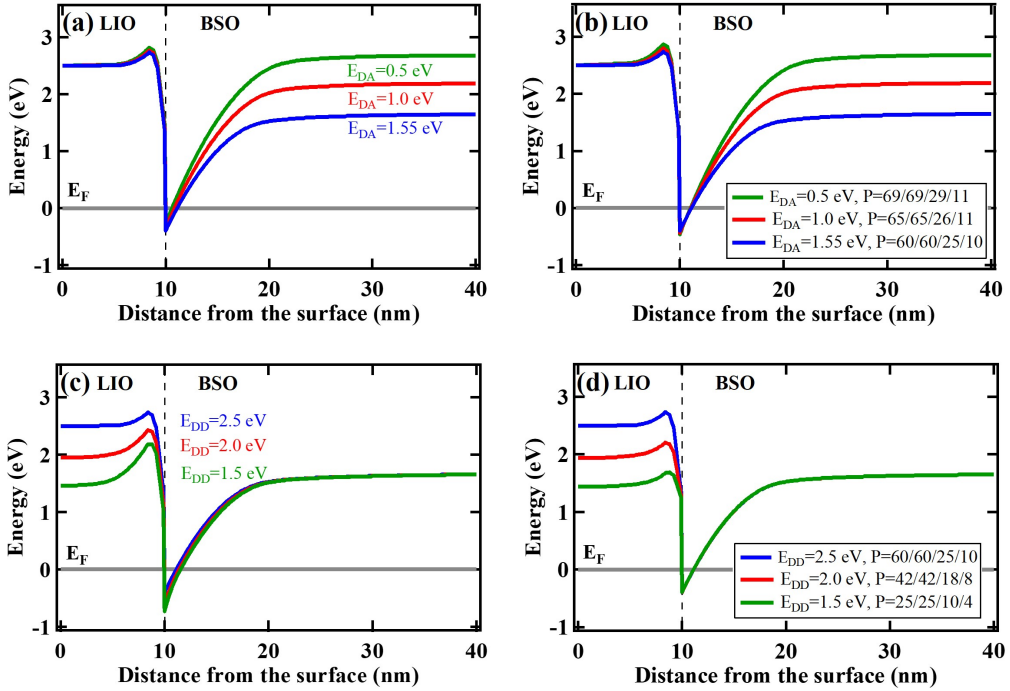


Fig 4.7 Influence of the deep acceptor activation energy of BSO and deep donor activation energy of LIO on the LIO/undoped BSO interface calculated with the P-S equation. (a) Changes in minimum conduction band bending at different deep acceptor activation energy of BSO, 0.5 eV, 1.0 eV, and 1.55 eV at LIO 10 nm. (b) Polarization adjustment to apply other deep acceptor activation energies of BSO. (c) Changes in minimum conduction band bending at different deep donor activation energy of LIO, 1.5 eV, 2.0 eV, and 2.5 eV at LIO 10 nm. (d) Polarization adjustment to apply other deep donor activation energies of LIO.

The deep state level has so far been considered to be at the center of the band gap, activation energy of 1.55 eV for BSO and 2.5 eV for LIO. However, they might be smaller in reality because most of deep state activation energy of point defects in perovskite oxide like LAO, STO, BSO are between 0.5 eV and half of band gap from the calculated expects

[72-74]. Therefore, it is meaningful to adjust the deep state activation energy of BSO and LIO though the big picture of quantum well does not change as mentioned earlier.

First, the deep acceptor activation energy of BSO was adjusted from 1.55 eV to 0.5 eV and 1.0 eV and investigated what happens in quantum well at the 10 nm of LIO/undoped BSO interface. Band bending at BSO deep acceptor activation energy of 0.5 eV, 1.0 eV and 1.55 eV are indicated by green, red, and blue lines in Fig 4.7(a). The conduction band bending slope of BSO increases at low deep acceptor activation energy. And the Fermi level goes down at the bottom boundary of the BSO because the low deep acceptor level lowers the Fermi level throughout the BSO layer based on the conduction band. These change the quantum well depth. The high band slope and the change in boundary condition of BSO both reduce n_{2D} at the quantum well with low deep acceptor activation energy of BSO. The n_{2D} of the 10 nm LIO/undoped BSO interface is 0 cm^{-2} at 0.5 eV and $4.87 \times 10^{10} \text{ cm}^{-2}$ at 1.0 eV of BSO deep acceptor activation energy. They have much less values of n_{2D} in the 10 nm LIO/undoped BSO interface than what should be $1.31 \times 10^{12} \text{ cm}^{-2}$, deduced from Fig 4.6 with undoped BSO channel using 1.55 eV deep acceptor activation energy and the polarization of 60/60/25/10 $\mu\text{C}\cdot\text{cm}^{-2}$. For n_{2D} of $1.31 \times 10^{12} \text{ cm}^{-2}$ which is the expected result of undoped BSO/LIO 2DEG from experiment, the polarization value adjustment is required at the interface when it has lower deep acceptor activation energy of BSO. The adjustment of the polarization value and band bending are shown in Fig 4.7(b) at the interface of 0.5 eV and 1.0 eV of deep acceptor activation energy. For the comparison, band bending of 1.55 eV of deep acceptor activation energy with unchanged polarization value of 60/60/25/10 $\mu\text{C}\cdot\text{cm}^{-2}$ was represented together. For higher n_{2D} , the polarization should increase to 69/69/29/11 $\mu\text{C}\cdot\text{cm}^{-2}$ at 0.5 eV at each unit cell of LIO and 65/65/26/11 $\mu\text{C}\cdot\text{cm}^{-2}$ at 1.0 eV. With these polarizations, n_{2D} is adjusted to $1.26 \times 10^{12} \text{ cm}^{-2}$ at 0.5 eV and $1.30 \times 10^{12} \text{ cm}^{-2}$ at 1.0 eV, similar to the value of $1.31 \times 10^{12} \text{ cm}^{-2}$ deduced with BSO deep

acceptor activation energy of 1.55 eV. If the deep acceptor activation energy is lower than the 1.55 eV, polarization value should be increased.

The adjustment of LIO deep donor activation energy is similar. The deep donor activation energy of LIO was adjusted from 2.5 eV, which is the half of LIO band gap, to 1.5 eV and 2.0 eV, and the changed quantum wells are described in Fig 4.7(c) with polarization of 60/60/25/10 $\mu\text{C}\cdot\text{cm}^{-2}$. The direction of change is opposite to the effect of the low deep acceptor activation energy of BSO. Band slope change made by LIO deep donor density barely affect the quantum well but more activated deep donors increase the electron carriers and make deeper quantum well increasing the Fermi level of LIO. Surface boundary of Fermi level based on the conduction band of LIO also increases at the low deep donor activation energy of LIO. This change results in $n_{2\text{D}}$ of $3.21 \times 10^{13} \text{ cm}^{-2}$ at 1.5 eV and $1.71 \times 10^{13} \text{ cm}^{-2}$ at 2.0 eV of deep donor activation energy of LIO. For the same $n_{2\text{D}}$ predicted from the experiment like I did in Fig 4.7(b), polarization of 25/25/10/4 $\mu\text{C}\cdot\text{cm}^{-2}$ at 1.5 eV and 42/42/18/8 $\mu\text{C}\cdot\text{cm}^{-2}$ at 2.0 eV were needed in Fig 4.7(d). Smaller polarization is required to compensate for the $n_{2\text{D}}$ increase caused by more activated deep donor. However, the effect on the quantum well of deep donor level of LIO is much larger than deep acceptor level of BSO. At the quantum well that is located under the Fermi level, all BSO deep acceptors are fully activated regardless of deep acceptor level because they are under Fermi level in all cases, and the level only affects the band far from the quantum well and makes little change in 2DEG $n_{2\text{D}}$ while LIO deep donor level directly affects to the quantum well changing deep donor activation rate at each activation energies. This is why low deep acceptor activation energy of BSO in Fig 4.7(b) requires a slightly large polarization while low deep donor activation energy of LIO in Fig 4.7(d) requires a much smaller polarization. The combination of the BSO deep acceptor activation energy of 1.0 eV and the LIO deep donor activation energy of 1.5 eV produces $n_{2\text{D}}$ $2.73 \times 10^{13} \text{ cm}^{-2}$ with

a polarization of 60/60/25/10 $\mu\text{C}\cdot\text{cm}^{-2}$. With the same process in this combination, we need a polarization of 30/30/11/5 $\mu\text{C}\cdot\text{cm}^{-2}$ to make $1.37 \times 10^{12} \text{ cm}^{-2}$ of n_{2D} , similar with experimentally deduced value of $1.31 \times 10^{12} \text{ cm}^{-2}$ at 1.55 eV and 2.5 eV of BSO deep acceptor and LIO deep donor activation energy. This polarization value is plausible though it is much larger than the polarization values of the materials forming the conventional 2DEGs in Table 4.1, because it is smaller than the spontaneous polarization of ferroelectric materials with 25~45 $\mu\text{C}\cdot\text{cm}^{-2}$ in BaTiO_3 , 40 $\mu\text{C}\cdot\text{cm}^{-2}$ in KNbO_3 and 50~100 $\mu\text{C}\cdot\text{cm}^{-2}$ PbTiO_3 [75]. This value is more reasonable than the 60/60/25/10 $\mu\text{C}\cdot\text{cm}^{-2}$.

However, the polarization value is not the only thing to change. Like polarization among 13 kinds of material parameters, deep donor density of LIO and deep acceptor density of BSO are also parameters deduced from the electrical properties of BLSO and 2DEG with a deep activation energy value of half of the band gap. Therefore, these values also need to be adjusted with the changing deep activation energy values. When thinking about BSO case, we need to lower deep acceptor density if its activation energy goes down, because the deep acceptor density of $4 \times 10^{19} \text{ cm}^{-3}$ was estimated from the experimental electrical properties of the BLSO films under the assumption of 1.55 eV of BSO deep acceptor activation energy. If the deep acceptor is better activated, the same result can be achieved at low deep acceptor density. For example, for the experimental electrical result of δ -doped BLSO film [76] with a 20 nm 1% doped BSO channel, deep acceptor density of $3 \times 10^{19} \text{ cm}^{-3}$ at BSO deep acceptor activation energy of 0.5 eV explain it well while deep acceptor density of $3.6 \times 10^{19} \text{ cm}^{-3}$ makes the same result at the BSO deep acceptor activation energy of 1.55 eV. The value of deep acceptor density set to $4 \times 10^{19} \text{ cm}^{-3}$ in this chapter should also be lowered when adjusting the deep state level, and finally after that, the polarization value also needs to be changed. The deep donor level of LIO has to be deal with same process. However, the change of deep state levels and deep state densities are little and only

give less than about 50% reduction of polarization though we consider all changes. Therefore, even if these fine-tuning is not considered, the results are not very wrong, and in the next calculations, I used deep state activation energy of half of band gap. In addition, when reducing the deep state energy, we should consider the presence of deep acceptor in LIO and deep donor in BSO as mentioned earlier that we just set them as 0 cm^{-3} because deep acceptor in LIO and deep donor in BSO are activated when their activation energy is less than the half of band gap. However, deep acceptor in LIO and deep donor in BSO is equivalent to changing the density of deep donor in LIO and density of deep acceptor in BSO. So, I do not do that here.

4.4.4. Effective mass, dielectric constant, and conduction band offset

Fig 4.8 shows what the effective masses of BSO and LIO play for the quantum well. For a rough analysis here, I checked the energy eigenvalue of the Schrödinger equation with the triangular quantum well when the minimum triangular quantum well energy is 0, because LIO/BLSO quantum well has a triangle-like shape. Equation (4) is the n th energy eigenvalue of triangular quantum well while e is the electron charge, A is the electric field that creates triangle form of quantum well, same with the slope of conduction band in LIO/BLSO case, \hbar is the Plank constant, m is the effective mass and a_n is the n th zero of the Airy function which have minus value.

$$E_n = - \left(\frac{e^2 A^2 \hbar^2}{2m} \right)^{1/3} a_n \quad (4)$$

Fig 4.8(a) and (b) show the n_{2D} of 2DEG according to LIO thickness and band bending with 10 nm LIO of 2DEG at $0.2 m_e$, $0.42 m_e$ and $7 m_e$ of BSO effective mass while the actual effective mass of BSO is $0.42 m_e$. The n_{2D} is much greater at the effective mass of $7 m_e$, indicated by the blue line, than the other things that have more than 10 times smaller

effective mass, although quantum well is shallow and narrow at high effective mass, contrary to the trend seen so far. This is made by the relationship between the density of state and the effective mass at each bounded energy. In the 2D state, the density of state is proportional to the effective mass while it is also proportional to the energy value that is inversely proportional to the 1/3 power of effective mass in equation (4). As a result, as the effective mass increases, the density of state increases which creates high n_{2D} even in shallow and narrow quantum well with high effective mass. But the n_{2D} difference is smaller than the value of effective mass to the 2/3 because the quantum well has little difference in A in the three cases.

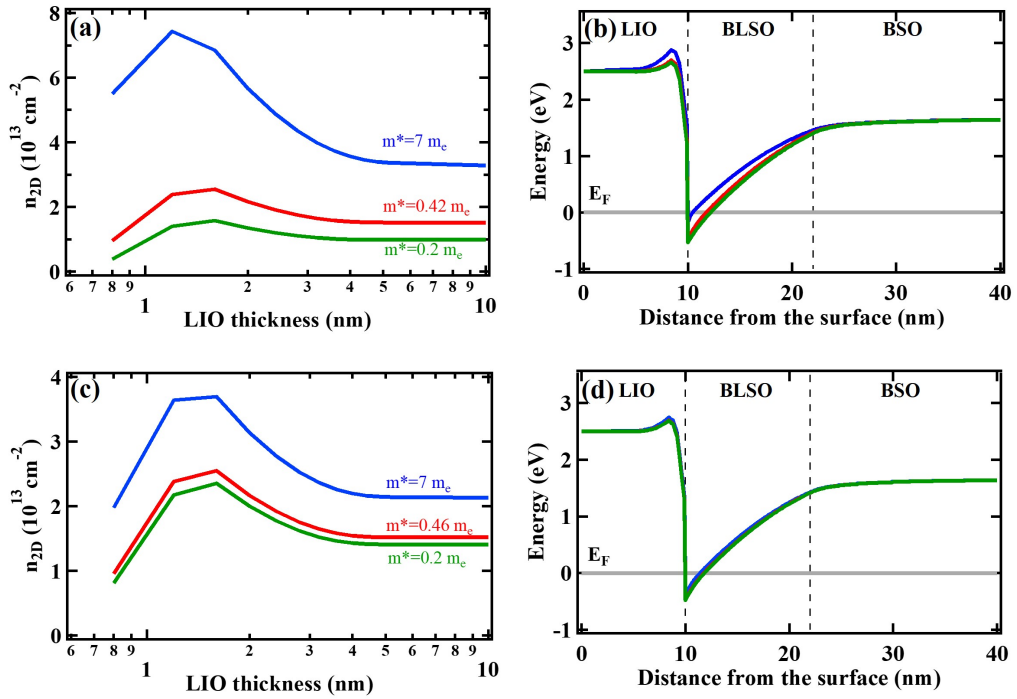


Fig 4.8 Influence of the effective mass of BSO and LIO on the LIO/BLSO interface calculated with the P-S equation. (a) Carrier densities of quantum well with BSO effective masses of $0.2 m_e$, $0.42 m_e$, and $7 m_e$ according to the LIO thickness. (b) Changes in minimum conduction band bending at each effective mass of BSO at LIO 10 nm. (c) Carrier densities of quantum well with LIO effective masses of $0.2 m_e$, $0.46 m_e$, and $7 m_e$ according to the LIO thickness. (d) Changes in minimum conduction band bending at each effective mass of LIO at LIO 10 nm.

Since the 2DEG quantum well is on the BSO side, it can be thought that the effective mass of LIO should not affect the n_{2D} of 2DEG. However, the effective mass of LIO also affects n_{2D} showing an increase at higher effective mass, and this is because the 2DEG quantum well is not located only on the BSO side. The electron carrier also spans a LIO of about 1 nm at the interface when it is calculated with $0.46 m_e$ of LIO effective mass in Fig 4.8(d) that has a 3D carrier density of $1.53 \times 10^{15} \text{ cm}^{-3}$ at the LIO of 1 nm apart from the interface. But the effect of LIO effective mass is much smaller because most of the 2DEG carriers are located in BSO. There is only a small change in the band shown in Fig 4.8(d), and the effect of the density of state is also small in Fig 4.8(c) compared to the effect of BSO effective mass. From these analysis, it can be thought that the effective mass of LIO and BSO are large enough compared to other materials that make up the other 2DEG interfaces, for making higher carriers of 2DEG.

The dielectric constant also plays an important role in forming 2DEG. In Fig 4.9(a), n_{2D} is plotted according to the LIO thickness at four different dielectric constants of BSO, 10, 20, 50 and 100, where 20 is an experimentally obtained value. When the dielectric constant goes up, n_{2D} goes down making the shallow quantum well in Fig 4.9(b) roughly. As can be seen from equation (2) and (3), the conduction band slope is inversely proportional to the dielectric constant while it is proportional to the carrier density, and the role of dielectric constants in BSO and LIO can be understood in the same way as for deep donor density and deep acceptor density. In contrast to the changes that deep donor density and deep acceptor density make, the absolute value of quadratic coefficient of band slope of BLSO decreases in Fig 4.9(b) as the dielectric constant of BSO increases. This makes a shallower and slightly wider quantum well with the smallest n_{2D} of purple line at the largest BSO dielectric constant value of 100. If the difference of dielectric constant is not large, the order can be reversed because of combination of changes in depth and width of quantum well.

There can be a section that has decreasing depth and increasing width of quantum well, which is why lines with dielectric constant of 10, 20, and 50 overlap. The tendency of n_{2D} and band slope change in the same way as the role of BSO dielectric constant in the change of the dielectric constant of LIO. When the dielectric constant of LIO rises from 25 to 38 and 50, n_{2D} goes down in Fig 4.9(c), making shallow quantum well at the interface with low band slope in Fig 4.9(d).

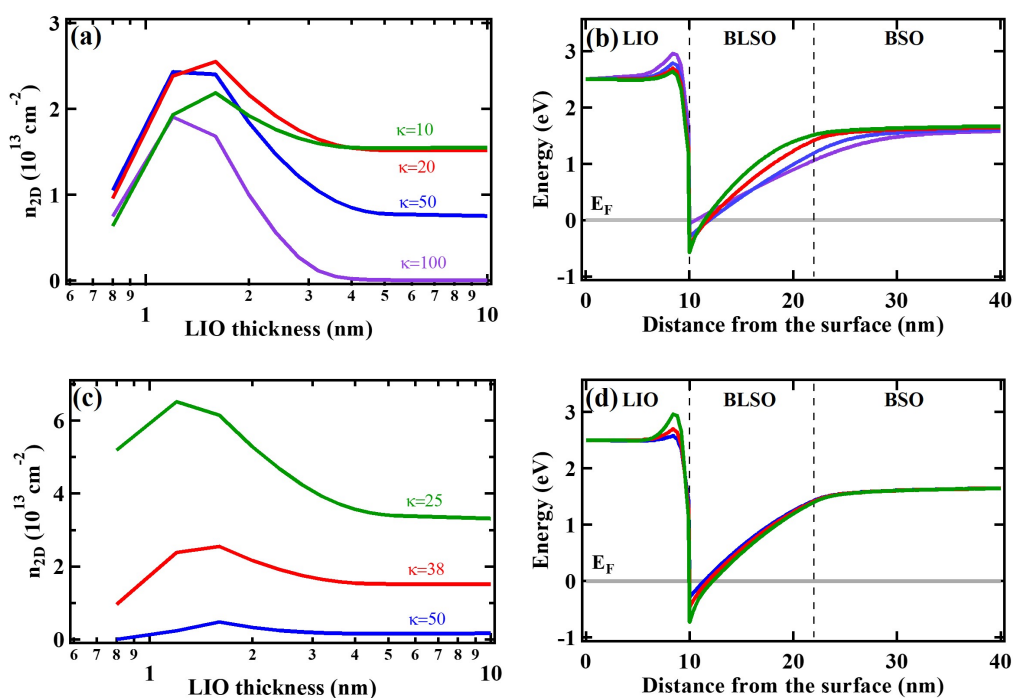


Fig 4.9 Influence of the dielectric constant of BSO and LIO on the LIO/BLSO interface calculated with the P-S equation. (a) Carrier densities of quantum well with BSO dielectric constants of 10, 20, 50, and 100 according to the LIO thickness. (b) Changes in minimum conduction band bending at each dielectric constant of BSO at LIO 10 nm. (c) Carrier densities of quantum well with LIO dielectric constants of 25, 38, and 50 according to the LIO thickness. (d) Changes in minimum conduction band bending at each dielectric constant of LIO at LIO 10 nm.

In addition, we can see one more phenomenon caused by change in dielectric constant. There is a high electric field at the interface with LIO dielectric constant of 25 in green line

of Fig 4.9(d) even though the dielectric constant of LIO barely affect the band slope near the quantum well where polarization exists, as can be seen in the role of deep donors in Fig 4.5(d). The change in the electric field at the interface is because the dielectric constant is connected to the electric field created by polarization. As the dielectric constant decreases, the electric field of the same polarization increases because the electric field is proportional to the polarization and inversely proportional to the dielectric constant. Small dielectric constant requires large polarization to create the same electric field. In fact, this is the main reason for making much higher n_{2D} at lower dielectric constant while n_{2D} in Fig 4.9(c) is also larger than n_{2D} in Fig 4.9(a) at the similar value of dielectric constant. And the dielectric constant plays a larger role in the formation of the 2D interface of LIO/BLSO than other material parameters because the dielectric constant varies over a large range compared to other parameters that vary only in a small range depending on materials or temperature. For example, the electron effective mass differs by about less than 10 times for each material. However, it is known that the dielectric constant of STO increases to 18000 at low temperature [77] while the dielectric constant of BSO and LIO hardly change with temperature change [78,79]. Therefore, it is important to have an appropriate value of dielectric constant. Too large dielectric constant can make the quantum well widen while greatly reducing the band slope, resulting in loss of 2D characteristics.

The change of conduction band offset gives the same results as changing the band gap, so the band gap change is not considered separately. The conduction band offset between LIO and BSO makes an electric field at the interface with the help of polarization, doing the same role as the polarization already shown in Fig 4.5(b). In Fig 4.10(a) and (b), three kinds of conduction band offset 1.0 eV, 1.6 eV, and 2.4 eV are described. The higher conduction band offset makes a higher electric field and a higher slope of the energy band at the interface in Fig 4.10(b), with a higher n_{2D} in Fig 4.10(a). A conduction band offset of

2.4 eV in blue line makes even more than $4 \times 10^{13} \text{ cm}^{-2}$ of n_{2D} with 0.2% La doped channel and 10 nm LIO. However, when the conduction band offset goes down to 1.0 eV, indicated by green line, there is almost no quantum well below the Fermi level in Fig 4.10(b) which means no carrier. To form a 2DEG on the LIO/BLSO interface, a conduction band offset of more than 1.0 eV is required. Fortunately, the conduction band offset between LIO and BSO is much greater than 1.0 eV with 1.6 eV and is much larger than the conduction band offset of other heterostructures shown in Table 4.1. The conduction band offsets of GaAs, GaN, ZnO interface are 0.35 eV, 1.1 eV, and 0.59 eV. These small values are because the alloyed one was used to make the conventional 2DEG interfaces making small difference in energy band with the non-alloyed film. But in LIO/BLSO 2DEG, a completely different two materials were used to make the interface, and the high conduction band offset is advantageous for making the high density of 2DEG.

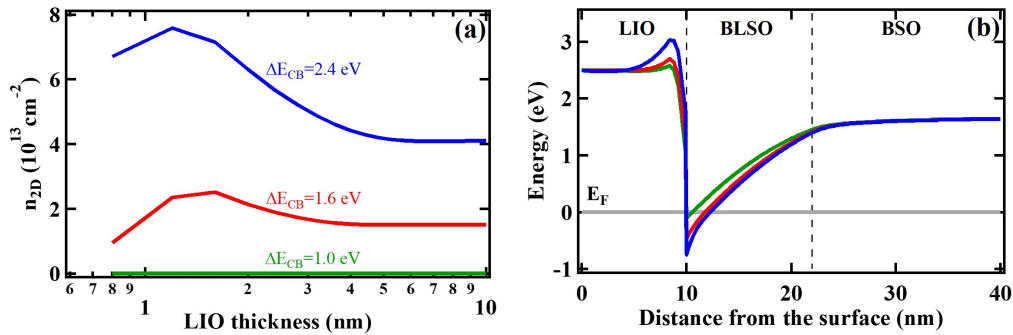


Fig 4.10 Influence of the conduction band offset between BSO and LIO on the LIO/BLSO interface calculated with the P-S equation. (a) Carrier densities of quantum well with conduction band offsets of 1.0 eV, 1.6 eV, and 2.4 eV according to the LIO thickness. (b) Changes in minimum conduction band bending at each conduction band offset at LIO 10 nm.

4.5. Comparison of two-dimensional electron gases

Based on the analysis of LIO/BSO interface, I organized and compared conventional 2DEGs and perovskite oxide 2DEGs including LAO/STO interface. Until now, there have been few studies describing LAO/STO as a semiconductor picture [37]. In particular, there has been no explanation of the electrical properties according to the LAO thickness. And the interface has been mainly explained with a “polar catastrophe” model [11] which is far from the methods of explaining other 2DEGs such as GaAs, GaN, and ZnO, whereas LIO/BSO can be described in the same way. Here I also tried to explain LAO/STO in the same picture as other 2DEGs, using P-S simulation that is also consistent with “polar catastrophe” model.

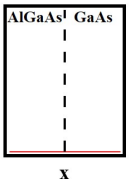
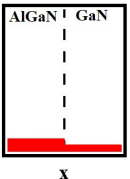
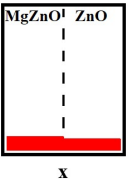
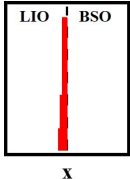
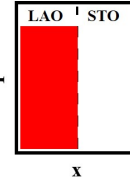
	$\text{Al}_{0.32}\text{Ga}_{0.68}\text{As}$ /GaAs	$\text{Al}_{0.32}\text{Ga}_{0.68}\text{N}$ /GaN	$\text{Mg}_{0.32}\text{Zn}_{0.68}\text{O}$ /ZnO	LaInO_3 /BaSnO ₃	LaAlO_3 /SrTiO ₃
2DEG n_{2D} (cm ⁻²)	$\sim 1 \times 10^{11}$	$\sim 1 \times 10^{13}$	$\sim 1 \times 10^{13}$	$1 \times 10^{13} \sim 3 \times 10^{13}$	$1 \times 10^{13} \sim 1 \times 10^{14}$
Point symmetry	GaAs : polar	GaN : polar	ZnO : polar	LIO : centrosymmetric	LAO : centrosymmetric
Interface layer	As -3 Ga +3	N -3 Ga +3	O -2 Zn +2	LaO +1 SnO ₂ 0	LaO +1 TiO ₂ -0.5 (Polar catastrophe)
m_e^*/m_0	0.096 / 0.067	0.37 / 0.27	0.49 / 0.30	0.46 / 0.42	0.42/4.2
κ	11.1 / 13.1	9.54 / 10.4	8.68 / 8.10	38 / 20	25/300
E_g (eV)	1.82 / 1.42	4.19 / 3.44	4.10 / 3.35	5.0/3.1	5.6/3.3
ΔE_C (eV)	0.35	1.1	0.59	1.6	2.6
P_{SP} ($\mu\text{C}\cdot\text{cm}^{-2}$)	0 / 0	4.56 / 2.90	7.43 / 5.40	-	55.9 (Polar catastrophe)
P_{PE} ($\mu\text{C}\cdot\text{cm}^{-2}$)	$< 1 \times 10^{-3}$ / 0	1.17 / -	1.10 / -	-	-
P_{int} ($\mu\text{C}\cdot\text{cm}^{-2}$)	-	-	-	60,60,25,10	-
P_{tot} ($\mu\text{C}\cdot\text{cm}^{-2}$)	$\Delta P = 0$ 	$\Delta P = 2.833$ 	$\Delta P = 0.93$ 	$\Delta P = P_{int}$ 	$\Delta P = 55.9$ 

Table 4.3 Materials parameters and interface properties at GaAs, GaN, ZnO, LIO/BSO, and LAO/STO 2DEGs.

Table 4.3 shows the materials and interfaces properties of GaAs, GaN, ZnO 2DEGs, together with LIO/BSO and LAO/STO perovskite oxide interfaces at room temperature. Most of parameters are the same as previously described. Each of the interfaces experimentally shows 2DEG n_{2D} of approximately 1×10^{11} , 1×10^{13} , 1×10^{13} , $1 \times 10^{13} \sim 3 \times 10^{13}$, $1 \times 10^{13} \sim 1 \times 10^{14}$ cm^{-2} at the GaAs, GaN, ZnO, LIO/BSO, and LAO/STO interface as mentioned in the introduction. The point symmetry of materials classified by structures shows whether the structure can have polarization. The zinc blende structure of GaAs and the wurtzite structure of GaN and ZnO are one of the hexagonal structures, which are classified as polar materials that can have spontaneous and piezoelectric polarization. However, as mentioned before, the orthorhombic structure of LIO has centrosymmetric, and rhombohedral LAO also have centrosymmetric, which cannot have any polarization. The interface layers were also described along with the charges of each layer. For the formation of 2DEG, specific termination layer is required, and understanding the differences between 2DEGs requires comparisons at each interface layer. The LAO/STO interface case is described with a explanation of “polar catastrophe” model [11]. Effective mass, dielectric constant, band gap, conduction band offset at each interface were described. All parameters of the GaAs, GaN, ZnO and LIO/BSO interfaces are the same as described in Table 4.1 and 4.2. The effective mass of LAO was put roughly because there is no reference, and other parameters of LAO and STO represent experimentally and calculationally obtained values [80-85]. The polarization values at each material are shown divided into spontaneous polarization (P_{SP}), piezoelectric polarization (P_{PE}), and interface polarization (P_{int}), and it is assumed that there exists constant spontaneous polarization at LAO, consistent with alternating LaO^+ and AlO_2^- of LAO/STO interface [11,23]. The constant polarization of LAO cannot be explained in terms of point symmetry yet, but I put the polarization value that can be obtained from the “polar catastrophe” model here [11].

For comparison, the total polarization graph at each material is shown in the last line of Table 4.3. Using these materials parameters, the results of the previously performed P-S calculations were compared with the newly calculated LAO/STO interface using same process.

In Table 4.4, it presents the simulation results of interfaces at a temperature of 300K with parameters of Table 4.3. First, it shows interface structure for P-S calculation in the same format of Fig 4.1, 4.2, and 4.3. Carrier concentrations and activation energies, polarization values and directions, and boundary conditions are described. The structures and boundary conditions were set slightly different for each interface. GaAs, GaN and ZnO interfaces have a “Schottky” boundary at the surface and “slope=0” boundary at the bottom of the sample, as mentioned earlier. The LIO/BSO interface has some separated BSO layers for the same simulation as the experiment and has an “ohmic” boundary condition because it assumes a deep carrier level at the center of the band gap. LAO/STO was also calculated using an “ohmic” boundary with a deep level in the center of the band gap. These are not the exact, but as mentioned before they do not primarily affect the results. For the charge neutrality condition at the bottom boundary with high deep carrier activation energies, thickness of STO was set to be thick. Table 4.4 also shows the minimum conduction band bending results and the properties of the quantum well. All five interfaces have quantum well at the interface below the Fermi level of 0 eV, with n_{2D} similar to the experimentally obtained values. All have 2D narrow quantum wells less than 5 nm at the interfaces, even including LAO/STO interface that have particularly large dielectric constant of STO. And I presented the tendency of conductance change as the overlayer thickness increased in the experiments that I mentioned earlier, including the LAO/STO case [15-19,86,87]. Most experiments show that the conductance saturates as the overlayer film thickens that is explained well with “constant polarization” model [16,18,19,87], and there are some experiments that show a slight decrease in conductance at thick overlayer at the GaN

interface and at the LAO/STO interface [17,86]. These properties of conductance change have explained by the “constant polarization” model with the help of strain relaxation at the GaN interface. And it can equally be applied to LAO/STO interface. Although LAO/STO has not yet been explained by a “constant polarization” model, the “polar catastrophe” model can be treated as a “constant polarization” model in semiconductor picture, and it explains the LAO thickness dependent conductance well. However, as shown in the previous figures, LIO/BSO has different thickness dependent conductance that vary on very short length scale, and it can only be explained by the “interface polarization” model. At a temperature of 300 K, all simulation results fit well with the experimental results, even at the LAO/STO interface, which has never been treated with semiconductor picture. Details can be changed in LIO/BSO and LAO/STO interface because the deep carriers were assumed to have activation energies of half of band gap. However, it is true that quantum wells are formed at the interfaces, and these results can explain experimental results.

Table 4.5 is the results of the same simulation at a temperature of 4 K. Materials parameters were set to the same values because there was no significant difference at low temperature except for the dielectric constant of STO. STO is known to have large dielectric constant at low temperature [77] and was set to 10,000 at 4 K. At a temperature of 4 K, quantum wells are well formed at GaAs, GaN, ZnO, and LIO/BSO interface with one or two bounded energies. However, the LAO/STO interface shows a thick quantum well of 18 nm width with many bounded states because of too large dielectric constant of STO which seems difficult to see 2D properties at low temperature. Some papers say that STO films do not have large dielectric constant at low temperature [88]. In this case, the LAO/STO interface may also have a narrow quantum well at low temperature. From this comparison of five 2DEGs, I was able to understand the big principle in the semiconductor picture that explains all the 2DEGs.

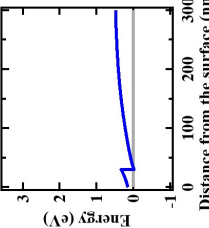
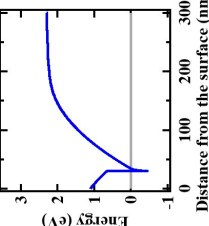
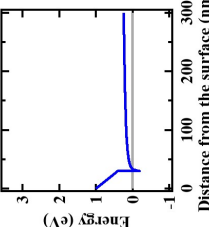
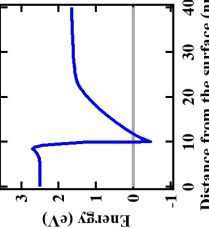
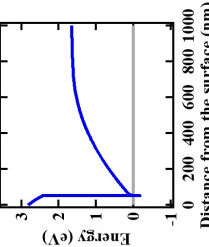
T=300 K	Al _{0.32} Ga _{0.68} As /GaAs	Al _{0.32} Ga _{0.68} N /GaN	Mg _{0.37} Zn _{0.63} O /ZnO	LaInO ₃ /BaSnO ₃	LaAlO ₃ /SrTiO ₃
<p>Interface structure</p>	<p>Schottky barrier = 0.15 eV</p> <p>Si-doped Al_{0.32}Ga_{0.68}As 30 nm $N_{DP} = 1 \times 10^{17} \text{ cm}^{-3}$ ($E_g = 0.05 \text{ eV}$) $N_{DA} = 1 \times 10^{16} \text{ cm}^{-3}$ ($E_g = 0.38 \text{ eV}$)</p> <p>GaAs 500 nm $N_{DP} = 1 \times 10^{16} \text{ cm}^{-3}$ ($E_g = 0.44 \text{ eV}$) $N_{DA} = 1 \times 10^{16} \text{ cm}^{-3}$ ($E_g = 0.38 \text{ eV}$)</p> <p>Slope=0</p>	<p>Schottky barrier = 1.1 eV</p> <p>Al_{0.32}Ga_{0.68}N 30 nm $N_{DP} = 1 \times 10^{16} \text{ cm}^{-3}$ ($E_g = 0.53 \text{ eV}$) $N_{DA} = 1 \times 10^{17} \text{ cm}^{-3}$ ($E_g = 1.2 \text{ eV}$)</p> <p>GaN 500 nm $N_{DP} = 1 \times 10^{16} \text{ cm}^{-3}$ ($E_g = 0.53 \text{ eV}$) $N_{DA} = 1 \times 10^{17} \text{ cm}^{-3}$ ($E_g = 1.2 \text{ eV}$)</p> <p>Slope=0</p>	<p>Schottky barrier = 1.0 eV</p> <p>Mg_{0.37}Zn_{0.63}O 30 nm $N_{DP} = 1 \times 10^{16} \text{ cm}^{-3}$ ($E_g = 0.3 \text{ eV}$) $N_{DA} = 1 \times 10^{15} \text{ cm}^{-3}$ ($E_g = 0.2 \text{ eV}$)</p> <p>ZnO 500 nm $N_{DP} = 1 \times 10^{16} \text{ cm}^{-3}$ ($E_g = 0.3 \text{ eV}$) $N_{DA} = 1 \times 10^{15} \text{ cm}^{-3}$ ($E_g = 0.2 \text{ eV}$)</p> <p>Slope=0</p>	<p>Ohmic</p> <p>LaInO₃ 10 nm $N_{DP} = 1.3 \times 10^{20} \text{ cm}^{-3}$ ($E_g = 2.5 \text{ eV}$) $P_{int} = 60/60/25/10 \mu\text{C}\cdot\text{cm}^{-2}$</p> <p>(Ba,La)SnO₃ 12 nm $N_D = 2.86 \times 10^{19} \text{ cm}^{-3}$ ($E_g = -0.63 \text{ eV}$) $N_{DA} = 4 \times 10^{19} \text{ cm}^{-3}$ ($E_g = 1.55 \text{ eV}$)</p> <p>BSO 30 nm $N_{DA} = 4 \times 10^{19} \text{ cm}^{-3}$ ($E_g = 1.55 \text{ eV}$)</p> <p>BSO 100 nm</p> <p>Ohmic</p>	<p>Ohmic</p> <p>LaAlO₃ 50 nm $N_{DP} = 1 \times 10^{17} \text{ cm}^{-3}$ ($E_g = 2.8 \text{ eV}$) $N_{DA} = 1 \times 10^{17} \text{ cm}^{-3}$ ($E_g = 2.8 \text{ eV}$)</p> <p>SrTiO₃ 3000 nm $N_{DP} = 1 \times 10^{17} \text{ cm}^{-3}$ ($E_g = 1.65 \text{ eV}$) $N_{DA} = 1 \times 10^{17} \text{ cm}^{-3}$ ($E_g = 1.65 \text{ eV}$)</p> <p>Ohmic</p>
<p>Conduction band bending simulated by P-S equation</p>					
<p>2DEG n_{2D} (cm⁻²) from simulation</p>	<p>2.49 × 10¹¹</p>	<p>1.51 × 10¹³</p>	<p>4.84 × 10¹²</p>	<p>1.52 × 10¹³</p>	<p>3.41 × 10¹⁴</p>
<p>Quantum well depth / width from simulation</p>	<p>0.0213 eV / 3.2 nm</p>	<p>0.451 eV / 4.2 nm</p>	<p>0.187 eV / 3.2 nm</p>	<p>0.5 eV / 1.8 nm</p>	<p>0.178 eV / 1.6 nm</p>
<p>Conductance change with increasing overlayer thickness (experiment)</p>	<p>increase → saturation (at >20 nm AlGaAs)</p>	<p>increase → saturation (at ~20 nm AlGaN) increase → slight decrease (at ~15 nm AlGaN)</p>	<p>increase → saturation (at ~100 nm MgZnO)</p>	<p>increase → slight decrease (at ~1.6 nm LaInO₃)</p>	<p>increase → saturation (at ~2 nm LaAlO₃) increase → decrease (at ~5 nm LaAlO₃)</p>
<p>Model for overlayer thickness dependence</p>	<p>Constant polarization discontinuity</p>	<p>Constant polarization discontinuity, Strain relaxation</p>	<p>Constant polarization discontinuity</p>	<p>Interface polarization discontinuity</p>	<p>Constant polarization discontinuity (Polar catastrophe)</p>

Table 4.4 Simulation results of GaAs, GaN, ZnO, LIO/BSO, and LAO/STO 2DEGs at temperature of 300K.

4.5. Conclusion

We investigated how the oxide 2DEG of LIO/BLSO with high n_{2D} is formed discussing what role 13 kinds of material parameters play in the forming quantum well based on the “interface polarization” model. With reliable P-S simulations, we have obtained theoretical results that are well understood physically. We first set two unknown parameters, polarization and deep donor density of LIO, to fit experimental results and investigated the changes that the two values make. Next, the effects of changing donor density and deep acceptor density of BSO, deep state activation energy, effective mass, dielectric constant, and conduction band offset were studied with the aid of approximation of Poisson equation and Schrödinger equation. Through these analyzes, we realized the speciality of the LIO and BSO material parameters for forming quantum well with high n_{2D} and understood all kinds of 2DEG systems.

References

- [1] T. Mimura, *Jpn. J. Appl. Phys.* **44**, 8263 (2005).
- [2] J. A. Simmons, H. P. Wei, L. W. Engel, D. C. Tsui, and M. Shayegan, *Phys. Rev. Lett.* **63**, 1731 (1989)
- [3] O. Ambacher, J. Smart, J. R. Shealy, N. G. Weimann, K. Chu, M. Murphy, W. J. Schaff, L. F. Eastman, R. Dimitrov, L. Wittmer, M. Stutzmann, W. Rieger, and J. Hilsenbeck, *J. Appl. Phys.* **85**, 3222 (1999).
- [4] H. Tampo, H. Shibata, K. Matsubara, A. Yamada, P. Fons, S. Niki, M. Yamagata, and H. Kanie, *Appl. Phys. Lett.* **89**, 132113 (2006).
- [5] L. Pfeiffer, K. W. West, H. L. Stormer, and K. W. Baldwin, *Appl. Phys. Lett.* **55**, 1888 (1989).
- [6] M. J. Manfra, L. N. Pfeiffer, K. W. West, H. L. Stormer, K. W. Baldwin, J. W. P. Hsu, D. V. Lang, and R. J. Molnar, *Appl. Phys. Lett.* **77**, 2888 (2000).
- [7] A. Tsukazaki, H. Yuji, S. Akasaka, K. Tamura, K. Nakahara, T. Tanabe, H. Takasu, A. Ohtomo, and M. Kawasaki, *Appl. Phys. Express* **1**, 055004 (2008).
- [8] Z. Schlesinger, W. I. Wang, and A. H. MacDonald, *Phys. Rev. Lett.* **58**, 73 (1987).
- [9] G. Herranz, F. Sa´nchez, N. Dix, M. Scigaj, and J. Fontcuberta, *Sci. Rep.* **2**, 758 (2012).
- [10] S. Thiel, G. Hammerl, A. Schmehl, C. W. Schneider, J. Mannhart, *Science* **313**, 5795, pp. 1942-1945 (2006).
- [11] U. Kim, C. Park, Y. M. Kim, J. Shin, and K. Char, *APL Mater.* **4**, 071102 (2016).
- [12] Y. Kim, Y. M. Kim, J. Shin, and K. Char, *APL Mater.* **6**, 096104 (2018).
- [13] D. Song, M. Jeong, J. Kim, B. Kim, J. H. Kim, J. H. Kim, K. Lee, and K. Char, “High-k perovskite gate oxide for modulation beyond 10^{14} cm⁻²” (unpublished).
- [14] P. M. Solomon and H. Morkoc, *IEEE Trans. Electron Devices* ED-31, **8**, 1015 (1984).
- [15] T. Saku, Y. Hirayama, and Y. Horikoshi, *Jpn. J. Appl. Phys.* **30**, 902 (1991).
- [16] G. Liu, J. Wu, Y. Lu, Z. Li, Y. Song, C. Li, S. Yang, X. Liu, Q. Zhu, and Z. Wang, *J. Appl. Phys.* **110**, 023705 (2011).
- [17] J. P. Ibbetson, P. T. Fini, K. D. Ness, S. P. DenBaars, J. S. Speck, and U. K. Mishra, *Appl. Phys. Lett.* **77**, 250 (2000).
- [18] Y. Takei, K. Tsutsui, W. Saito, K. Kakushima, H. Wakabayashi, and H. Iwai, *Jpn. J. Appl. Phys.* **55**, 040306 (2016).

- [19] J. D. Ye, S. Pannirselvam, S. T. Lim, J. F. Bi, X. W. Sun, G. Q. Lo, and K. L. Teo, *Appl. Phys. Lett.* **97**, 111908 (2010).
- [20] A. Savoia, D. Paparo, P. Perna, Z. Ristic, M. Salluzzo, F. Miletto Granozio, U. Scotti di Uccio, C. Richter, S. Thiel, J. Mannhart, and L. Marrucci, *Phys. Rev. B* **80**, 075110 (2009).
- [21] W. Siemons, G. Koster, H. Yamamoto, W. A. Harrison, G. Lucovsky, T. H. Geballe, D. H. A. Blank, and M. R. Beasley, *PRL* **98**, 196802 (2007).
- [22] H. J. Kim, U. Kim, H. M. Kim, T. H. Kim, H. S. Mun, B.-G. Jeon, K. T. Hong, W.-J. Lee, C. Ju, K. H. Kim, and K. Char, *Appl. Phys. Express* **5**, 061102 (2012).
- [23] Y. M. Kim, T. Markurt, Y. Kim, M. Zupancic, J. Shin, M. Albrecht, and K. Char, *Sci. Rep.* **9**, 16202 (2019).
- [24] D. Jena, Ph.D. thesis, University of Californial Santa Barbara, 2003.
- [25] Y. M. Kim, Y. Kim, and K. Char, *Commun. Mater.* **2**, 73 (2021).
- [26] E. B. Ramayya and I. Knezevic, *J. Comput. Electron.* **9**, 206 (2010).
- [27] J. -F. Mennemann, A. Jüngel, and H. Kosina, *J. Comput. Phys.* **239**, 187 (2013).
- [28] M. Pourfath, H. Kosina, and S. Selberherr, *J. Comput. Electron.* **5**, 155 (2006).
- [29] I-H. Tan, G. L. Snider, L. D. Chang, and E. L. Hu, *J. Appl. Phys.* **68**, 4071 (1990).
- [30] H. Choi, M. Kim, J.-Y. Moon, J.-H. Lee, and S.-K. Son, *J. Nanosci. Nanotechnol.* **20**, 4428, (2020).
- [31] T. Scheinert, T. Mikolajick, and S. Schmult, *AIP Advances* **9**, 125018 (2019).
- [32] R. Singh, M. A. Khan, S. Mukherjee, *IEEE Trans. Electron Devices*, **64**, NO. 9, 3661(2017).
- [33] I. A. Larkin and J. H. Davies, *Phys. Rev. B* **52**, 5535(R) (1995).
- [34] A. M. Cruz Serra, and H. Abreu Santos, *J. Appl. Phys.* **70**, 2734 (1991).
- [35] B. Sarikavak-Lisesivdin, *Philos. Mag.* **93**, No. 9, 1124 (2013).
- [36] S. Sasa, T. Tamaki, K. Koike, M. Yano and M. Inoue, *J. Phys.: Conf. Ser.* **109**, 012030 (2008).
- [37] A. Janotti, L. Bjaalie, L. Gordon, and C. G. Van de Walle, *Phys. Rev. B* **86**, 241108(R) (2012)
- [38] S. Su, J. H. You, and C. Lee, *J. Appl. Phys.* **113**, 093709 (2013).
- [39] K. Krishnaswamy, L. Bjaalie, B. Himmetoglu, , A. Janotti, L. Gordon, and Chris G. Van de Walle, *Appl. Phys. Lett.* **108**, 083501 (2016).
- [40] S. Adachi, *J. Appl. Phys.* **58**, R1 (1985).

- [41] S. M. Sze and K. K. Ng, *Physics of Semiconductor Devices* (Wiley, 2007).
- [42] T. Kozawa, T. Mori, T. Ohwaki, Y. Taga and N. Sawaki, *Jpn. J. Appl. Phys.* **39**, 772 (2000).
- [43] R. N´uñez-González, A. Reyes-Serrato, A. Posada-Amarillas, and D. H. Galván, *REVISTA MEXICANA DE FÍSICA S* **54** (2), 111 (2008).
- [44] Y.-N. Xu and W. Y. Ching, *Phys. Rev. B* **48**, 4335 (1993).
- [45] A. T. Collins, E. C. Lightowers, and P. J. Dean, *Phys. Rev.* **158**, 833 (1967)
- [46] Z. Li, P. Wang, J. He, H. Chen, J. Cheng, *Superlattices Microstruct.* **111**, 852 (2017).
- [47] J. G. Lu, S. Fujita, T. Kawaharamura, H. Nishinaka, Y. Kamada, and T. Ohshima, *Appl. Phys. Lett.* **89**, 262107 (2006).
- [48] A. Tsukazaki, A. Ohtomo, T. Kita, Y. Ohno, H. Ohno, M. Kawasaki, *Science* **315**, Issue 5817, 1388 (2007).
- [49] H. Yin, J. Chen, Y. Wang, J. Wang, and H. Guo, *Sci. Rep.* **7**, 41567 (2017).
- [50] H. Tampo, H. Shibata, K. Maejima, A. Yamada, K. Matsubara, P. Fons, S. Kashiwaya, S. Niki, Y. Chiba, T. Wakamatsu, and H. Kanie, *Appl. Phys. Lett.* **93**, 202104 (2008).
- [51] B. A. Lombos, *Can. J. Chem.* **63**, 1666 (1985).
- [52] M. O. Watanabe, K. Morizuka, M. Mashita, Y. Ashizawa, and Y. Zohta, *Jpn. J. Appl. Phys.* **23**, L103 (1984).
- [53] M. M. Sobolev, F. Yu. Soldatenkov, and V. A. Kozlov, *Semiconductors* **50**, 924 (2016).
- [54] B. Vinter, *Appl. Phys. Lett.* **44**, 307 (1984).
- [55] M. J. Uren, K. J. Nash, R. S. Balmer, T. Martin, E. Morvan, N. Caillas, S. L. Delage, D. Ducatteau, B. Grimbert, and J. C. De Jaeger, *IEEE Trans. Electron Devices*, **53**, no. 2, 395 (2006).
- [56] T. T. Duc, G. Pozina, E. Janzén, and C. Hemmingsson, *J. Appl. Phys.* **114**, 153702 (2013).
- [57] Z. Xie, Y. Sui, J. Buckeridge, C. R. A. Catlow, T. W. Keal, P. Sherwood, A. Walsh, M. R. Farrow, D. O. Scanlon, S. M. Woodley, and A. A. Sokol, *J. Phys. D: Appl. Phys.* **52** 335104 (2019).
- [58] D.C. Look, *Materials Science and Engineering* **B80**, 383 (2001).
- [59] H. von Wenckstern, R. Pickenhain, H. Schmidt, M. Brandt, G. Biehne, M. Lorenz, M. Grundmann, and G. Brauer, *Appl. Phys. Lett.* **89**, 092122 (2006).
- [60] M. Higashiwaki, S. Chowdhury, M.-S. Miao, B. L. Swenson, C. G. Van de Walle, and U. K. Mishra, *J. Appl. Phys.* **108**, 063719 (2010).

- [61] J. Ghosh, International Conference on Electron Devices and Solid-State Circuits (EDSSC), pp. 1-4 (2017).
- [62] N. Goyal, B. Iñiguez, and T. A. Fjeldly, *Appl. Phys. Lett.* **101**, 103505 (2012).
- [63] J. Shin, Y. M. Kim, Y. Kim, C. Park, and K. Char, *Appl. Phys. Lett.* **109**, 262102 (2016).
- [64] J. Nowotny, *Science of Ceramic interface II* (Elsevier Science Publisher B. V., Amsterdam, The Netherlands, 1994) p. 349.
- [65] H. M. Park, H. J. Lee, S. H. Park, and H. I. Yoo. *Acta Cryst.* **C59**, i131-i132 (2003).
- [66] C. J. Roh, M.-C. Jung, J. R. Kim, K.-J. Go, J. Kim, H. J. Oh, Y.-R. Jo, Y. J. Shin, J. G. Choi, B.-J. Kim, D. Y. Noh, S.-Y. Choi, T. W. Noh, M. J. Han, and J. S. Lee, *Small* **16**, 2003055 (2020).
- [67] A. Slassi, *Mater. Sci. Semicond. Process.* **32**, 100 (2015).
- [68] U. Kim, C. Park, T. Ha, R. Kim, H. S. Mun, H. M. Kim, H. J. Kim, T. H. Kim, N. Kim, J. Yu, K. H. Kim, J. H. Kim, and K. Char, *APL Mater.* **2**, 056107 (2014).
- [69] P. Singh, B. J. Brandenburg, C. P. Sebastian, P. Singh, S. Singh, D. Kumar, and O. Parkash, *Jpn. J. Appl. Phys.* **47**, 3540 (2008).
- [70] H. J. Kim, U. Kim, T. H. Kim, J. Kim, H. M. Kim, B.-G. Jeon, W.-J. Lee, H. S. Mun, K. T. Hong, J. Yu, K. Char, and K. H. Kim, *Phys. Rev. B* **86**, 165205 (2012).
- [71] U. Kim, C. Park, T. Ha, Y. M. Kim, N. Kim, C. Ju, J. Park, J. Yu, J. H. Kim, and K. Char, *APL Materials* **3**, 036101 (2015).
- [72] K. Xiong, J. Robertson, and S. J. Clark, *Appl. Phys. Lett.* **89**, 022907 (2006).
- [73] L. Yu and A. Zunger, *Nat. Commun.* **5**, 5118 (2014).
- [74] Y. Liu, Y. Zhou, D. Jia, J. Zhao, B. Wang, Y. Cui, Q. Li, and B. Liu, *Journal of Materials Science & Technology* **42**, 212 (2020).
- [75] W. Zhong, R.D. King-Smith, and D. Vanderbilt, *Phys. Rev. Lett.* **72**, 3618 (1994)
- [76] Y. Kim, H. Cho, and K. Char, *Appl. Phys. Lett.* **118**, 052101 (2021).
- [77] H. E. Weaver, *J. Phys. Chem. Solids* **11**, 274 (1959).
- [78] W. Nunn, A. Prakash, A. Bhowmik, R. Haislmaier, J. Yue, J. M. G. Lastra, and B. Jalan, *APL Mater.* **6**, 066107 (2018).
- [79] D. H. Jang, W.-J. Lee, E. Sohn, H. J. Kim, D. Seo, J.-Y. Park, E. J. Choi, and K. H. Kim, *J. Appl. Phys.* **121**, 125109 (2017).
- [80] W. Wunderlich, H. Ohta, K. Koumoto, arXiv:0808.1772 (2008).
- [81] G. A. Samara, *J. Appl. Phys.* **68**, 4214 (1990).
- [82] B. K. Choudhury, K. V. Roa, R. N. P. Choudhury, *J. Mater. Sci.* **24** 3469 (1989).

- [83] S.-G. Lim, S. Kriventsov, and T. N. Jackson, J. H. Haeni, D. G. Schlom, A. M. Balbashov, R. Uecker, P. Reiche, J. L. Freeouf, and G. Lucovsky, *J. Appl. Phys.* **91**, 4500 (2002).
- [84] K. van Benthem, C. Elsässer, and R. H. French, *J. Appl. Phys.* **90**, 6156 (2001).
- [85] G. Berner, A. Müller, F. Pfaff, J. Walde, C. Richter, J. Mannhart, S. Thiess, A. Gloskovskii, W. Drube, M. Sing,¹ and R. Claessen¹, *Phys. Rev. B* **88**, 115111 (2013).
- [86] G. Herranz, F. Sánchez, N. Dix, M. Scigaj and J. Fontcuberta, *Sci. Rep.* **2**, 758 (2012).
- [87] C. Li, Y. Hong, H. Xue, X. Wang, Y. Li, K. Liu, W. Jiang, M. Liu, L. He, R. Dou, C. Xiong, and J. Nie, *Sci. Rep.* **8**, 404 (2018).
- [88] H.W. Jang, A. Kumar, S. Denev, M. D. Biegalski, P. Maksymovych, C.W. Bark, C. T. Nelson, C. M. Folkman, S. H. Baek, N. Balke, C. M. Brooks, D. A. Tenne, D. G. Schlom, L. Q. Chen, X. Q. Pan, S.V. Kalinin, V. Gopalan, and C. B. Eom, *PRL* **104**, 197601 (2010).

Chapter 5. Future direction of $\text{LaInO}_3/\text{BaSnO}_3$ and possibility of other BaSnO_3 based interface

In this chapter, I will discuss the speciality of LIO/BLSO interface and its future direction. From the analysis based on chapter 4, 4 kinds of main properties of LIO/BLSO interface can be seen, and the reduction of deep acceptor density of BSO show improvement of the interface making deeper and wider quantum well with higher 2D carrier density. There are also several ways to improve LIO/BLSO interface, which have not been exactly explained yet. I will also predict other 2DEG using other materials instead of LIO, based on BSO, with the advantage of not having to create termination-controlled surface.

5.1. Properties of $\text{LaInO}_3/\text{BaSnO}_3$ interface

From the roles of 13 kinds of material parameters, we can see the LIO and BSO materials parameters are appropriate to form the 2DEG with high carrier density. First, the polarization value is large enough to form deep quantum well making large electric field at the interface though it is located only near the interface. Second, deep state carriers seem to have appropriate values not trapping all the electron carriers in BSO channel and screening the negative polarization charge enough in LIO. Third, shallow donor of BSO can be adjusted according to the intention by La doping changing quantum well depth. Forth, LIO and BSO have not too small effective mass, not too large dielectric constant, and have large enough conduction band offset. Among many kinds of perovskite oxides, the lattice matched two materials with the appropriate material parameters could form 2DEG interface.

Based on these properties, I can think of big four differences between the LIO/BLSO interface and conventional 2DEGs. First, in the LIO/BLSO, the electric field at the interface made by polarization and conduction band offset is much larger than that of the

conventional 2DEGs shown in Fig 5.1, Table 4.1, and 4.2. And this helps to form deep and narrow quantum well with a depth of 0.43 eV and a width of 1.1 nm in the blue line of Fig 5.2 calculated with an undoped channel layer and 10 nm LIO when the BSO deep acceptor density is $4 \times 10^{19} \text{ cm}^{-3}$ at temperature of 4K. In Fig 4.1, 4.2, and 4.3, the three types of 2DEG have a quantum well of a depth of 0.05~0.46 eV and width of 5~12 nm. This property helps the formation of high n_{2D} in the LIO/BLSO interface. Second, there is no band slope on the LIO surface while three conventional 2DEGs have an electric field at the surface boundary of alloyed layer. For the GaAs interface, the slope occurs from the pinned Fermi level of the surface, which is made by surface deep states. And the band slope of the GaN and ZnO interfaces is due to the constant polarization across the whole alloyed layer added to a pinned Fermi level, whereas the LIO has polarization and electric field only near the interface because all polarization charges are screened by large density of ionized deep donor and flatten the band before the end of LIO surface. Above a certain thickness of LIO, we can see flat band near the surface from the previous calculation results. Even if I set the boundary condition of the LIO to have Fermi level pinning like conventional 2DEGs, lowering deep state activation energy like in Fig 4.7(c) and (d), large number of deep donors still can flatten all the conduction band slope. However, relatively small amounts of deep carriers of AlGaN and MgZnO cannot screen space charges from polarization enough and remain electric field at the surface. This will make the surface stable without electric field in LIO/BLSO. Third, there is possibility of Rashba effect at the LIO/BLSO interface created by large spin-orbit coupling because there is large electric field at the interface, and LIO and BSO have higher atomic masses compared to other materials that form 2DEGs. If there is Rashba effect at the interface, the energy eigenvalue with high energy and n_{2D} can be used in spintronics, separating electrons to spin up and spin down clearly. Fourth, perovskite structure of LIO and BSO can be combined with other perovskite material that

have novel properties such as ferroelectric. This combination will make possible to pioneer fields that have not been studied so far. And the high dielectric constant of perovskite oxide materials including LIO will be able to modulate high carrier density of LIO/BLSO 2DEG [1].

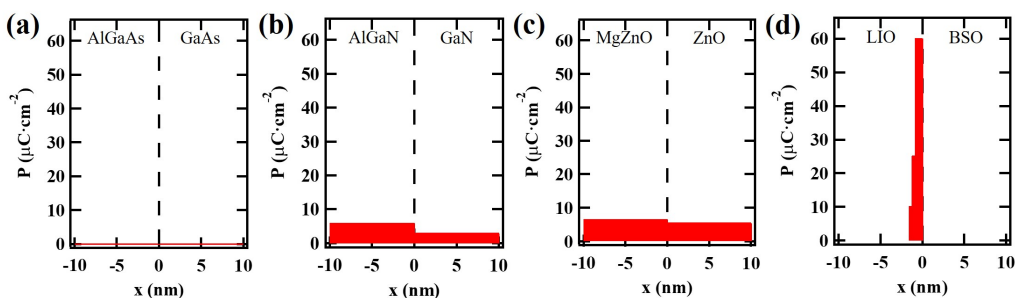


Fig 5.1 Polarization distributions at (a) AlGaAs/GaAs (b) AlGaN/GaN (c) MgZnO/ZnO (d) LIO/BSO interface.

5.2. Reduction of dislocation density

Most material parameters of LIO and BSO cannot be changed. However, if we find the way to reduce dislocation density of BSO film, deep acceptor density can be reduced. We are trying to reduce the deep acceptor density by using substrates such as $\text{Ba}_2\text{ScNbO}_6$, BSO, and LIO that have almost same lattice constants with the BSO channel layer [2-4]. We investigated what we can get if we reduce the deep acceptor density with this way, looking more clearly at the energy band and energy eigenvalues, similar to the calculations I have already done in Fig 4.6(a) and (b) at the temperature of 300 K. Here, I calculated at the temperature of 4 K to see the energy eigenvalues clearly and compare them with the results of Fig 4.1, 4.2, and 4.3. And the undoped BSO channel was used to make a clear difference. In the blue line in Fig 5.2(a), the conduction band minimum that makes the 2DEG is plotted, along with the already known parameters, including deep acceptor density of $4 \times 10^{19} \text{ cm}^{-3}$

obtained from experimental electrical properties under optimal growth conditions of the sample [1,5]. And the conduction band minimum with deep acceptor density of 1×10^{18} and $1 \times 10^{19} \text{ cm}^{-3}$ are also presented that have a deeper and wider quantum well indicated by the green and red line. They have n_{2D} of $8.89 \times 10^{10} \text{ cm}^{-3}$ in blue line, $1.87 \times 10^{13} \text{ cm}^{-3}$ in red line, and $3.19 \times 10^{13} \text{ cm}^{-3}$ in green line. In Fig 5.2(b), the energy bands are enlarged and the eigenvalues of three types of deep acceptor density are presented. The eigenvalues are -0.0004 eV at deep acceptor density of $4 \times 10^{19} \text{ cm}^{-3}$, -0.1063 eV at $1 \times 10^{19} \text{ cm}^{-3}$, and -0.0123 eV and -0.1693 eV at $1 \times 10^{18} \text{ cm}^{-3}$ with undoped BSO channel. Quantum well gets deeper and wider with lower deep acceptor density and creates higher energies of carriers that make high density of state in 2D. At BSO deep acceptor density of $1 \times 10^{18} \text{ cm}^{-3}$, it has over $3 \times 10^{13} \text{ cm}^{-3}$ of n_{2D} at 10 nm LIO and over $4 \times 10^{13} \text{ cm}^{-3}$ of n_{2D} at 4 unit cell LIO, even using the channel without doping at temperature of 4 K. Using an undoped BSO channel helps to avoid ionized impurity scattering in the channel. Compared to conventional 2DEGs, the n_{2D} of 2DEG will be much larger than now with reducing deep acceptor density of BSO. This would be a great advantage of LIO/BLSO 2DEG.

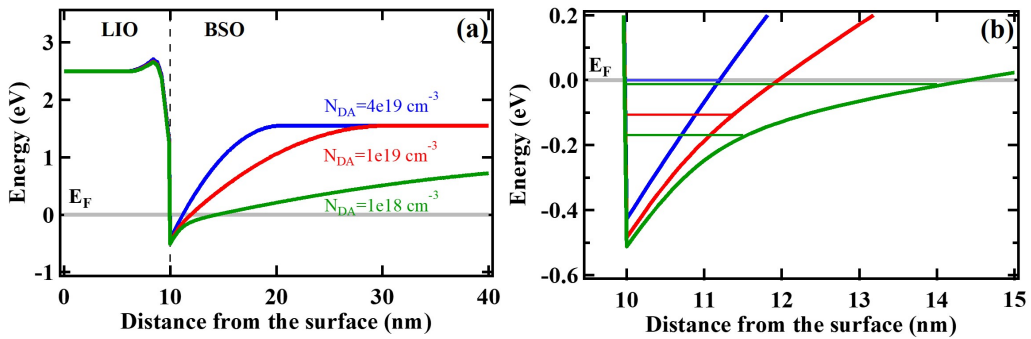


Fig 5.2 Influence of reduced deep acceptor density of BSO on the LIO/undoped BSO interface calculated with the P-S equation at temperature 4 K. (a) Minimum conduction band bending of the interface with $1 \times 10^{18} \text{ cm}^{-3}$, $1 \times 10^{19} \text{ cm}^{-3}$, and $4 \times 10^{19} \text{ cm}^{-3}$ deep acceptor density. (b) Enlarged views of band near the interface and subband energies of the 2D quantum wells at each deep acceptor densities of BSO.

5.3. Additional conductance enhancement of $\text{LaInO}_3/\text{BaSnO}_3$ interface

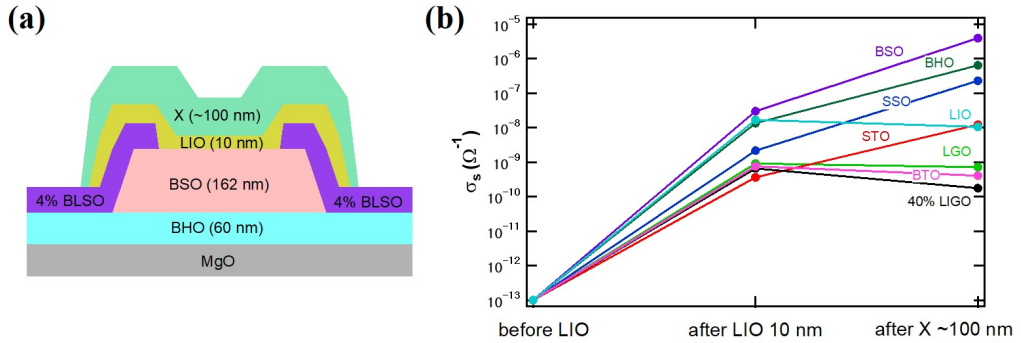


Figure 5.3 Experiments for the enhancement of LIO/BLSO conductance. (a) Structure of 2DEG interface that has additional X layer on LIO layer. (b) Conductance enhancement after deposition of about 100 nm material X on LIO.

There are several experimental results of the LIO/BLSO interface showing higher conductance by depositing materials over the LIO/BLSO interface. In Fig 5.3, samples with extra layer of various materials X on LIO/BLSO interface show extra conductance enhancement even after the conductance enhancement made by deposition of 10 nm LIO layer. I deposited insulating perovskite oxides BSO, BHO, SrSnO_3 (SSO), STO, LIO, BaTiO_3 (BTO), LaGaO_3 (LGO), $\text{La}(\text{In,Ga})\text{O}_3$ (LIGO) on top to the LIO/BSO interface. XRD measurement roughly confirmed the structural characteristics and I thought that it would have grown epitaxially. However, more study about their structural properties on LIO layer are needed. And the interfaces between BSO and material Xs did not showed any conductance enhancement. There was an additional conductance enhancement with only a few Xs and some did not show enhancement. BSO, BHO, SSO, STO showed conductance enhancement after deposition of them, but deposition of BTO, LGO, and LIGO had similar property with thick LIO showing slightly decreasing conductance. I tried to find something in common of the Xs that shows additional conductance enhancement

because it can be connected to the mechanism of 2DEG making quantum well deeper. Classification of Xs using conduction band offset based on LIO, material structure, lattice constant based on LIO and BSO, and presence of polarization were tried. Higher strain gradient made by lattice strain or additional polarization of X can make quantum well deeper. However, there were nothing in common. BSO, SSO, STO, and BTO have lower conduction band than LIO, and BHO, LGO, and LIGO have higher conduction band [6-9]. BSO, BHO, and STO have cubic structure while SSO, LIO, LGO, and LIGO have orthorhombic structure. Lattice constant of SSO, STO, BTO, LGO, and LIGO are smaller than LIO and BSO while the BHO has larger lattice constant [10-16]. BSO, BHO, SSO, and STO do not have polarization because their structures have inversion symmetry, and LIO, LGO and LIGO can have polarization presented in chapter 4, while BTO is known to have polarization structurally. The band bending results including X using P-S equation also could not explain the additional conductance enhancement. To explain this, further research on the cause of 2DEG formation is needed. The exact cause will be only understood when the interface formation mechanism is clearly explained.

Another improved conductance was observed in inverted LIO/BSO interface. I made same interface only changing the deposition order of LIO and BSO. Considering BSO that has similar or worse electrical properties when it use thicker buffer layer than about 200 nm [17], 2DEG with the BSO channel should be similar or worse in structure Fig 5.4(a). However, in Fig 5.4(b), the conductance of the interface is higher than the results of Fig 5.4(d) that has the interface made with the previously used structure of Fig 5.4(c). At 4 unit cell of LIO, it is about 50 times higher at inverted structure we have never seen. The trend as the LIO thickness changes is same in both cases. From this, we can think the mechanism of this conductance is same and the only difference would be the depth of quantum well for some reason. The results with 0.2% La-doped BSO channel also shows same trend in

Fig 5.5.

There can be two reasons for this phenomenon. First, the polarization value at the inverted structure of Fig 5.4(a) can be higher which cannot be confirmed by experiments now. Second, the termination-controlled layer of LIO can be easily obtained than BSO surface. LIO/BSO 2DEG interface need termination-controlled surface and LIO can be deposited with 100% LaO terminated surface while BSO is deposited with less than 100% SnO₂ terminated surface. This can be confirmed with the experiments of LIO/BSO interface with the BSO surface that is controlled well.

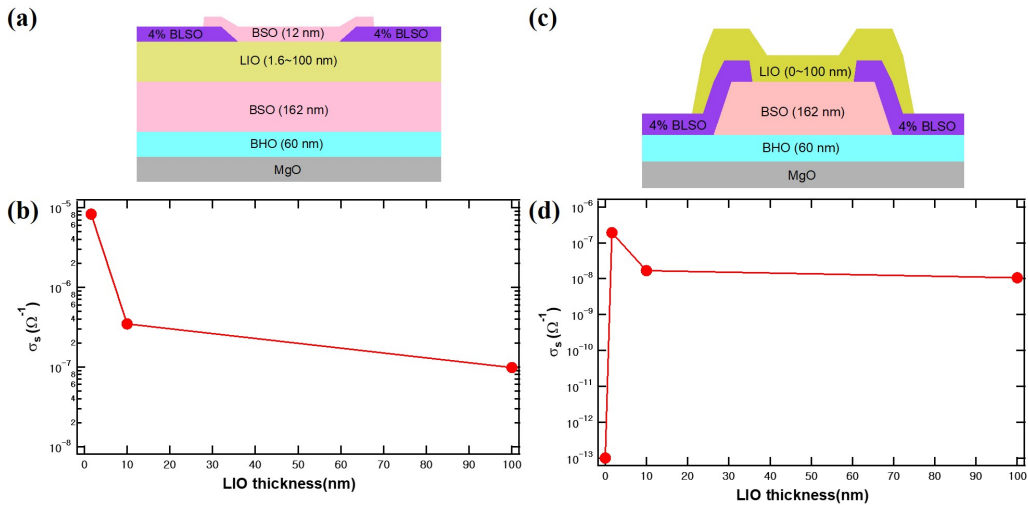


Figure 5.4 Different electrical characteristics depending on the deposition order of the interface between LIO and undoped BSO (a)(b) Structure and conductance results of the interface when the BSO layer was deposited on the LIO. (c)(d) Structure and conductance results of the interface when the LIO layer was deposited on the BSO.

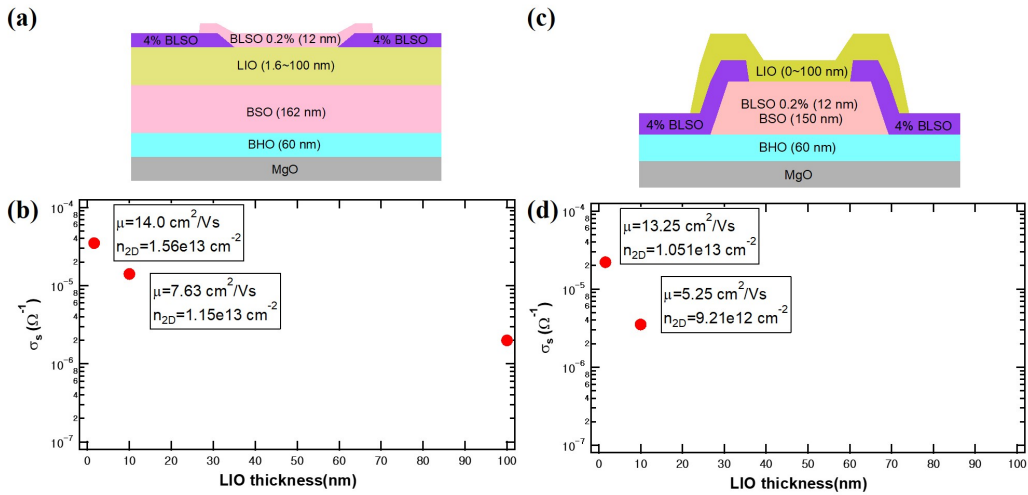


Figure 5.5 Different electrical characteristics depending on the deposition order of the interface between LIO and 0.2% La-doped BSO (a)(b) Structure and conductance results of the interface when the BLSO layer was deposited on the LIO. (c)(d) Structure and conductance results of the interface when the LIO layer was deposited on the BLSO.

5.4. Other two-dimensional electron gas based on BaSnO_3

From the analysis of the formation of LIO/BLSO 2DEG, we can expect another 2DEG formation based on BSO. First, other material instead of LIO that have similar material parameters with LIO can be used to make the quantum well with BSO while forming polarization like LIO. For example, $\text{LaScO}_3/\text{BLSO}$ [18] and $\text{LaLuO}_3/\text{BLSO}$ can have possibility to make similar 2DEGs. Second, instead of the combination of the polarization and conduction band offset to make electric field, only large conduction band offset can make 2DEG. GaN, ZnO and LIO/BLSO have polarization discontinuity that forms quantum well. And for the appropriate direction of polarization, they need deposition of a well terminated layer of a specific plane. Ga polar surface of GaN in GaN 2DEG [19] and Zn polar surface of ZnO in ZnO 2DEG [20] are known to be needed in the structure of Fig 4.1, 4.2, and 4.3, and LIO/BLSO may need SnO_2 terminated surface of BSO for 2DEG [21].

But if we only use conduction band offset increasing its value as a substitute for polarization discontinuity, 2DEG can be formed easily without termination control. This is similar with modulation doping of GaAs 2DEG and it will make uniform current without termination control.

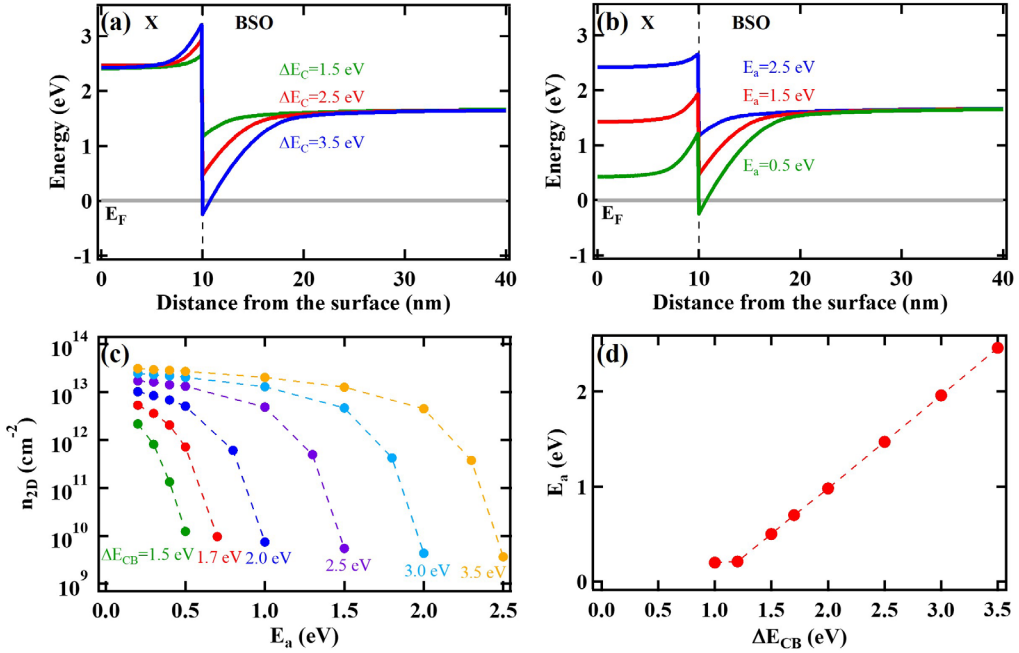


Fig 5.6 Quantum well formation without polarization based on BSO. (a) Minimum conduction band bending at unknown material X and BSO interface when the conduction band offset between X and BSO is 1.5, 2.5, and 3.5 eV with the deep donor activation energy of 2.5 eV of X. X does not have any polarization and has same material parameters with BSO, except the band gap of 5 eV. (b) Minimum conduction band bending at unknown material X and BSO interface when the deep donor activation energy of X is 0.5, 1.5, and 2.5 eV with the conduction band offset 1.5 eV. (c) Carrier densities of quantum well at each combination of the X deep donor activation energy and the conduction band offset between X and BSO. (d) The X deep donor activation energy and the conduction band offset between X and BSO that make the quantum well n_{2D} of about $1 \times 10^{10} \text{ cm}^{-2}$, which means minimum condition to form the quantum well.

In several simulations, I expected some materials that can form 2DEG with BSO without polarization like GaAs interface. Simulations of changing two material parameters of unknown material X were tried at the interface with an undoped BSO channel. Using all

other parameters identical to BSO without polarization, only conduction band offset between X and BSO and deep donor activation energy of X were adjusted to find the values that make quantum well because these two parameters of X can mainly change the quantum well although other material parameters also influence the formation of quantum well like presented previously. To apply various conduction band offset and activation energy, the band gap of X was set to 5 eV. For simplicity, the carriers were set as a deep donor of $1 \times 10^{20} \text{ cm}^{-3}$ in X and a deep acceptor of $4 \times 10^{19} \text{ cm}^{-3}$ in BSO without any shallow carriers.

In Fig 5.6(a) and (b), material X with parameters similar to LIO was studied. First, I adjusted the conduction band offset that act as a source of electric field at the interface, fixing the deep donor activation energy of X to 2.5 eV, same as that of LIO. This shows roughly how much conduction band offset is needed to form a quantum well for LIO without polarization. X is not completely identical to LIO because other parameters were entered the same as BSO. Fig 5.6(a) represents the results of band bending at the conduction band offset of 1.5, 2.5, and 3.5 eV. At the deep donor activation energy of X of 2.5 eV, conduction band offset of 1.5 and 2.5 eV cannot form a quantum well below the Fermi level showing the 0 cm^{-2} of n_{2D} at the interface. Conduction band offset of 3.5 eV barely start to produce $3.64 \times 10^9 \text{ cm}^{-2}$ of n_{2D} , which is much larger than that of LIO. Second, I adjusted deep donor activation energy of X at the conduction band offset of 1.5 eV, that is the similar value with the conduction band offset between LIO and BSO. The conduction band bending at deep donor activation energy of 0.5, 1.5, and 2.5 eV are shown in Fig 5.6(b). At least, deep donor activation energy of about 0.5 eV is needed to form quantum well at the interface without polarization. The n_{2D} was 0 cm^{-2} with deep donor activation energy of 1.5 and 2.5 eV and 2D electron carriers start to show at the interface with $1.21 \times 10^{10} \text{ cm}^{-2}$ of n_{2D} at 0.5 eV of activation energy. To make 2DEG using BSO and LIO without polarization, increasing the conduction band offset larger than about 3.5 eV is

needed, which is impossible thing, and adequate deep dopant is needed to lower the deep donor activation energy of LIO under about 0.5 eV.

I searched other combination of conduction band offset and deep donor activation energy to find other material that makes 2DEG interface without polarization instead of LIO. Fig 5.6(c) shows the change of n_{2D} according to the deep donor activation energy of X in each conduction band offset of 1.5, 1.7, 2.0, 2.5, 3.0, and 3.5 eV. I only presented the cases where the X itself does not have conduction to exclude carriers that are not 2DEG. With highest conduction band offset of 3.5 eV, forming a deep quantum well is possible to have large deep donor activation energies up to 2.0 eV. However, as the conduction band offset decreases lowering the electric field at the interface, it needs deep donors that can be activated more easily. In Fig 5.6(d), minimum combinations to form a quantum well that has about of $1 \times 10^{10} \text{ cm}^{-2}$ of n_{2D} are shown. We need to find materials that satisfies these conditions to find a new 2DEG based on BSO. I expect SrHfO₃ (SHO), SrZrO₃ (SZO) and (Ba,Sr)HfO₃ (BSHO) as a candidate of X that have conduction band offset with BSO larger than 2.5 eV and similar lattice constant with BSO [22]. Even if they do not have polarization, the interface can have 2DEG quantum well made by large conduction band offset and its n_{2D} will be much higher than GaAs 2DEG that has same 2DEG formation mechanism. Though we do not know about deep donor activation energy of candidate materials, a moderately small activation energy of deep donor will make 2DEG at the interface with BSO.

5.5. Conclusion

Through P-S simulations, it is realized that there is a speciality of LIO and BSO material parameters for forming quantum well with high n_{2D} . And it was possible to confirm the future direction of the LIO/BLSO interface by reducing deep acceptor density of BSO. Depositing other materials on the LIO layer and changing the deposition order of LIO and BSO also raised n_{2D} . Another candidate material for the formation of 2DEG based on BSO was predicted as SHO, SZO, and BSHO. The attempt to analyze the influence of the material parameters on oxide heterostructure and research to improve the LIO/BLSO interface will help to study the physical properties of 2D quantum wells and their applications.

References

- [1] Y. Kim, Y. M. Kim, J. Shin, and K. Char, *APL Mater.* **6**, 096104 (2018).
- [2] C. Guguschev, D. Klimm, M. Brützam, T.M. Gesing, M. Gogolin, H. Paik, A. Dittmar, V.J. Fratello, D.G. Schlom, *J. Cryst. Growth* **528**, 125263 (2019).
- [3] W.-J. Lee, H. J. Kim, E. Sohn, T. H. Kim, J.-Y. Park, W. Park, H. Jeong, T. Lee, J. H. Kim, K.-Y. Choi, and K. H. Kim, *Appl. Phys. Lett.* **108**, 082105 (2016).
- [4] Z. Galazka, K. Irmscher, S. Ganschow, M. Zupancic, W. Aggoune, C. Draxl, M. Albrecht, D. Klimm, A. Kwasniewski, T. Schulz, M. Pietsch, A. Dittmar, R. Grueneberg, U. Juda, R. Schewski, S. Bergmann, H. Cho, K. Char, T. Schroeder, and M. Bickermann, *Phys. Status Solidi A*, 2100016 (2021).
- [5] Y. M. Kim, T. Markurt, Y. Kim, M. Zupancic, J. Shin, M. Albrecht, and K. Char, *Sci. Rep.* **9**, 16202 (2019).
- [6] A. Giampietri, Ph. D. thesis, Cattolica del Sacro Cuore University (2017).
- [7] U. Kim, C. Park, T. Ha, Y. M. Kim, N. Kim, C. Ju, J. Park, J. Yu, J. H. Kim, and K. Char, *APL Materials* **3**, 036101 (2015).
- [8] Y. M. Kim, C. Park, T. Ha, U. Kim, N. Kim, J. Shin, Y. Kim, J. Yu, J. H. Kim, and K. Char, *APL Mater.* **5**, 016104 (2017).
- [9] U. Treske, N. Heming, M. Knupfer, B. Büchner, E. D. Gennaro, A. Khare, U. S. D. Uccio, F. M. Granozio, S. Krause, and A. Koitzsch, *Sci. Rep.* **5**, 14506 (2015).
- [10] A. Vegas, M. Vallet-Regi, J. M. Gonzalez-Calbet, and M. A. Alario-Franco, *Acta Cryst.* **B 42**, 167 (1986).
- [11] S. Piskunov, E. Heifets, R. I. Eglitis, and G. Borstel, *Comput. Mater. Sci.* **29**, 165 (2004).
- [12] Nurazila Mat Zali, Che Seman Mahmood, Siti Mariam Mohamad, Choo Thye Foo, and Julie Adrianny Murshidi, *AIP Conf. Proc.* **1584**, 160 (2014).
- [13] L. Vasylechko, A. Matkovski, A. Suchocki, D. Savytskii, I. Syvorotka, *J. of Alloys Compd.* **286**, 213 (1999).
- [14] H. M. Park, H. J. Lee, S. H. Park, and H. I. Yoo, *Acta Crystallogr., Sect. C: Cryst. Struct. Commun.* **C59**, i131–i132 (2003).
- [15] H. J. Kim, U. Kim, H. M. Kim, T. H. Kim, H. S. Mun, B.-G. Jeon, K. T. Hong, W.-J. Lee, C. Ju, K. H. Kim, and K. Char, *Appl. Phys. Express* **5**, 061102 (2012).

- [16] G. Lupina, O. Seifarth, P. Dudek, G. Kozłowski, J. Dabrowski, H.-J. Thieme, G. Lippert, T. Schroeder, and H.-J. Müssig, *Phys. Status Solidi B* **248**, 323 (2011).
- [17] C. Park, U. Kim, C. J. Ju, J. S. Park, Y. M. Kim, and K. Char, *Appl. Phys. Lett.* **105**, 203503 (2014).
- [18] H. Cho, D. Song, Y. Kim, and K. Char, “Two-dimensional electron gas at the $\text{LaScO}_3/\text{BaSnO}_3$ interface” (unpublished).
- [19] O. Ambacher, J. Smart, J. R. Shealy, N. G. Weimann, K. Chu, M. Murphy, W. J. Schaff, L. F. Eastman, R. Dimitrov, L. Wittmer, M. Stutzmann, W. Rieger, and J. Hilsenbeck, *J. Appl. Phys.* **85**, 3222 (1999).
- [20] H. Tampo, H. Shibata, K. Matsubara, A. Yamada, P. Fons, S. Niki, M. Yamagata, and H. Kanie, *Appl. Phys. Lett.* **89**, 132113 (2006).
- [21] S. Kim, J. Lee, B. Kim, M. Lippmaa, and K. Char, “Role of termination layer in formation of 2DEG state at the $\text{LaInO}_3/\text{BaSnO}_3$ interface” (unpublished)
- [22] L. Bjaalie, B. Himmetoglu, L. Weston, A. Janotti, and C. G. Van de Walle, *New J. Phys.* **16**, 025005 (2014).

Chapter 6. Summary

BSO is a perovskite oxide that exhibits high mobility, oxygen stability, and transparency with a wide band gap of 3.1 eV. The wide range of resistivity of n-type doped BSO and the possibility of p-n junction also broaden the scope of application. This Ph.D. dissertation was dedicated to BSO-based 2D systems. I focused on δ -doped BSO and LIO/BLSO 2DEG to investigate 2D systems with quantum wells.

δ -doped BSO is a simple structure that can form 2D quantum well. The BSO/BLSO/BSO structure showed a quantum well at its center, and the electrical characteristics of the δ -doped BSO were physically described by band bending at the BLSO/BSO interface and Fermi level pinning of the BLSO surface using P-S simulation. However, at the temperature dependent electrical properties results, the mobility value at low temperature is not sufficient to directly see the 2D quantum phenomena, and a reduction of dislocation density of BSO is required.

LIO/BLSO system is a more complex 2D system. As a basic step in this study, XRD and STEM measurement were first used to confirm the structural characterization of the LIO/BLSO interface. LIO/BLSO on MgO substrate showed conducting properties and was thought to be 2DEG. And I found the difference in the electrical properties between the LIO/BLSO interfaces grown on STO and MgO substrates, which was well explained by the calculations changing deep acceptor density of BSO, but the tendency of the LIO thickness dependence was the same. The FET was also fabricated using the 2DEG interface as a channel layer and the LIO as a dielectric layer. It showed great properties compared to oxide-based devices with the highest mobility of $61.3 \text{ cm}^2/\text{Vs}$ and the on/off ratio of 10^9 . Mobility at the LIO/BLSO interface showed lower value than needed to see quantum phenomena at low temperature and lattice matched substrate with BSO is required.

The Formation of 2DEG at LIO/BLSO interface was understood by physically analyzing the roles of material parameters using P-S simulation. Including deep acceptor density of BSO that explained the difference of the interfaces on STO and MgO, 13 kinds of material parameters of LIO and BSO (polarization, concentration and activation energy of donor, deep donor, acceptor, and deep acceptor, effective mass, dielectric constant, band gap, and conduction band offset between two materials) were analyzed to show how quantum well is formed with high 2D carrier density, and how the LIO/BLSO interface has their experimental electrical properties. In addition, I summarized the possibilities of the LIO/BLSO 2DEG system and showed the future direction suggesting another BSO based 2D system.

국문초록

BaSnO₃ 기반의 2차원 시스템에 관한 연구

김유정

서울대학교 물리천문학부

산화물 반도체는 투명하면서 높은 전기 전도도를 보임으로 인해 많이 연구되어왔다. 특히 페로브스카이트 구조의 산화물은 강자성, 강유전성, 다강성, 초전도성 같은 추가적인 특이한 성질을 보여주었다. 그러나 산화물은 높은 온도에서 산소가 불안정하고, 상온에서는 낮은 전자 이동도를 가지고 있어 디바이스 응용에 있어서 문제가 되어왔다. BaSnO₃는 페로브스카이트 구조의 산화물로 10^{20} cm^{-3} 정도의 전하 밀도에서 산화물 중 가장 높은 전자 이동도인 $320 \text{ cm}^2/\text{Vs}$ 를 보여주고, 높은 산소안정성을 가지고 있어 p-n 접합도 가능하게 하는 물질이다. 이러한 특성으로 인해 BaSnO₃는 고속으로 동작하는 전자 분야, 높은 전력을 이용하는 전자 분야, 태양전지 등에 응용되어왔고 응용이 가능하다.

이 논문은 BaSnO₃를 기반으로 하는 이차원 시스템에 대한 연구에 초점을 두어, BaSnO₃/(Ba,La)SnO₃/BaSnO₃의 구조를 가지는 BaSnO₃ 델타 도핑 시스템과 LaInO₃/BaSnO₃ 구조에서 만들어지는 양자우물의 전기적 특성을 보여준다. 델타 도핑된 BaSnO₃ 시스템에서는 La이 도핑된 BaSnO₃ 층에 양자우물을 갖고 있고, 이 양자우물은 BaSnO₃/(Ba,La)SnO₃ 계면에서의 전도 밴드의 휘어짐에 의해 만들어진다. LaInO₃/BaSnO₃ 시스템에서는 BaSnO₃ 쪽에 양자우물을 가지고 있고, 이는 LaInO₃와 BaSnO₃ 두 물질 사이의 전도 밴드의 차이와 LaInO₃의 극성에 의해 만들어진다.

델타 도핑된 BaSnO₃ 시스템에서는, 다양한 두께와 도핑 레벨에서 이차원 전하 밀도를 측정해 두가지의 예측하지 못한 전기적 특성을 얻었는데, 얇은

(Ba,La)SnO₃ 샘플의 예상보다 너무 낮은 전도도와 도핑하지 않은 BaSnO₃ 캐핑 층의 두께를 두껍게 함에 따라 증가하는 전도도가 그것이다. 푸아송-슈뢰딩거 시뮬레이션을 이용한 분석으로 이러한 거시적인 두가지의 특성이 BaSnO₃와 (Ba,La)SnO₃ 사이의 연속적인 밴드 휘어짐과 BaSnO₃ 캐핑 층의 두께에 따라 변화하는 표면 경계조건을 통해 물리적으로 잘 설명되는 것을 확인하였다. 또한, 델타 도핑된 BaSnO₃에서 온도에 따라 변화하는 저항을 측정하였고, 이는 양자현상 측정의 기반이 될 것이다.

LaInO₃/BaSnO₃ 시스템에서는 LaInO₃와 BaSnO₃ 둘 다 절연체임에도 불구하고 계면에서 전도도의 증가를 보여준다. 이 계면은 이차원 전자 가스로 여겨지고, 여기서 BaSnO₃의 도핑 레벨과 LaInO₃의 두께를 바꿔가며 계면의 전기적 특성을 측정하였다. 또한 이차원 전자가스를 채널층으로, LaInO₃를 높은 유전상수를 가지는 산화물로 사용하여 장 효과 트랜지스터를 만들었고, 그것은 잘 작동하였다. LaInO₃/BaSnO₃ 계면에서 또한 온도에 따라 변하는 저항을 측정하였고, 양자현상을 보기 위해서는 현재보다 더 낮은 dislocation 밀도가 필요하다.

LaInO₃/BaSnO₃ 계면의 실험결과를 푸아송-슈뢰딩거 시뮬레이션을 통해 분석하여 양자우물에서 높은 이차원 전하밀도가 형성되는 방법에 대해 이해하였다. LaInO₃와 BaSnO₃의 13가지의 물질 파라미터 (극성, 도너, 억셉터, 딥 도너, 딥 억셉터의 전하밀도와 활성화 에너지, 유효질량, 유전상수, 밴드갭, 두 물질 사이의 전도 밴드의 차이)를 분석하여 물질 파라미터들이 양자우물에 어떠한 영향을 미치는지에 대해 이해하였다. LaInO₃의 높은 극성, 적당한 전하량과 전하의 활성화 에너지, 너무 작지 않은 유효질량, 너무 크지 않은 유전상수, 큰 전도 밴드 차이가 기존의 이차원 전자가스에 비해 LaInO₃/BaSnO₃ 계면에서 높은 전하 밀도를 가지는 양자우물을 만들었다. 이러한 계산 분석을 기반으로 기존에 알려진 다섯가지의 전자가스들을 비교하고, LaInO₃/BaSnO₃ 이차원 전자가스를 현재보다 개선시킬 방법을 제시하였고, BaSnO₃를 기반으로 하는 다른 이차원 전자가스 계면을 예측하였다.

델타 도핑된 BaSnO₃와 LaInO₃/BaSnO₃에서의 이차원 전자가스에 대한 연

구는 BaSnO₃를 기반으로 하는 이차원 시스템에서의 거시적인 전기적 특성을 물리적으로 이해할 수 있게 했고, 그에 대한 분석결과를 통해 또 다른 BaSnO₃ 기반의 이차원 전자 가스를 예측하였다. 그리고 이러한 연구는 추후에 BaSnO₃의 dislocation 밀도 문제를 해결해 양자 현상을 보는데 도움이 될 것이다.

Keywords: BaSnO₃, LaInO₃, 페로브스카이트 산화물, 델타 도핑, 이차원 전자 가스, 푸아송-슈뢰딩거 시뮬레이션.

Student Number: 2015-20321